博士学位論文

高調波磁束を利用した可変速ギアの研究

アリフ　ザイニ

２０１５年１月

大阪大学大学院工学研究科

知能・機能創成工学専攻

Abstract

Rising costs in fossil fuels and commitments to reduce the production of carbon dioxide have spurred interest in renewable energy, especially in wind energy, and due to this, many new wind turbines are being constructed around the world. However, large wind power turbines have to be installed in places that are difficult for human access such as on top of hills, making the mechanical gears that are utilized difficult to maintain. To achieve maintenance free operation of the wind turbine system, the usage of magnetic gears have been suggested and thus magnetic gears are becoming a burgeoning area of study. However the gear ratios of these magnetic gears are fixed, and thus the generator will not always be operating at its most efficient speed. To achieve maintenance free operation of wind turbines that always operate at their most efficient operating speed, this thesis proposes the utilization of magnetic gears that have continuously variable gear ratios.

In Chapter 1, the history of magnetic gears is discussed, the operating principle of magnetic gears that utilize flux harmonics are explained, and the aim of this research is presented. In Chapter 2, finite element analysis method (FEM), which was used in this research to determine the characteristics of the proposed magnetic gears are explained.

In Chapter 3, two magnetic gears that can achieve a continuously variable gear ratio are presented, their respective characteristics are investigated and they are compared with each other. It was found that the Vernier version has better torque characteristics although steps will have to be taken to decrease its torque ripples.

In Chapter 4, the power equations of the magnetic gears are derived and their efficiency is evaluated. It was found that the proposed magnetic gears would be most suitable in the high speed rotation range.

Finally, two topics that are connected to this research: the Vernier motor and the induction magnetic gear, are also extensively investigated and are inserted in the appendix.

Contents

Chapter 1 Introduction

1.1 History of Magnetic Gears

Magnetic gears have been around for over 100 years. They transmit torque without contact and so there is no energy loss from friction. Also, they are not subject to wear and tear, meaning that they can operate with little or no maintenance required. Furthermore, magnetic gears possess inherent overload protection characteristics: during overload, the rotors just slip – preventing breakage of the magnetic gear itself and protecting the surrounding equipment.

The earliest model was by Armstrong in 1901. Armstrong's model (Fig. 1.1) was very simple: it utilizes magnetic attraction by replacing the teeth of conventional mechanical gears with magnetic steel segments and electromagnets.

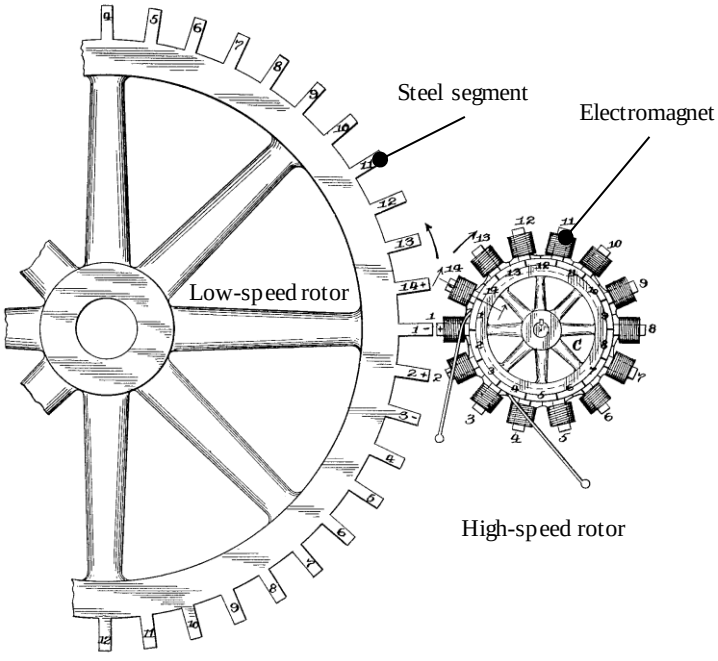

Fig. 1.1 Magnetic gear proposed by Armstrong[1].

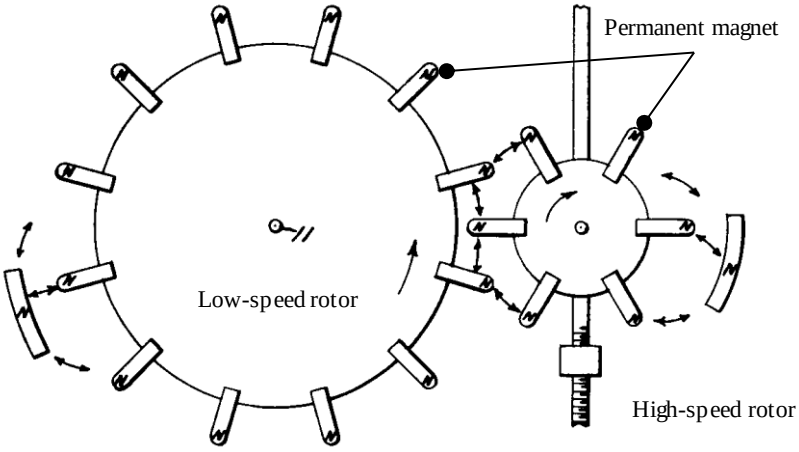

Fig. 1.2 Magnetic gear proposed by Faus[2].

Another similar model was by Faus in 1941 (Fig. 1.2). However, Faus's model is different from Armstrong's in that permanent magnets were used instead of steel segments and electromagnets. Also, whereas Armstrong utilized magnetic attraction, Faus utilized magnetic repulsion. The permanent magnets were configured such that the N poles of both rotors were always pointing outwards.

The first two examples were just conventional mechanical gears whose teeth were replaced with magnetic material. The big drawback of these models was that only one or two teeth from each rotor could interact with each other at any one time. For conventional mechanical gears, this did not pose any problems, but for magnetic gears it meant that the maximum transmission torque was very small. Due to this, these two models were never commercialized.

The next two magnetic gears proposed by Reese[3] (1967) and Martin[4] (1968), shown in Figs. 1.3 and 1.4 respectively, are structurally and conceptually different. Structurally, instead of just two rotors, the respective inventors introduced a stationary part in between the rotors. The function of this stationary part is to generate flux harmonics, which will be detailed in the next chapter. These magnetic gears do not operate by simply using magentic attraction or repulsion, but use these flux harmonics to transmit torque, which is what make these magnetic gears also conceptually different. Furthermore the stationary part and the two rotors are concentric. This means that all the teeth of the magnetic gear can simultaneously interact with each other, largely

increasing the maximimum transmission torque. However, at that time, powerful rare-earth magnets widely available today had not yet been developed, and the maximum transmission torque was still very low and thus these magnetic gears did not gain much attention.

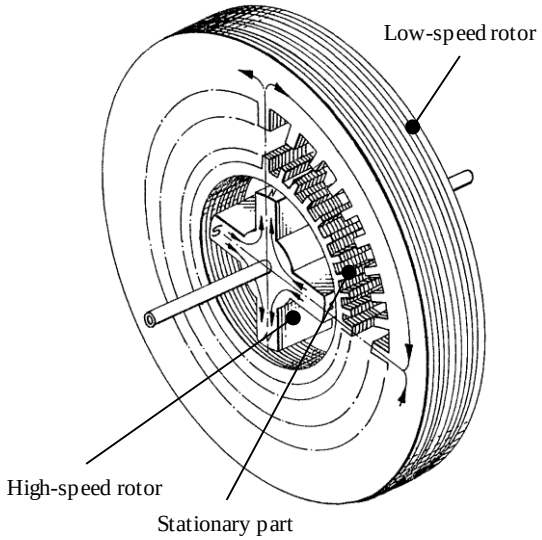

Fig. 1.3 Magnetic gear proposed by Reese[3].

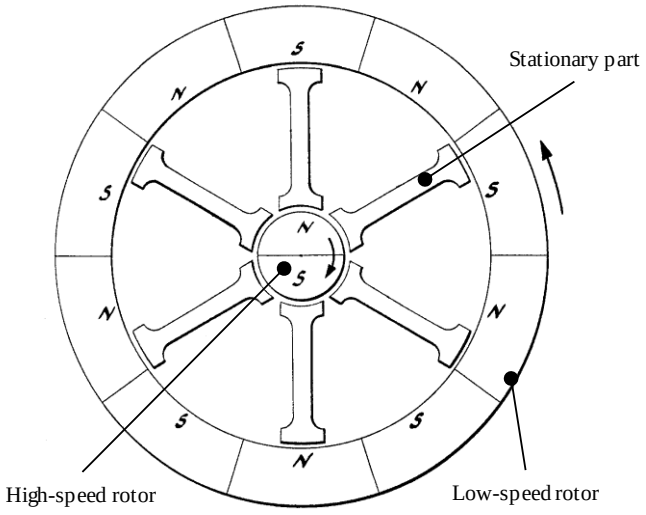

Fig. 1.4 Magnetic gear proposed by Martin[4].

It was only until in 2001 when Atallah combined high-performance rare earth magnets with the concept of magnetic gears utilizing flux harmonics (Fig. 1.5) did magnetic gears really gain any attention. Atallah's paper reported the ability of his model to transmit a torque density of over 100kNm/m^3. Two years later, Rasmussen was the first to successfully create a working prototype, shown in Fig. 1.6.

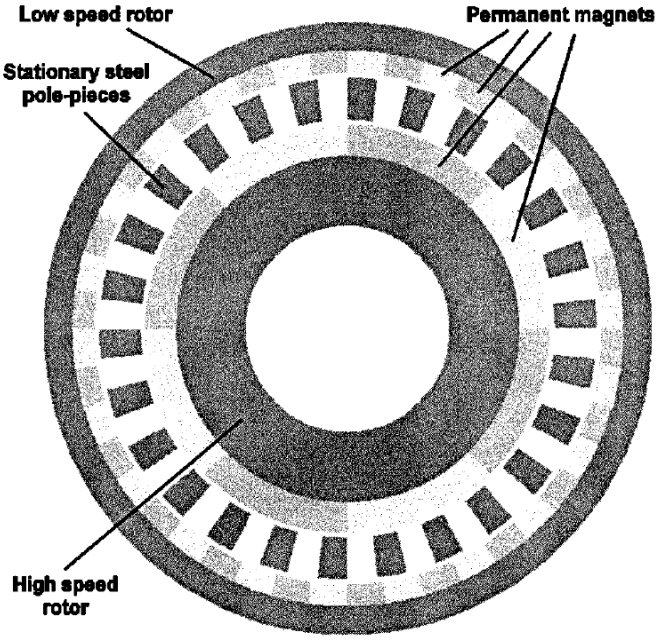

Fig. 1.5 Magnetic gear proposed by Atallah[5].

Fig. 1.6 First prototype developed by Rasmussen[6].

In the next section, the fundamentals to the operating principle of magnetic gears utilizing flux harmonics will be detailed.

1.2 Fundamentals of Flux Space Harmonics

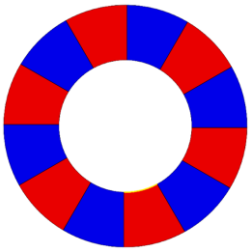

(a) Array of arc-shaped permanent magnets.

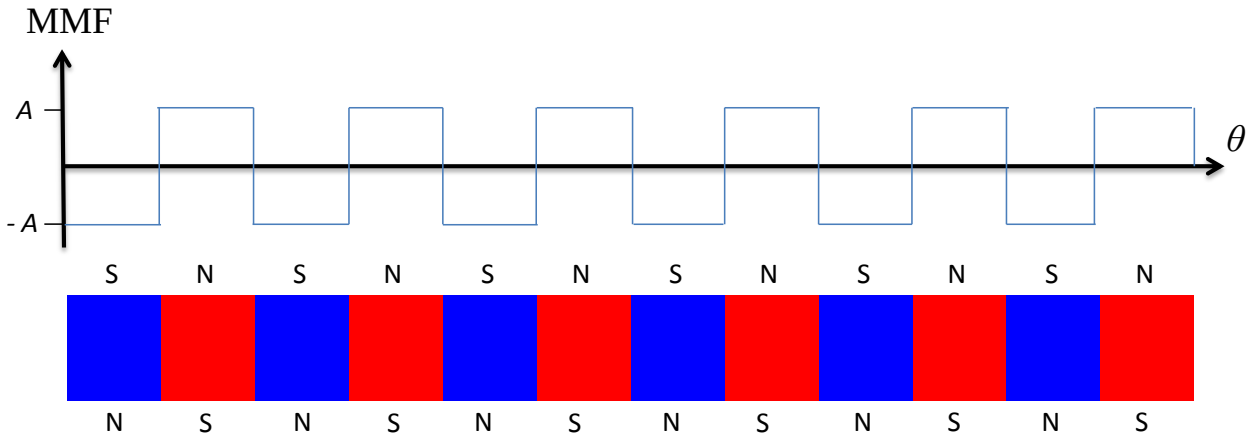

(b) Magnetomotive force distribution of array of magnets.

Fig. 1.7 Array of PMs and resulting MMF distribution.

Consider an array of arc-shaped permanent magnets arranged together such that the N and S poles alternate, as shown in Fig. 1.7(a). If the magnets are flattened out on a plane, as shown in Fig. 1.7(b), the magnetomotive force (MMF) of the magnet array would look like a square wave and can be mathematically expressed by equation (1.1)

$$F(\theta) = \sum_{h=1}^{\infty} \frac{A}{(2h-1)} \sin\{(2h-1)N_h\theta\} \tag{1.1}$$

where A is the amplitude coefficient of the magnetomotive force and N_h is the number of permanent magnet pole pairs.

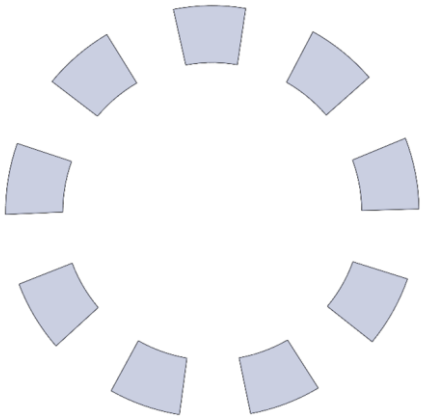

(a) Array of arc-shaped magnetic steel pieces.

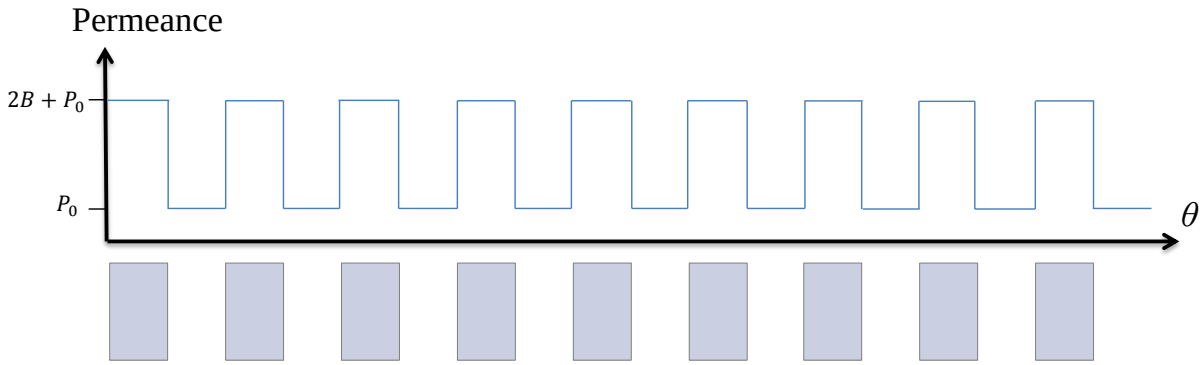

(b) Permeance distribution of an array of magnetic steel pieces.

Fig. 1.8 Array of magnetic steel pieces and resulting permeance distribution.

Next, consider an array of arc-shaped magnetic steel pieces placed at equally spaced intervals, such as in Fig. 1.8(a). Again, if the steel pieces are flattened out on a plane, as shown in Fig. 1.8(b), the permeance of the steel pieces would also look like a square wave, and can be mathematically expressed in equation (1.2)

$$P(\theta) = P_0 + \sum_{s=1}^{\infty} \frac{B}{(2s-1)} \sin\{(2s-1)N_s\theta\} \tag{1.2}$$

where P_0 is the permeance of vacuum, B is the amplitude coefficient of the permeance, and N_s is the number of steel pieces.

The magnetic flux distribution in any space can be obtained by multiplying the magnetomotive force in that area with the permeance, as shown in equation (1.3).

$$\varphi = F \times P \tag{1.3}$$

Therefore, in the case when only the magnets exist, the magnetic flux distribution in the space above the magnets would be

$$F(\theta) = \sum_{h=1}^{\infty} \frac{AP_0}{(2h-1)} \sin\{(2h-1)N_h\theta\}. \tag{1.4}$$

It is almost the same as the magnetomotive force equation in (1.1) except the permeance of vacuum P_0 has been added.

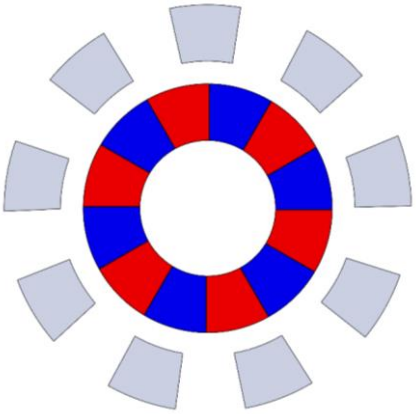

(a) Steel pieces surround permanent magnets.

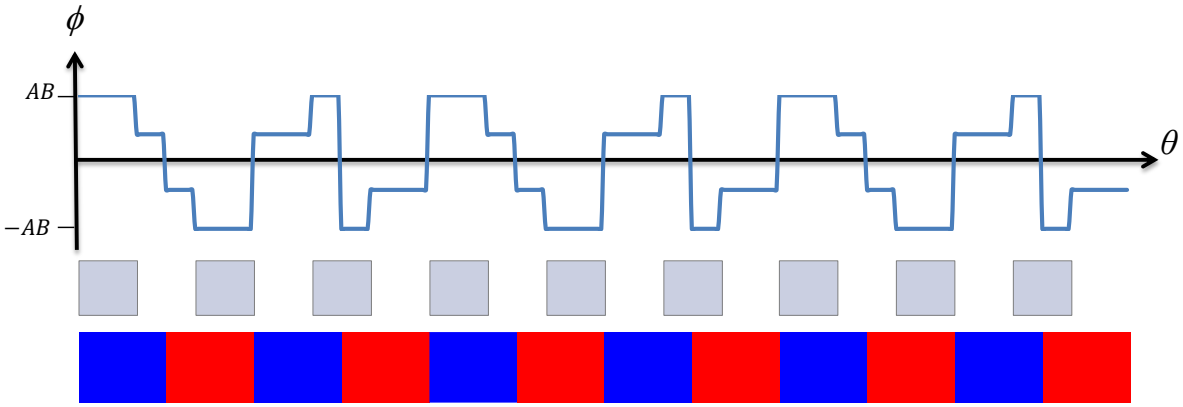

(b) Distorted flux distribution when steel pieces are added

Fig. 1.9 Flux distribution of area above magnet and steel pieces.

Next, when the steel pieces are placed around the magnets as in Fig. 1.9(a), the magnetic flux distribution around the steel pieces, which is illustrated in Fig. 1.9(b) and is obtained by multiplying equations (1.1) and (1.2), becomes equation (1.5).

$$\phi(\theta) = \sum_{h=1}^{\infty} \frac{AP_0}{(2h-1)} \sin(C_1\theta) + \sum_{h=1}^{\infty}\sum_{s=1}^{\infty} C_0 \left[\cos(C_2 - C_1)\,\theta - \cos(C_2 + C_1)\,\theta\right] \tag{1.5}$$

Equation (1.5) contains the variables C_0, C_1, and C_2, which are used to simplify calculations. Their definitions are shown in equations (1.6), (1.7), and (1.8).

$$C_0 = \frac{AB}{2(2h-1)(2s-1)} \tag{1.6}$$

$$C_1 = (2h-1)N_h \tag{1.7}$$

$$C_2 = (2s-1)N_s \tag{1.8}$$

Fig. 1.9 shows that the flux distribution has now become distorted, indicating the existence of harmonics in the flux distribution waveform. Indeed, we can confirm this in equation (1.5), where we can see that along with the original component of equation (1.4) when only the magnets existed, which will be called the Fundamental Component, now two new components can be seen. These two components are the flux harmonics. In this section, they will be called Harmonic 1 and Harmonic 2. They exist due to the steel pieces modulating the magnetic flux. What is most interesting and also crucial about these harmonics to the principle of magnetic gears is explained next.

Assume that the array of magnets has rotated $\omega_h t$ radians, where ω_h is the angular velocity of the magnets, and t is time. The new MMF distribution is:

$$F(\theta) = \sum_{h=1}^{\infty} \frac{A}{(2h-1)} \sin\{(2h-1)N_h(\theta - \omega_h t)\}. \tag{1.9}$$

Thus the new flux distribution is:

$$\begin{aligned} \phi(\theta) = &\sum_{h=1}^{\infty} \frac{AP_0}{(2h-1)} \sin C_1(\theta - \omega_h t) \\ &+ \sum_{h=1}^{\infty}\sum_{s=1}^{\infty} C_0 \left[\cos(C_2 - C_1)\left(\theta + \frac{C_1}{C_2 - C_1}\omega_h t\right) - \cos(C_2 + C_1)\left(\theta - \frac{C_1}{C_2 + C_1}\omega_h t\right)\right]. \end{aligned} \tag{1.10}$$

From (1.10), we can see that rotation angle of the Fundamental Component is the same as the magnets, which is $\omega_h t$. However the rotation angles of the harmonics are different. This is all summarized in Table 1.1.

Table 1.1 Summary of the rotation angles of the flux components

Component Name	Harmonic Order	Rotation Angle
Fundamental Component	$C_1\theta$	$\omega_h t$
Harmonic 1	$C_2 - C_1$	$-\frac{C_1}{C_2 - C_1}\omega_h t$
Harmonic 2	$C_2 + C_1$	$\frac{C_1}{C_2 + C_1}\omega_h t$

It is this characteristic of the harmonics whereby it rotates at different angular velocities from the magnets that can be utilized to create a magnetic gear.

1.3 Operating Principle of Magnetic Gears

Continuing from the previous section, to create a magnetic gear, the flux harmonics have to be utilized. This is done by introducing another set of magnets that have the same number of magnetic pole pairs as the harmonic order of either harmonic component outside of the steel pieces. In other words, the following equation must hold true

$$C_2 \mp C_1 = (2l - 1)N_l \tag{1.11}$$

where N_l is the number of permanent magnet pole pairs outside the steel pieces and l is a positive integer. When this is done, the new set of magnets will couple with the harmonic component and rotate with it.

Fig. 1.9(a) shows 6 magnet pole pairs and 9 steel pieces. From Table 1.1, if we input $N_h = 6,\ N_s = 9$ into Harmonic 1, possible harmonic orders become 3, 15, 21, 39, … . If we input the same variables into Harmonic 2, possible harmonic orders become 15, 27, 33, … . If the harmonic order of 3 $(h = 1, s = 1)$ from Harmonic 1 is chosen to be used for our magnetic gear, then 3 magnet pairs must be introduced to the space outside of the steel pole pieces (see Fig. 1.10). Since the number of magnet pairs outside of the steel pieces are the same as the order of a harmonic component (3 in this case), the outside

magnets will couple with the harmonic and rotate together with it.

The gear ratio for this particular magnetic gear is

$$G_r = \frac{Output\ rotor\ speed}{Input\ rotor\ speed} = \frac{-\frac{C_1}{C_2 - C_1}\omega_h t}{\omega_h t} = -\frac{C_1}{C_2 - C_1} = -\frac{6}{9-6} = -2{:}1 \tag{1.12}$$

with the magnets outside rotating twice as fast as the magnets inside. It should be pointed out that the rotor with fewer magnets will rotate faster than the rotor with a larger number of magnets. Due to this reason, for this particular magnetic gear, the magnets outside becomes the High Speed Rotor (HSR) and the magnets on the inside become the Low Speed Rotor (LSR), as shown in Fig. 1.11(a).

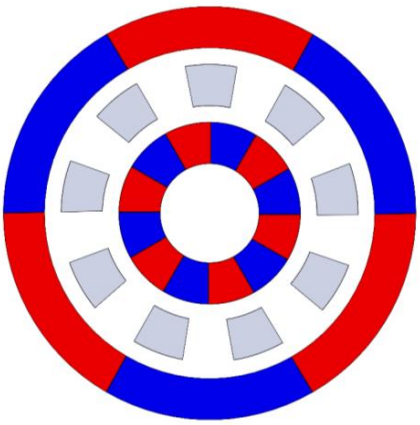

Fig. 1.10 Example of a magnetic gear.

However it is actually not necessary for the steel pieces to be stationary. Another popular configuration for the magnetic gear is to fix the rotor with the more magnets and leave the steel pieces and rotor with the fewer magnets to rotate. In this configuration, the steel pieces will become the Low Speed Rotor and the rotor with the fewer magnets will become the High Speed Rotor (see Fig. 1.11(b)). Another configuration is to fix the rotor with the fewer magnets, and leave the steel pieces and rotor with the more magnets to rotate. The steel pieces become the Low Speed Rotor and the rotor with the more magnets become the High Speed Rotor (see Fig. 1.11(c)).

Of course, different rotating parts will mean different gear ratios. How the gear ratios change with which part is being fixed is summarized in Table 1.2.

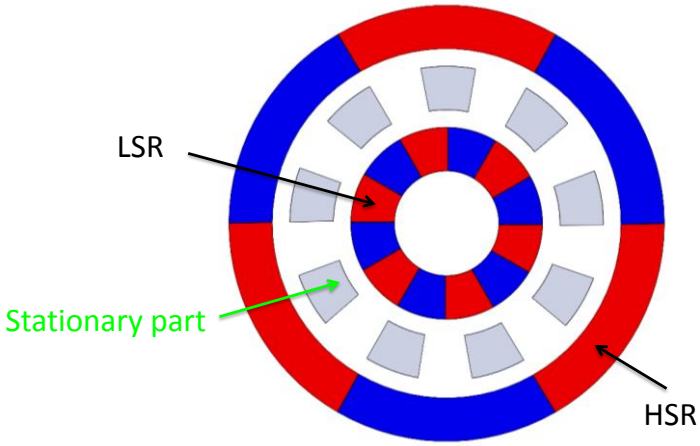

(a) Steel pieces stationary configuration

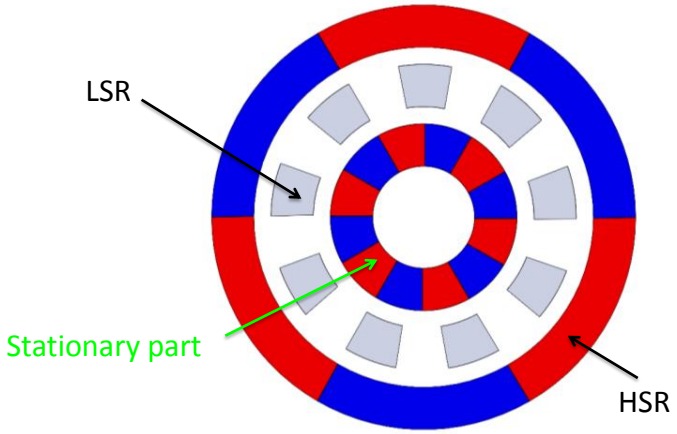

(b) More magnets stationary configuration

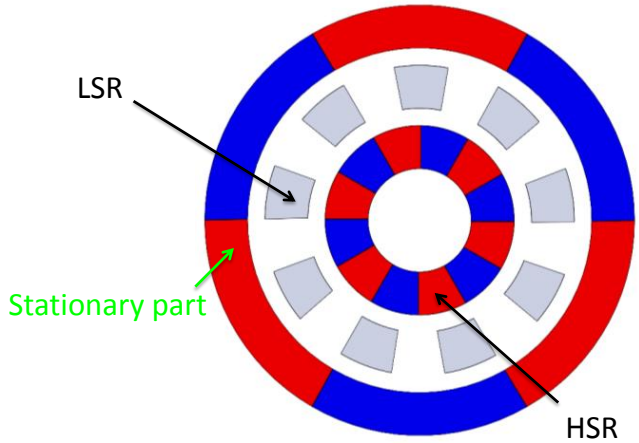

(c) Fewer magnets stationary configuration

Fig. 1.11 Possible configurations of the magnetic gear.

Table 1.2 Gear ratio according to different gear configurations.

	Stationary Part	HSR	LSR	Gear Ratio
(a)	Steel Pieces	Fewer magnets	More Magnets	－2：1
(b)	More Magnets	Fewer Magnets	Steel Pieces	3：1
(c)	Fewer Magnets	More Magnets	Steel Pieces	1.5：1

One would probably notice by now that this magnetic gear is quite similar to the planetary gear train (see Fig. 1.12) in terms of having three main parts and also three possible operating configurations. Due to this, this magnetic gear that utilizes flux harmonics is also sometimes called a magnetic planetary gear train in some literature[7-9].

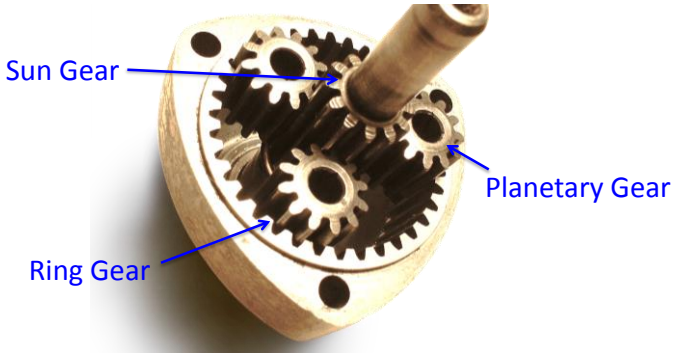

Fig. 1.12 Mechanical planetary gear train.

1.4 Magnetic Gears with Variable Gear Ratios

All the magnetic gears that have been introduced thus far have a fixed gear ratio. In this section, magnetic gears with variable gear ratios are introduced.

Fig. 1.13 shows a model proposed by Daif[10]. Instead of permanent magnets, electromagnets powered by DC currents are used instead. The outer most part is fixed, much like the configuration of the permanent magnet version shown in Fig. 1.11(c). A variable gear ratio is achieved by changing the polarity of the electromagnets and also the number of electromagnets being used. In his paper, Daif analyzed two gear ratios: $G_r = -3{:}1$ shown in Fig. 1.14(a) and $G_r = -1{:}3$ shown in Fig. 1.14(b).

Daif's proposal at first glance seems like an excellent idea to obtain various gear

ratios. However the number of gear ratios that can be achieved practically is actually very limited. This is due to the fact that for the gear to function properly, equation (1.11) must always be satisfied, and this severely limits the gear ratios possible.

Daif's prototype in Fig. 1.13 uses 30 coils each on the stator and inner rotor, and 20 steel pieces. With 30 coils in the stator and inner rotor, by changing the polarity of the coils, 15, 10, 6, 5, 3 or 1 magnetic pole-pairs can be obtained. However this flexibility in the number of poles is severely limited by the 20 steel pole piece because when the possible number of magnetic pole-pairs and the 20 steel pieces are substituted into equation (1.11), one quickly realizes that only the two gear ratios shown in Fig. 1.14 can be obtained.

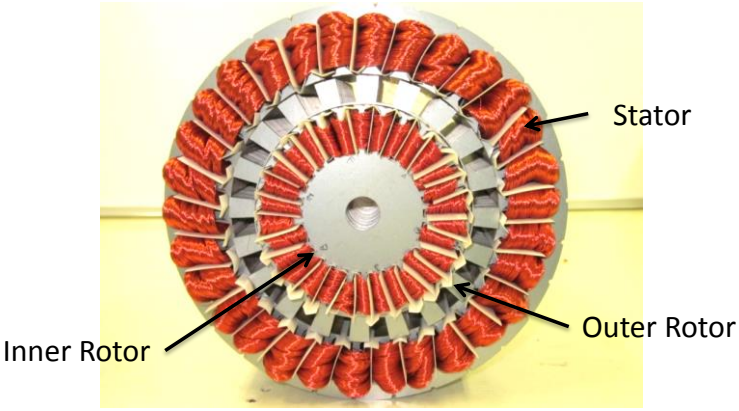

Fig. 1.13 Variable gear ratio magnetic gear by Daif[10].

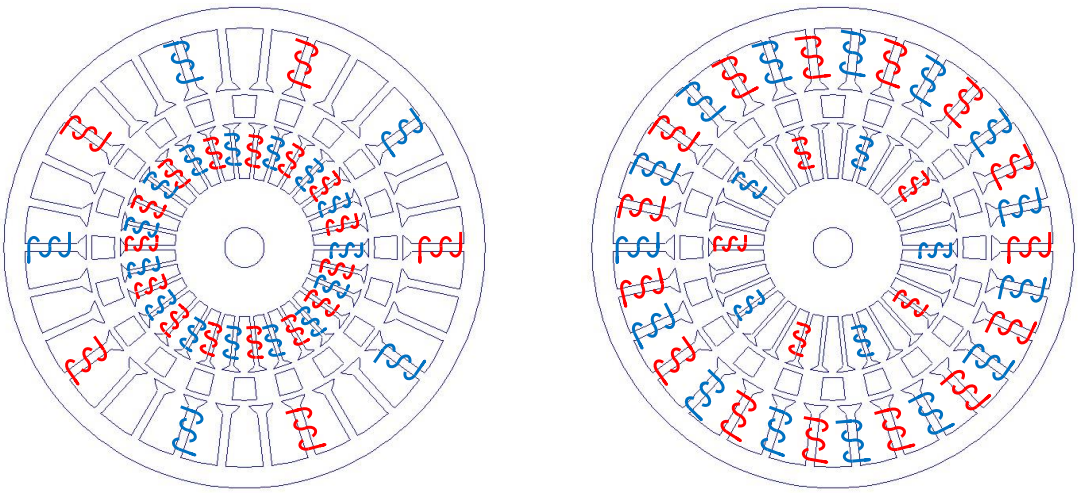

(a) $G_r = -3:1$ (b) $G_r = -1:3$

Fig. 1.14 Different gear configurations by Daif.

Shah[11] proposed a model illustrated in Fig. 1.15(a) whereby the steel pieces of Atallah's model shown in Fig. 1.5 are connected to a motor. By controlling the rotation of these steel pieces, which he calls the Control Rotor, a continuously variable gear ratio can be achieved. The operating principle for this is explained next.

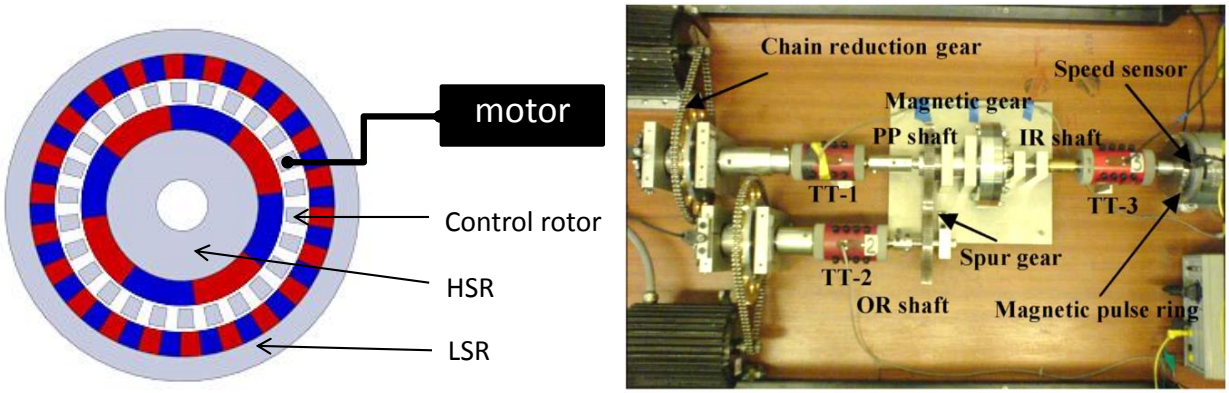

(a) Illustration of concept (b) Experimental setup of prototype

Fig. 1.15 Magnetic gear with control rotor proposed by Shah[11].

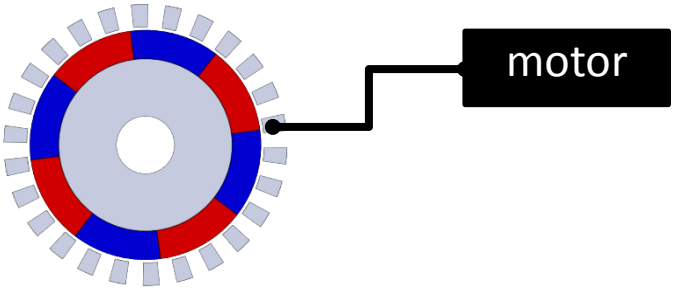

Fig. 1.16 Case where only HSR and Control Rotor are present.

Consider the case where only the HSR and Control Rotor are present, such as in Fig. 1.16. At time t, let the HSR be rotating at an angular velocity of ω_h, and the Control Rotor at ω_s. Essentially, since this is still the same magnetic gear that was explained in section 1.2, the initial equation shown in equation (1.9) expressing the MMF distribution is used again here. However, this time since the steel pieces are rotating too, the permeance distribution of the Control Rotor becomes

$$P(\theta) = P_0 + \sum_{s=1}^{\infty} \frac{B}{(2s-1)} \sin\{(2s-1)N_s(\theta - \omega_s t)\}. \tag{1.13}$$

Multiplying equations (1.9) and (1.13) yields the new flux distribution outside of the Control Rotor, which is

$$\phi\{\theta\} = \sum_{h=1}^{\infty} \frac{AP_0}{(2h-1)} \sin C_1(\theta - \omega_h t) + \sum_{h=1}^{\infty}\sum_{s=1}^{\infty} C_0 \left\{ \cos(C_2 - C_1)\left(\theta - \frac{C_2\omega_s t - C_1\omega_h t}{C_2 - C_1}\right) - \cos(C_2 + C_1)\left(\theta - \frac{C_2\omega_s t + C_1\omega_h t}{C_2 + C_1}\right)\right\}. \quad (1.14)$$

Again, the fundamental component and 2 harmonic components in the flux distribution can be observed. The rotation angle of each component is summarized in Table 1.3.

Table 1.3 Summary of the rotation angles of the flux components

Component Name	Harmonic Order	Rotation Angle
Fundamental Component	$C_1\theta$	$\omega_h t$
Harmonic 1	$C_2 - C_1$	$\frac{C_2\omega_s t - C_1\omega_h t}{C_2 - C_1}$
Harmonic 2	$C_2 + C_1$	$\frac{C_2\omega_s t + C_1\omega_h t}{C_2 + C_1}$

As was stated in section 1.3, to create a magnetic gear, the flux harmonics have to be utilized. This is done by introducing another set of magnets outside of the magnetic pole pieces (see Fig. 1.15(a)) that has the same number of magnetic pole pairs as the harmonic order of either harmonic component outside of the steel pieces. When this happens, the new set of magnets will couple with the selected flux harmonic and their rotation speeds will be in synch as shown in the next equation

$$\frac{C_2\omega_s t \mp C_1\omega_h t}{C_2 \mp C_1} = \omega_l t \quad (1.15)$$

where ω_l is the angular velocity of the new rotor outside.

Differentiating both sides with respect to time yields

$$\frac{C_2\omega_s \mp C_1\omega_h}{C_2 \mp C_1} = \omega_l. \quad (1.16)$$

Since both C_1 and C_2 are constants, equation (1.16) is essentially an equation linking the angular velocities of the HSR (ω_h), Control Rotor (ω_s), and LSR (ω_l). Therefore, if for example the HSR is the input rotor and is rotated at a constant angular velocity, by controlling the angular velocity of the Control Rotor, any arbitrary angular velocity and consequently gear ratio can be obtained at the output rotor, which in this case is the LSR.

As has been shown thus far, Shah's prototype can achieve a continuous gear ratio. However, as can be seen in the experimental setup in Fig. 1.15(b), the Control Rotor (labelled PP shaft in the picture) has to be connected to the servo motor through a large chain reduction gear so that sufficient torque can be generated to rotate the Control Rotor. This defeats the whole purpose of the magnetic gear, which was to transmit torque through non-contact means.

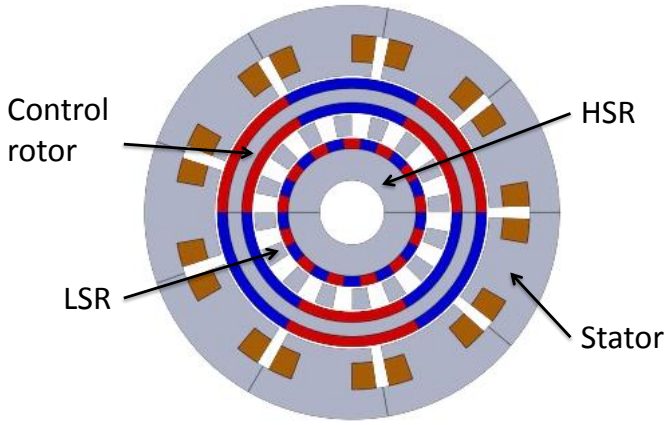

Fig. 1.17 Wang's magnetic gear proposal[12].

Wang's magnetic gear[12] proposal is shown in Fig. 1.17. His magnetic gear can also achieve a continuously variable gear ratio. It uses the same concept as Shah whereby a Control Rotor is used to adjust the gear ratio. However, instead of rotating the Control Rotor mechanically like Shah, Wang installed a set of coils on the outside and magnetically rotates the Control Rotor. This overcomes the problem of mechanical transmission of torque that Shah had. However this model becomes large and complicated. Furthermore, a large amount of permanent magnets is used. Apart from being hard to manufacture, this also increases the manufacturing cost.

1.5 Problem Establishment, Necessity for this Research, and Research Target

Magnetic gears can be used anywhere. However, due to the high costs of rare-earth permanent magnets, it would not be cost-effective to use such a gear in normal vehicles or factory machines. Instead it should be utilized for applications that can take advantage of its 2 biggest assets, which are its virtually maintenance free operation and inherent overload protection property.

One of the applications proposed for the magnetic gear is in wind power generation. Fig. 1.18 illustrates a common system used in wind power generation. The propeller shaft is connected first to a mechanical gear before being connected to a generator. The function of the mechanical gear is to increase the rotation speed of the generator. However, since it is a mechanical gear, it requires regular lubrication and maintenance, experiences a lot of stress during strong winds and is one of the first components to fail. And since medium and large size wind turbines (currently up to 200 m) are installed at places far away from human existence, it becomes clear that maintaining these wind power turbines is costly and time consuming.

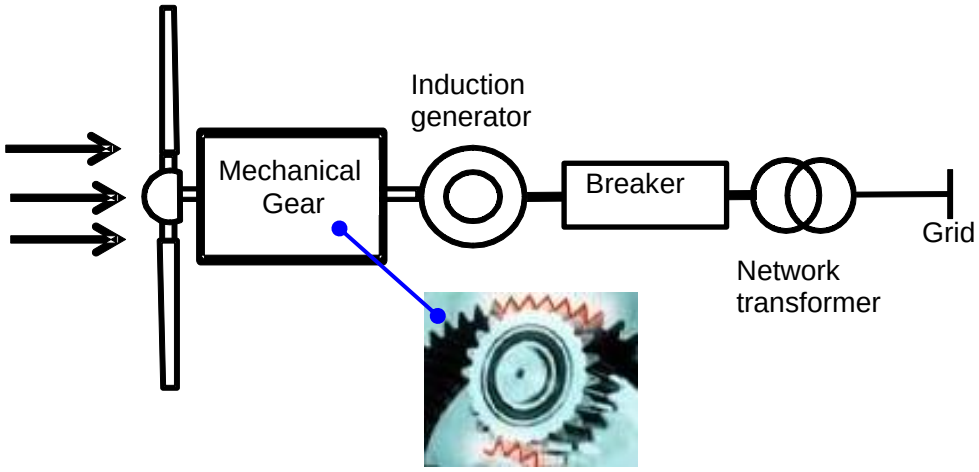

Fig. 1.18 Common system used in wind power generation

Furthermore, the problem with this setup is that the rotation speed of the propellers is solely dependent on the wind speed. This means that on windy days, the propeller rotates very fast and the amount of power and the frequency of the voltage being

generated becomes too high. On the other hand, on relatively quiet days, the propeller rotates too slowly. Not only that, with all the constant changing of the wind speed, the generator is almost never operating at its most efficient speed.

Currently, conventional wind power generation systems try to control the propeller speed by adjusting the angle of the propeller with respect to the wind or try to control the rotation speed of the generator itself using flux weakening systems. Whilst they can reduce the rotation speed of the generator on windy days to bring the operating speed of the generator back to its most efficient point, they cannot increase the rotation speed of the generator.

Using a magnetic gear that has a continuously variable gear ratio can immediately solve these problems. First since the magnetic gear is a non-contact mechanism and does not require regular lubrication, maintenance free operation can be achieved. On top of that, due to its inherent overload protection characteristics, the magnetic gear is safe from breakage during strong winds. Furthermore, having a continuously variable gear ratio means that the rotation speed of the generator can be controlled by the magnetic gear and the generator can always produce electricity at its most efficient rotation speed. Also, no equipment will be necessary to control the angle of the propeller, and thus the overall size of the wind turbine can be reduced.

Although the initial cost of manufacturing a wind turbine utilizing a magnetic gear would be higher than manufacturing a wind turbine utilizing a mechanical gear, money and time saved from not having to maintain the magnetic gear makes it a worthwhile investment in the long run.

As was already mentioned in the previous section, so far, only 3 magnetic gears that have variable gear ratio characteristics have been found in literature. Daif's model[10] had a variable gear ratio but it was discrete and he could only obtain two. Therefore although Daif's model could solve the maintenance and overload problem of the conventional wind power generator setup, it would be impossible to control the speed of the generator so that it is always rotating at its most efficient speed.

Shah's model[11] on the other hand could output a continuous gear ratio. However to achieve this, he used a servo motor that was connected to large mechanical gear chains. This means that although his magnetic gear itself would be maintenance free and immune to overload problems, the control system is not and this idea totally defeats the purpose of developing magnetic gears.

Wang's model[12] is also able to achieve a continuous gear ratio and he did it without using mechanical means. However his model has 3 concentric rotating parts, making the whole system very large and more costly and difficult to manufacture. More importantly, this is unnecessary since the author thinks that only two rotating parts is required. Furthermore, so that the gear ratio of his model could be controllable, due to the operating principle of his particular model, he had to sacrifice his output to input torque ratio. The model in Fig. 1.17 only has a torque ratio of 1.3 : 1. The author thinks that this is far too low for a gear.

The aim of this research is to develop a magnetic gear that can solve the problems of conventional wind power generator systems. The magnetic gear **must:**

1. Have a **continuously variable gear ratio**
2. Have **100% non-contact** mechanism i.e. no mechanical gears, slip rings etc.
3. Have a relatively **high torque ratio**

By developing such a magnetic gear, the author hopes to improve wind powered generator systems so that they are maintenance free and immune to overloading, and that the generator always operates at its most efficient speed. Through this, the author hopes that wind power generation will become a more popular choice for electric power companies and that this research will help in the reduction of the world's reliance on fossil fuels.

1.6 Thesis Outline

This thesis is divided into 5 chapters. The 1st Chapter covers the history of magnetic gears and the aim of this research. Next, since this whole research was conducted using FEM analysis, the 2nd Chapter is dedicated to this topic. In Chapter 3, two magnetic gears that have continuously variable gear ratios are proposed and their characteristics are investigated. In Chapter 4, the power equations of these gears are derived and their efficiencies are determined. In Chapter 5, the main points of this thesis are summarized. Finally, two topics that are connected to the topic of this research: the Vernier motor and a magnetic gear using induced currents, are extensively investigated in the appendix.

References

1. Charles G Armstrong, "Power-transmitting device", US Patent, US687292 A, 1901.
2. Harold T Faus, "Magnet gearing", US Patent, US2243555 A, 1941.
3. Glenn A Reese, "Magnet gearing arrangement", US Patent, US3301091 A, 1967.
4. Martin Jr Thomas B, "Magnetic transmission", US Patent, US3378710 A, 1968.
5. K. Atallah and D. Howe, "A novel high-performance magnetic gear", IEEE Trans. Magn., Vol. 37, No. 2, pp. 2844-2846,2001.
6. P.O. Rasmussen, T.O. Andersen, F.T. Joergensen, O. Nielsen, "Development of a high performance magnetic gear", Industry Applications Conference 38th IAS Annual Meeting. Conference. IEEE Signal Processing Society, pp. 1696 – 1702, 2003.
7. E. Gouda, S. Mezani, L. Baghli, and A. Rezzoug, "Comparative Study Between Mechanical and Magnetic Planetary Gears", IEEE Trans. Magn., Vol.47, No.2, pp.439-450, 2001.
8. N. Frank and H. Toliyat, "Analysis of the Concentric Planetary Magnetic Gear With Strengthened Stator and Interior Permanent Magnet Inner Rotor", IEEE Trans. Ind. App., Vol.47, No.4, pp.1652-1660, 2001.

9. M. Fukuoka, K. Nakamura, O. Ichinokura, “Dynamic Analysis of Planetary-Type Magnetic Gear Based on Reluctance”, IEEE Trans. Magn., Vol.47, No.10, pp.2414-2417, 2011.
10. Mustafa Husain, Katsuhiro Hirata, Noboru Niguchi, “Novel Proposals for the Realization of Variable-Transmission Magnetic Gear”, IEEJ Transactions on Industry Applications, Vol. 131, No. 11, pp. 1263-1268, 2011.
11. L. Shah, A. Cruden, B.W. Williams, “A Variable Speed Magnetic Gear Box Using Contra-Rotating Input Shafts”, IEEE Trans. Magn., Vol. 47, No. 2, pp. 431-438, 2011.
12. Jiabin Wang, K. Atallah, S.D. Carvley, “A Magnetic Continuously Variable Transmission Device”, IEEE Trans. Magn., Vol. 47, No. 10, pp. 2815-2818, 2011.

Chapter 2 FEM Analysis for Determining Model Characteristics

2.1 Introduction

The work in this chapter is based on [1].

A well–established method for determining the characteristics of electromagnetic devices was to create the equivalent circuit model. However this method is not accurate since the flux flow of the electric machine is only approximated. Furthermore, since this method only calculates the average torque value over one electrical period, it is impossible to evaluate fluctuations in the torque. Therefore, in this research, Finite Element Method (FEM) is used to solve Maxwell's equations of electromagnetism, to accurately evaluate the torque characteristics of an electromagnetic device.

This chapter explains the method for determining the torque characteristics of an electric machine using FEM. First, from Maxwell's equations, the basic magnetic field equations of the A–method and Ω–method is derived. Then, as an example of calculation using Galerkin's method, the calculation method using tetrahedral elements by the A–method is described. Then, CG and ICCG methods that are used for solving linear simultaneous equations, the Newton–Raphson method when considering the nonlinearity of materials, and the Maxwell Stress Tensor and Nodal Force Methods for calculating the electromagnetic force will be described.

Section 2.3 explains how the magnetic field analysis is coupled to the equation of motion and how the equation is solved. Section 2.4 describes the method for correcting the mesh partitions when the rotor of the electromagnetic device is rotating.

2.2 Magnetic Field Analysis

2.2.1 Derivation of the Fundamental Equations

All electromagnetic phenomena can be explained by the following 4 equations, also known as Maxwell's equations

$$\mathrm{rot}\boldsymbol{H} = \boldsymbol{J} + \frac{\partial \boldsymbol{D}}{\partial t} \tag{2.1}$$

$$\mathrm{rot}\boldsymbol{E} = -\frac{\partial \boldsymbol{B}}{\partial t} \tag{2.2}$$

$$\mathrm{div}\boldsymbol{B} = 0 \tag{2.3}$$

$$\mathrm{div}\boldsymbol{D} = \rho \tag{2.4}$$

where $\boldsymbol{H}$ is the magnetic field intensity, $\boldsymbol{J}$ is the current density, $\boldsymbol{D}$is the flux density, $\boldsymbol{E}$ is the electrical field intensity, $\boldsymbol{B}$ is the flux density, ρ is the electrical charge density. Also, the relationships between $\boldsymbol{B}$ and $\boldsymbol{H}$, $\boldsymbol{D}$ and $\boldsymbol{E}$, $\boldsymbol{J}$ and $\boldsymbol{E}$ in a certain medium can be described by the following equations

$$\boldsymbol{B} = \mu \boldsymbol{H} \tag{2.5}$$

$$\boldsymbol{D} = \varepsilon \boldsymbol{E} \tag{2.6}$$

$$\boldsymbol{J} = \sigma \boldsymbol{E} \tag{2.7}$$

where μ is the magnetic permeability, ε is the permittivity, σ is the electrical conductivity of that medium.

Next, when div rot$\boldsymbol{A}$=0 is substituted into equation (2.3), equation (2.8) is obtained, where $\boldsymbol{A}$ is defined as the magnetic vector potential.

$$\boldsymbol{B} = \mathrm{rot}\boldsymbol{A} \tag{2.8}$$

Also, flux density $\boldsymbol{B}$ is a function of the magnetic field intensity $\boldsymbol{H}$ and can be expressed in equation (2.9).

$$\boldsymbol{B} = \mu \boldsymbol{H} = \frac{1}{\nu} \boldsymbol{H} \tag{2.9}$$

where ν is the reluctivity of the magnetic material.

By applying Stoke's theorem to Ampere's circuital law, Ampere's circuital law in its

differential form is obtained, and is shown in equation (2.10)

$$\mathrm{rot}\boldsymbol{H} = \boldsymbol{J}_0 \tag{2.10}$$

where $\boldsymbol{J_0}$ is the density of the current flowing into the area.

Substituting equations (2.8) and (2.9) into equation (2.10) yields equation (2.11), which is the fundamental equation for static magnetic field analysis.

$$\mathrm{rot}(\nu\mathrm{rot}\boldsymbol{A}) = \boldsymbol{J}_0 \tag{2.11}$$

The magnetic flux density in the permanent magnet $\boldsymbol{B}$, magnetic field intensity $\boldsymbol{H}$, and the magnetization of the permanent magnet $\boldsymbol{M}$ can be expressed using equation (2.12).

$$\boldsymbol{B} = \mu\boldsymbol{H} + \boldsymbol{M} \quad \Leftrightarrow \quad \boldsymbol{H} = \frac{1}{\mu}(\boldsymbol{B} - \boldsymbol{M}) \tag{2.12}$$

Substituting equation (2.12) into equation (2.10) yields equation (2.13).

$$\mathrm{rot}\boldsymbol{H} = \mathrm{rot}\frac{1}{\mu}(\boldsymbol{B} - \boldsymbol{M}) = \boldsymbol{J}_0 \tag{2.13}$$

Substituting equation (2.8) into equation (2.13) yields equation (2.14), which is the fundamental equation inside of the permanent magnet.

$$\mathrm{rot}(\nu\mathrm{rot}\boldsymbol{A}) = \boldsymbol{J}_0 + \nu\mathrm{rot}\boldsymbol{M} \tag{2.14}$$

where ν is the magnetic reluctivity of vacuum and $\nu_0\mathrm{rot}\boldsymbol{M}$ is defined as $\boldsymbol{J}_m$, which is the equivalent magnetization current density.

From the above, for cases where eddy currents are not generated, equation (2.14) holds true for areas inside the permanent magnet of the electromagnetic device, whilst equation (2.11) is used for all the other areas. The magnetic vector potential $\boldsymbol{A}$ is solved for as an unknown quantity, and this method is called the A–method.

2.2.2 Discretization Using Galerkin's Method

To solve the linear magnetic vector potential equation shown in equation (2.14), the analysis area has to be divided into many small discrete areas (discretization) called "elements", and the potential distribution of each element is approximated as simple functions. Calculations of each small area are done throughout the whole analysis area,

and this analysis method is called the Finite Element Method. One method for deriving discretized equations in FEM is to use Galerkin's method.

If we let the differential equation of the magnetic vector potential $\boldsymbol{A}$ be $f(\boldsymbol{A}) = 0$, then

$$f(\boldsymbol{A}) = \mathrm{rot}(\nu \mathrm{rot}\boldsymbol{A}) - \boldsymbol{J}_0 - \boldsymbol{J}_m \tag{2.15}$$

Then, let the approximate solution of this equation be $\boldsymbol{A}'$. Substituting this into equation (2.15) does not equal zero ($f(\boldsymbol{A}') = 0$) but instead yields a residual $\boldsymbol{R}$, as shown in equation (2.16).

$$f(\boldsymbol{A}') = \boldsymbol{R} \tag{2.16}$$

The integration of the residual over the whole area should be zero. The method of using the weight function $\boldsymbol{N}_i$ that approximates the magnetic vector potential, for making the weighted integral value for the residual $\boldsymbol{R}$ over the whole analysis area zero is called Galerkin's method. The residual's equation is shown in equation (2.17).

$$G_i = \iiint_V \boldsymbol{N}_i \cdot f(\boldsymbol{A}) \mathrm{d}V = 0 \tag{2.17}$$

The weight function $\boldsymbol{N}_i$ in equation (2.17) is called the interpolation function.

Next, the interpolation function for when the analysis area has been divided into 1st order tetrahedral elements is determined. First, we shall consider a 1st order tetrahedral nodal element as shown in Fig. 2.1(a). Each 1st order tetrahedral nodal element contains 4 nodes and on each node there are the magnetic vector potentials A_x, A_y, A_z. In the field of electromagnetism, the flux density $\boldsymbol{B}$'s normal component and the magnetic field $\boldsymbol{H}$'s tangent component are continuous at the boundary plane of dissimilar ferromagnetic materials. However, for 1st order tetrahedral nodal elements, all of $\boldsymbol{A}$'s components becomes continuous at the nodes of the boundary plane of dissimilar materials. As a result even $\boldsymbol{B}$'s tangent component becomes continuous, making this physically incorrect.

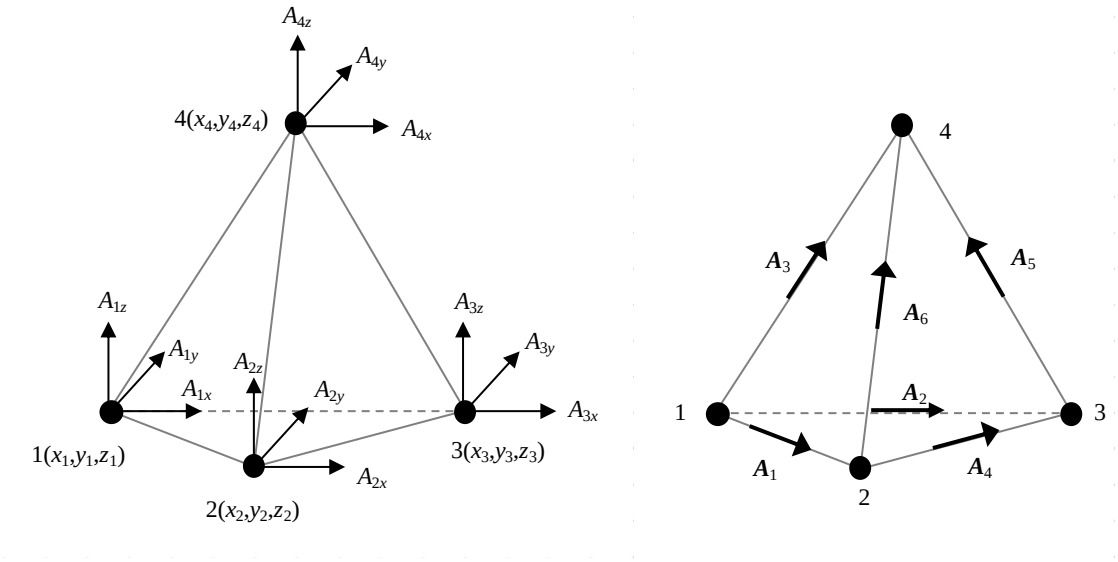

(a) Nodal element (b) Edge element

Fig. 2.1 Definition of unknown variables.

Therefore, instead of using 1st order tetrahedral nodal elements, 1st order tetrahedral edge elements, as shown in Fig. 2.1(b), are used. The vector component of the vector potential $\boldsymbol{A}$ projected onto edge k is integrated along edge k, and these integrals are the unknowns A_k (k=1, 2, 3, 4, 5, 6).

$$A_k = \int_k \boldsymbol{A} \cdot d\boldsymbol{s} \tag{2.18}$$

where $\boldsymbol{s}$ is a vector along the particular edge. Here, the interpolation function $\boldsymbol{N}_k$ of edge k is determined as follows.

$$\int_m \boldsymbol{N}_k \cdot d\boldsymbol{s} = \begin{cases} 1 & (m = k) \\ 0 & (m \neq k) \end{cases} \tag{2.19}$$

From equation (2.19), we can see that when $\boldsymbol{N}_k$ is integrated along edge k we get 1, and when it is integrated along the other edges we get 0. Here, the interpolation function that links node i and node j together is defined as follows.

$$\boldsymbol{N}_k = \frac{1}{36V^2}\left\{(b_i + c_i x + d_i y + e_i z)\left(\boldsymbol{i}c_j + \boldsymbol{j}d_j + \boldsymbol{k}e_j\right) - \left(b_j + c_j x + d_j y + e_j z\right)(\boldsymbol{i}c_i + \boldsymbol{j}d_i + \boldsymbol{k}e_i)\right\} \tag{2.20}$$

$$b_i = (-1)^i \left\{x_j\left(y_n z_m - y_m z_n\right) + x_m\left(y_j z_n - y_n z_j\right) + x_n\left(y_m z_j - y_j z_m\right)\right\} \tag{2.21}$$

$$c_i = (-1)^i \left\{y_j\left(z_m - z_n\right) + y_m\left(z_n - z_j\right) + y_n\left(z_j - z_m\right)\right\} \tag{2.22}$$

$$d_i = (-1)^i \{z_j(x_m - x_n) + z_m(x_n - x_j) + z_n(x_j - x_m)\} \tag{2.23}$$

$$e_i = (-1)^i \{x_j(y_m - y_n) + x_m(y_n - y_j) + x_n(y_j - y_m)\} \tag{2.24}$$

$$V = \frac{1}{6}(x_1 c_1 + x_2 c_2 + x_3 c_3 + x_4 c_4) \tag{2.25}$$

where $\boldsymbol{i}$, $\boldsymbol{j}$, $\boldsymbol{k}$ are unit vectors in the x, y, z direction respectively, and i, j, k, m are subscripts. When i is 2, j=3, m=4, n=1. Here, the magnetic vector potential $\boldsymbol{A}$ of the tetrahedral element becomes as follows.

$$\boldsymbol{A} = \sum_{k=1}^{6} \boldsymbol{N}_k A_k \tag{2.26}$$

Now since the interpolation function $\boldsymbol{N}_k$ has been determined, it is now possible to conduct calculations using Galerkin's method.

Let us consider a field that contains a permanent magnet. Equation (2.17) can be expressed as (2.27).

$$G_k = \iiint_V \boldsymbol{N}_k \cdot \mathrm{rot}(\nu \mathrm{rot}\boldsymbol{A})\mathrm{d}V - \iiint_V \boldsymbol{N}_k \cdot \boldsymbol{J_0}\mathrm{d}V - \iiint_V \nu \boldsymbol{N}_k \cdot \mathrm{rot}\boldsymbol{M}\mathrm{d}V \tag{2.27}$$

Substituting the first term on the right side of equation (2.27) with the following vector formula div($\boldsymbol{a}\times\boldsymbol{b}$) = $\boldsymbol{b}\cdot$rot $\boldsymbol{a}$ – $\boldsymbol{a}\cdot$rot $\boldsymbol{b}$, gives equation (2.28).

$$\iiint_V \boldsymbol{N}_k \cdot \mathrm{rot}(\nu \mathrm{rot}\boldsymbol{A})\mathrm{d}V = \iiint_V \nu \mathrm{rot}\boldsymbol{A} \cdot \mathrm{rot}\boldsymbol{N}_k \mathrm{d}V + \iiint_V \nu \mathrm{rot}\boldsymbol{A} \times \boldsymbol{N}_k \mathrm{d}V \tag{2.28}$$

Then, if we apply Gauss' divergence theorem to the second term of the right side of equation (2.28), we obtain

$$\iiint_V \nu \mathrm{rot}\boldsymbol{A} \times \boldsymbol{N}_k \mathrm{d}V = \iint_S (\nu \mathrm{rot}\boldsymbol{A} \times \boldsymbol{N}_k) \cdot \boldsymbol{n}\mathrm{d}S \tag{2.29}$$

And applying the vector formula $\boldsymbol{a}\cdot(\boldsymbol{b}\times\boldsymbol{c}) = \boldsymbol{b}\cdot(\boldsymbol{c}\times\boldsymbol{a}) = \boldsymbol{c}\cdot(\boldsymbol{a}\times\boldsymbol{b})$ to equation (2.29) yields

$$\iint_S (\nu \mathrm{rot}\boldsymbol{A} \times \boldsymbol{N}_k) \cdot \boldsymbol{n}\mathrm{d}S = \iint_S (\boldsymbol{n} \times \nu \mathrm{rot}\boldsymbol{A}) \cdot \boldsymbol{N}_k \mathrm{d}S \tag{2.30}$$

Looking at the right side of equation (2.30), since $\boldsymbol{n}\times\nu$ rot$\boldsymbol{A} = \boldsymbol{n}\times\nu\boldsymbol{B} = \boldsymbol{n}\times\boldsymbol{H}$, when the magnetic field intensity $\boldsymbol{H}$ is perpendicular to the boundary plane (natural boundaries), $\boldsymbol{n}\times\boldsymbol{H} = 0$ (outer product). And when the magnetic field intensity $\boldsymbol{H}$ is parallel to the

boundary plane (fixed boundaries), the magnetic vector potential at the plane becomes a known value, and thus it is no longer necessary to create equations using Galerkin's method, and we can just substitute it with $\mathbf{0}$. Also, since there is no forced current, $\boldsymbol{J}_0 = \mathbf{0}$. Therefore, equation (2.27) can be expressed as follows

$$G_k = \int\int\int_V \nu \mathrm{rot}\boldsymbol{A} \cdot \mathrm{rot}\boldsymbol{N}_k \mathrm{d}V - \int\int\int_V \nu_0 \boldsymbol{N}_k \cdot \mathrm{rot}\boldsymbol{M} \mathrm{d}V \tag{2.31}$$

Here, if we let the interpolation function $\boldsymbol{N}_k$ become the interpolation function of edge k, which connects node 1 with node 2, $\boldsymbol{N}_k$ can be expanded into equation (2.32).

$$\begin{aligned} \boldsymbol{N}_k &= \frac{1}{36V^2}\left\{(b_i + c_i x + d_i y + e_i z)\left(\boldsymbol{i}c_j + \boldsymbol{j}d_j + \boldsymbol{k}e_j\right) - \left(b_j + c_j x + d_j y + e_j z\right)(\boldsymbol{i}c_i + \boldsymbol{j}d_i + \boldsymbol{k}e_i)\right\} \\ &= \frac{1}{36V^2}\begin{Bmatrix} (b_{k1} + c_{k1} x + d_{k1} y + e_{k1} z)(\boldsymbol{i}c_{k2} + \boldsymbol{j}d_{k2} + \boldsymbol{k}e_{k2}) \\ -(b_{k2} + c_{k2} x + d_{k2} y + e_{k2} z)(\boldsymbol{i}c_{k1} + \boldsymbol{j}d_{k1} + \boldsymbol{k}e_{k1}) \end{Bmatrix} \end{aligned} \tag{2.32}$$

Then, expanding and reorganizing equation (2.32) according to $\boldsymbol{i}$, $\boldsymbol{j}$, $\boldsymbol{k}$ yields

$$\begin{aligned} \left(\mathrm{rot}\boldsymbol{N}_k\right)_x &= \frac{\partial\left(\boldsymbol{N}_k\right)_z}{\partial y} - \frac{\partial\left(\boldsymbol{N}_k\right)_y}{\partial z} \\ &= \frac{1}{36V^2}\left[\frac{\partial}{\partial y}\left\{b_{k1}e_{k2} - b_{k2}e_{k1} + \left(c_{k1}e_{k2} - c_{k2}e_{k1}\right)x + \left(d_{k1}e_{k2} - d_{k2}e_{k1}\right)y\right\}\right. \\ &\quad \left. - \frac{\partial}{\partial z}\left\{b_{k1}d_{k2} - b_{k2}d_{k1} + \left(c_{k1}d_{k2} - c_{k2}d_{k1}\right)x + \left(e_{k1}d_{k2} - e_{k2}d_{k1}\right)z\right\}\right] \\ &= \frac{1}{18V^2}\left(d_{k1}e_{k2} - d_{k2}e_{k1}\right) \end{aligned} \tag{2.33}$$

$$\left(\mathrm{rot}\boldsymbol{N}_k\right)_y = \frac{1}{18V^2}\left(e_{k1}c_{k2} - e_{k2}c_{k1}\right) \tag{2.34}$$

$$\left(\mathrm{rot}\boldsymbol{N}_k\right)_z = \frac{1}{18V^2}\left(c_{k1}d_{k2} - c_{k2}d_{k1}\right) \tag{2.35}$$

Substituting equation (2.26) into the first term of the right side of equation (2.31) gives

$$\begin{aligned} \iiint_V \nu \mathrm{rot}\boldsymbol{A} \cdot \mathrm{rot}\boldsymbol{N}_k \mathrm{d}V &= \iiint_V \mathrm{rot}\boldsymbol{N}_k \cdot \left\{\nu \mathrm{rot} \sum_{u=1}^{6}\left(\boldsymbol{N}_u A_u\right)\right\}\mathrm{d}V \\ &= \iiint_V \mathrm{rot}\boldsymbol{N}_k \cdot \left\{\nu \sum_{u=1}^{6} \mathrm{rot}\boldsymbol{N}_u A_u\right\}\mathrm{d}V \end{aligned} \tag{2.36}$$

Then, rewriting the vector parts of equation (2.36) into x, y, z components gives

$$\begin{aligned}&\iiint_V \mathrm{rot}\boldsymbol{N}_k \cdot \left\{ \nu \sum_{u=1}^{6} \mathrm{rot}\boldsymbol{N}_u A_u \right\} \mathrm{d}V \\ &= \iiint_V \sum_{u=1}^{6} \left(\frac{1}{18V^2} \right)^2 \begin{Bmatrix} \nu_x (d_{k1}e_{k2} - e_{k1}d_{k2})(d_{u1}e_{u2} - e_{u1}d_{u2}) \\ +\nu_y (e_{k1}c_{k2} - c_{k1}e_{k2})(e_{u1}c_{u2} - c_{u1}e_{u2}) \\ +\nu_z (c_{k1}d_{k2} - d_{k1}c_{k2})(c_{u1}d_{u2} - d_{u1}c_{u2}) \end{Bmatrix} A_u \mathrm{d}V\end{aligned} \tag{2.37}$$

Here, if we apply equation (2.38) to equation (2.37), and integrate the whole analysis area, the first term of the right side of equation (2.31) becomes equation (2.39).

$$\iiint_V \mathrm{d}V = V \tag{2.38}$$

$$\sum_V \frac{1}{324V^3} \sum_{u=1}^{6} \begin{Bmatrix} \nu_x (d_{k1}e_{k2} - e_{k1}d_{k2})(d_{u1}e_{u2} - e_{u1}d_{u2}) \\ +\nu_y (e_{k1}c_{k2} - c_{k1}e_{k2})(e_{u1}c_{u2} - c_{u1}e_{u2}) \\ +\nu_z (c_{k1}d_{k2} - d_{k1}c_{k2})(c_{u1}d_{u2} - d_{u1}c_{u2}) \end{Bmatrix} A_u \tag{2.39}$$

Next, applying the vector formula $\mathrm{div}(\boldsymbol{a} \times \boldsymbol{b}) = \boldsymbol{b} \cdot \mathrm{rot}\,\boldsymbol{a} - \boldsymbol{a} \cdot \mathrm{rot}\,\boldsymbol{b}$ and Gauss' divergence theorem to the second term of the right side of equation (2.31) gives equation (2.40).

$$-\iiint_V \nu \boldsymbol{N}_k \cdot \mathrm{rot}\boldsymbol{M} \mathrm{d}V = -\nu \iint_S (\boldsymbol{M} \times \boldsymbol{N}_k) \cdot \boldsymbol{n} \mathrm{d}S - \nu \iiint_V \boldsymbol{M} \cdot \mathrm{rot}\boldsymbol{N}_k \mathrm{d}V \tag{2.40}$$

Applying the vector formula $\boldsymbol{a} \cdot (\boldsymbol{b} \times \boldsymbol{c}) = \boldsymbol{b} \cdot (\boldsymbol{c} \times \boldsymbol{a}) = \boldsymbol{c} \cdot (\boldsymbol{a} \times \boldsymbol{b})$ to the first term of the right side of equation (2.40) gives

$$-\nu \iint_S (\boldsymbol{M} \times \boldsymbol{N}_k) \cdot \boldsymbol{n} \mathrm{d}S = -\nu \iint_S (\boldsymbol{n} \times \boldsymbol{M}) \cdot \boldsymbol{N}_k \mathrm{d}S \tag{2.41}$$

When the magnetization $\boldsymbol{M}$ is perpendicular with the boundary plane S, it is parallel to $\boldsymbol{n}$, and $\boldsymbol{n} \times \boldsymbol{M}$ becomes $\boldsymbol{0}$ (natural boundary). In other words, with regards to $\boldsymbol{A}$, by making equation (2.41) become $\boldsymbol{0}$, $\boldsymbol{M}$ becomes perpendicular to the boundary plane S, and setting it as $\boldsymbol{0}$ ensures that no contradiction occurs. Therefore equation (2.41) becomes $\boldsymbol{0}$, and only the second term of equation (2.40) remains.

$$-\nu \iiint_V \boldsymbol{M} \cdot \mathrm{rot}\boldsymbol{N}_k \mathrm{d}V = -\nu \iiint_V \left\{ \boldsymbol{M}_x (\mathrm{rot}\boldsymbol{N}_k)_x + \boldsymbol{M}_y (\mathrm{rot}\boldsymbol{N}_k)_y + \boldsymbol{M}_z (\mathrm{rot}\boldsymbol{N}_k)_z \right\} \mathrm{d}V \tag{2.42}$$

Using equation (2.38), integrating equation (2.42) over the whole analysis area yields equation (2.43).

$$-\sum_{V}\frac{\nu}{18V}\left\{\left(d_{k1}e_{k2}-e_{k1}d_{k2}\right)M_x+\left(e_{k1}c_{k2}-c_{k1}e_{k2}\right)M_y+\left(c_{k1}d_{k2}-d_{k1}c_{k2}\right)M_z\right\} \tag{2.43}$$

Then if we substitute equations (2.39) and (2.43) into equation (2.31)

$$\begin{aligned}&\sum_{V}\frac{1}{324V^3}\sum_{u=1}^{6}\left\{\begin{array}{l}\nu_x\left(d_{k1}e_{k2}-e_{k1}d_{k2}\right)\left(d_{u1}e_{u2}-e_{u1}d_{u2}\right)\\+\nu_y\left(e_{k1}c_{k2}-c_{k1}e_{k2}\right)\left(e_{u1}c_{u2}-c_{u1}e_{u2}\right)\\+\nu_z\left(c_{k1}d_{k2}-d_{k1}c_{k2}\right)\left(c_{u1}d_{u2}-d_{u1}c_{u2}\right)\end{array}\right\}A_u\\&-\sum_{V}\frac{\nu}{18V}\left\{\left(d_{k1}e_{k2}-e_{k1}d_{k2}\right)M_x+\left(e_{k1}c_{k2}-c_{k1}e_{k2}\right)M_y+\left(c_{k1}d_{k2}-d_{k1}c_{k2}\right)M_z\right\}=0\end{aligned} \tag{2.44}$$

Arranging equation (2.44) into its matrix form gives us equation (2.45)

$$\begin{bmatrix}H_{11} & \cdots & H_{1n}\\ \vdots & \ddots & \vdots\\ H_{n1} & \cdots & H_{nn}\end{bmatrix}\begin{Bmatrix}A_1\\ \vdots\\ A_n\end{Bmatrix}=\begin{Bmatrix}K_1\\ \vdots\\ K_n\end{Bmatrix} \tag{2.45}$$

Here, n is the number of edges when the whole analysis area has been discretized, and matrix H is a $n\times n$ symmetric matrix. Equation (2.45) is an n^{th} order linear equation of A_k, and so the number of unknowns is also n, and therefore is solvable. In electromagnetic analysis, we take advantage of the symmetric property of the matrix H and use an iterative method such as the CG method (conjugate gradient method) or the ICCG method (incomplete Cholesky conjugate gradient method) to solve the matrix.

The CG method shall be described. Equation (2.45) is written as $[H]\{A\}=\{K\}$. First, let the initial solution of $\{A\}$ be $\{A_0\}$, and define the search direction vector $\{P_0\}$ as equation (2.46).

$$\{P_0\}=\{r_0\}=\{K\}-[H]\{A_0\} \tag{2.46}$$

At iteration number r+1, let the solution be $\{A_{r+1}\}$ as is shown in equation (2.47).

$$\{A_{r+1}\}=\{A_r\}+\alpha_r\{P_r\} \tag{2.47}$$

Here,

$$\alpha_r=\frac{\{P_r\}^t\{R_r\}}{\{P_r\}^t\{H\}\{P_r\}} \tag{2.48}$$

$$\{R_{r+1}\}=\{R_r\}-\alpha_r[H]\{P_r\} \tag{2.49}$$

$$\{P_{r+1}\}=\{R_{r+1}\}+\beta_r\{P_r\} \tag{2.50}$$

$$\beta_r = \frac{\{R_{r+1}\}^t \{H\}\{P_r\}}{\{P_r\}^t \{H\}\{P_r\}} \tag{2.51}$$

Here, when equation (2.52) reaches a value below the permissible value, $\{A_i\}$ is the solution for $\{A\}$.

$$\phi(A_i) = \frac{1}{2}\{A_i\}^t [H]\{A_i\} - \{A_i\}\{K\} \tag{2.52}$$

On the other hand, in the ICCG method, incomplete Cholesky decomposition is conducted, and the approximate inverse matrix, $[H^*]^{-1}$, of $[H]$ in $[H]\{A\}=\{K\}$is determined. Multiplying both sides by $[H^*]^{-1}$,we obtain

$$\left[H^*\right]^{-1}[H]\{A\} = \left[H^*\right]^{-1}\{K\} \tag{2.53}$$

Then, equation (2.53) is defined as follows

$$\left[H^*\right]^{-1}[H]\{A\} = [\tilde{H}]\{A\} = \left[H^*\right]^{-1}\{K\} = \{\tilde{K}\} \tag{2.54}$$

Iterative calculations using the CG method conducted on equation (2.54) is called the ICCG method. Although with this method it becomes necessary to first calculate the approximate inverse matrix, the iterative calculations converge faster.

2.2.3 Non-Linearity of the Material

The non-linearity of the direct current magnetizing characteristics of ferromagnetic materials is solved using iterative calculation methods and one such method is called the Newton-Raphson Method. In this method, each element is initially given a rough magnetic permeability value and the magnetic permeability is calculated using FEM. Then, from the obtained results after one calculation, the magnetic permeability is revised, and the calculation is performed again. This is repeated until the value converges.

Let the estimated solution of $f(x,y) = 0$, $g(x,y) = 0$ at the u^{th} iteration be $x^{(u)}$, $y^{(u)}$ respectively. If we apply the Taylor expansion to $f(x,y)$ and $g(x,y)$ respectively, the following equations are obtained.

$$f\left(x^{(u)}+\delta x^{(u)}, y^{(u)}+\delta y^{(u)}\right)= f\left(x^{(u)}, y^{(u)}\right)+\frac{\partial}{\partial x^{(u)}} f\left(x^{(u)}, y^{(u)}\right)\delta x^{(u)}+\frac{\partial}{\partial y^{(u)}} f\left(x^{(u)}, y^{(u)}\right)\delta y^{(u)}+\cdots \quad (2.55)$$

$$g\left(x^{(u)}+\delta x^{(u)}, y^{(u)}+\delta y^{(u)}\right)= g\left(x^{(u)}, y^{(u)}\right)+\frac{\partial}{\partial x^{(u)}} g\left(x^{(u)}, y^{(u)}\right)\delta x^{(u)}+\frac{\partial}{\partial y^{(u)}} g\left(x^{(u)}, y^{(u)}\right)\delta y^{(u)}+\cdots \quad (2.56)$$

Terms with exponentials of 2 and above in equation (2.55) and equation (2.56) are ignored, and $x = x^{(u)} + \delta x^{(u)}$, $y = y^{(u)} + \delta y^{(u)}$ is the true solution. Therefore $f(x^{(u)} + \delta x^{(u)}, y^{(u)} + \delta y^{(u)}) = 0$, $g(x^{(u)} + \delta x^{(u)}, y^{(u)} + \delta y^{(u)}) = 0$, and the left side of equations (2.55) and (2.56) become 0. Then, if we let $f(x^{(u)} + y^{(u)})$ and $g(x^{(u)} + y^{(u)})$ from equations (2.55) and (2.56) be $f^{(u)}$ and $g^{(u)}$ respectively, and rewrite them in the matrix form whilst ignoring 2nd degree polynomials and above, we obtain

$$\begin{bmatrix} \dfrac{\partial f^{(u)}}{\partial x^{(u)}} & \dfrac{\partial f^{(u)}}{\partial y^{(u)}} \\ \dfrac{\partial g^{(u)}}{\partial x^{(u)}} & \dfrac{\partial g^{(u)}}{\partial y^{(u)}} \end{bmatrix} \begin{Bmatrix} \delta x^{(u)} \\ \delta y^{(u)} \end{Bmatrix} = \begin{Bmatrix} -f^{(u)} \\ -g^{(u)} \end{Bmatrix} \quad (2.57)$$

$\delta x^{(u)}$, $\delta y^{(u)}$ is obtained by solving (2.57). And, from the following equations

$$x^{(u+1)} = x^{(u)} + \delta x^{(u)} \quad (2.58)$$

$$y^{(u+1)} = y^{(u)} + \delta y^{(u)} \quad (2.59)$$

the $u+1^{th}$ approximate solution is obtained.

In Galerkin's method, the residual equation $G_k = 0$ is solved and the magnetic vector potential is obtained. In other words $f(x,y) = 0$ is equivalent to $G_k = 0$. Therefore rewriting equation (2.57) gives us

$$\begin{bmatrix} \dfrac{\partial G_1}{\partial A_1} & \cdots & \dfrac{\partial G_1}{\partial A_n} \\ \vdots & \dfrac{\partial G_k}{\partial A_m} & \vdots \\ \dfrac{\partial G_n}{\partial A_1} & \cdots & \dfrac{\partial G_n}{\partial A_n} \end{bmatrix} \begin{Bmatrix} \delta A_1 \\ \vdots \\ \delta A_k \\ \vdots \\ \delta A_n \end{Bmatrix} = \begin{Bmatrix} -G_1 \\ \vdots \\ -G_k \\ \vdots \\ -G_n \end{Bmatrix} \quad (2.60)$$

If we let A_k, G_k be the value for the u^{th} iteration, then from equation (2.61),

$$A_k^{(u+1)} = A_k^{(u)} + \delta A_k^{(u)} \quad (2.61)$$

the approximate solution $A_k^{(u+1)}$ of the magnetic vector potential of the edge k obtained at the $u+1^{th}$ iteration is acquired. Here, when the absolute value of δA_k goes below the

specified value, the analysis is judged to have converged.

2.2.4 Electromagnetic Force Calculation Method

Maxwell's Stress method and the Nodal Force method are 2 common ways for determining the electromagnetic force. Maxwell's Stress method is a method of using the Maxwell stress tensor that was obtained from the flux density of a closed surface S, to determine the total Maxwell stress applied to said closed surface S. The electromagnetic force here is shown in equation (2.62).

$$\boldsymbol{F} = \iint_S \boldsymbol{T} \cdot \boldsymbol{n} dS \tag{2.62}$$

where $\boldsymbol{n}$ is the normal unit vector of S and $\boldsymbol{T}$ is Maxwell stress tensor, which is shown in equation (2.63).

$$\boldsymbol{T} = \begin{bmatrix} B_x^2 - B_y^2 - B_z^2 & 2B_xB_y & 2B_xB_z \\ 2B_yB_x & B_y^2 - B_z^2 - B_x^2 & 2B_yB_z \\ 2B_zB_x & 2B_zB_y & B_z^2 - B_x^2 - B_y^2 \end{bmatrix} \tag{2.63}$$

The accuracy of the analysis is greatly influenced by the selection of the closed surface S. Since the flux changes drastically at the boundary of a magnetic body and air, the closed surface S is set at a place that is far enough from any ferromagnetic bodies, which does not experience drastic changes in flux.

Torque T is calculated using equation (2.64).

$$T = \iint_S \boldsymbol{t} \cdot \boldsymbol{T} \cdot \boldsymbol{n} |\boldsymbol{r}| \mathrm{d}S \tag{2.64}$$

where $\boldsymbol{t}$ is the rotational direction unit vector, and $\boldsymbol{r}$ is the normal vector of the closed area whose torque we would like to calculate ($|\boldsymbol{r}|$ expresses the distance from the rotation axis).

On the other hand, the Nodal Force method is a method where the total force acting on the whole of the magnetic body is calculated by adding up the individual forces that act on each node inside the said magnetic body. Unlike Maxwell's stress method, it is not important how a closed surface S is selected. Furthermore, the electromagnetic

force inside the magnetic body can also be calculated.

First, the Maxwell Stress tensor is expressed in equation (2.65)

$$\boldsymbol{T} = \begin{bmatrix} B_x^2 - B_y^2 - B_z^2 & 2B_xB_y & 2B_xB_z \\ 2B_yB_x & B_y^2 - B_z^2 - B_x^2 & 2B_yB_z \\ 2B_zB_x & 2B_zB_y & B_z^2 - B_x^2 - B_y^2 \end{bmatrix} = \begin{bmatrix} T_{xx} & T_{xy} & T_{xz} \\ T_{yx} & T_{yy} & T_{yz} \\ T_{zx} & T_{zy} & T_{zz} \end{bmatrix} \tag{2.65}$$

Here, if tetrahedral elements are used, the total electromagnetic force acting on node i is calculated. If tetrahedral nodal elements are used, since the interpolation equation N_i is given in equation (2.66), using equation (2.38) yields the total electromagnetic force, which is expressed in equations (2.67), (2.68) and (2.69).

$$N_i = \frac{1}{6V}\left(b_i + c_i x + d_i y + e_i z\right) \tag{2.66}$$

$$f_{xi} = -\frac{1}{6V}\iiint_V \left(T_{xx}c_i + T_{xy}d_i + T_{xz}e_i\right)\mathrm{d}V = -\frac{1}{6}\sum_{V_i}\left(T_{xx}c_i + T_{xy}d_i + T_{xz}e_i\right) \tag{2.67}$$

$$f_{yi} = -\frac{1}{6}\sum_{V_i}\left(T_{yx}c_i + T_{yy}d_i + T_{yz}e_i\right) \tag{2.68}$$

$$f_{zi} = -\frac{1}{6}\sum_{V_i}\left(T_{zx}c_i + T_{zy}d_i + T_{zz}e_i\right) \tag{2.69}$$

where the V_i in equations (2.67), (2.68) and (2.69) is the sum of the all the elements including node i.

Torque is calculated using equation (2.70)

$$T = \sum_i^n r_i \boldsymbol{t}_i \cdot \boldsymbol{f}_i \tag{2.70}$$

where r_i is the distance of node i from the rotation axis, and $\boldsymbol{t}_i$ is the unit tangent vector.

2.3 Equation of Motion

The rotating bodies in this research follow the equation of motion shown in equation (2.71)

$$J\frac{d^2\theta}{dt^2} = T_r - T_f \tag{2.71}$$

where J is the moment of inertia, θ is the rotation angle of the rotating body, T_r is the torque, and T_f is the friction torque. If we take the approximate backward difference of equation (2.71), the angular acceleration α^t of the rotating body at time t can be expressed in equation (2.72).

$$\alpha^t = \frac{T_r^t - T_f^t}{J} \tag{2.72}$$

If the rotating body is assumed to accelerate uniformly, and its rotation angle is $\Delta\theta^t$ within an infinitesimally small time frame of Δt, then body rotation angle $\Delta\theta^t$ can be expressed as follows

$$\Delta\theta^t = \omega^t \Delta t + \frac{\alpha^t \Delta t^2}{2} \tag{2.73}$$

where ω^t is the angular velocity of the rotating body at time t. At the next time interval $t + \Delta t$, the rotation angle $\theta^{t+\Delta t}$ and angular velocity $\omega^{t+\Delta t}$ of the rotating body can be respectively expressed in equations (2.74) and (2.75).

$$\theta^{t+\Delta t} = \theta^t + \Delta\theta^t \tag{2.74}$$

$$\omega^{t+\Delta t} = \omega^t + \alpha^t \Delta t \tag{2.75}$$

where θ^t is the rotation angle at time t. Therefore from equations (2.72) ~ (2.75), if the rotation angle of the rotating body is calculated at intervals of Δt, the rotation angle of the body can be obtained.

2.4 Mesh Modification

When a rotating body rotates next to a stationary body, as in the Surface Permanent Magnet (SPM) magnetic harmonic gear, it is necessary to generate a slide mesh in between the 2 bodies.

When generating a slide mesh, at least 3 mesh layers will be generated in between in the rotating and stationary bodies, as shown in Fig. 2.2. During rotation, the air region's mesh layer that is in contact with the rotating body will also rotate. However, if the rotation angle and the number of elements in the circumferential direction do not match each other as shown in Fig. 2.3(a), an error will occur then the calculation cannot continue. So that such mesh nonconformity does not occur, the nodes on the slide face will automatically move so that they are in union. A slide mesh is very useful because it is virtually unnecessary to regenerate the mesh after each analysis step, and thus shortening the analysis time.

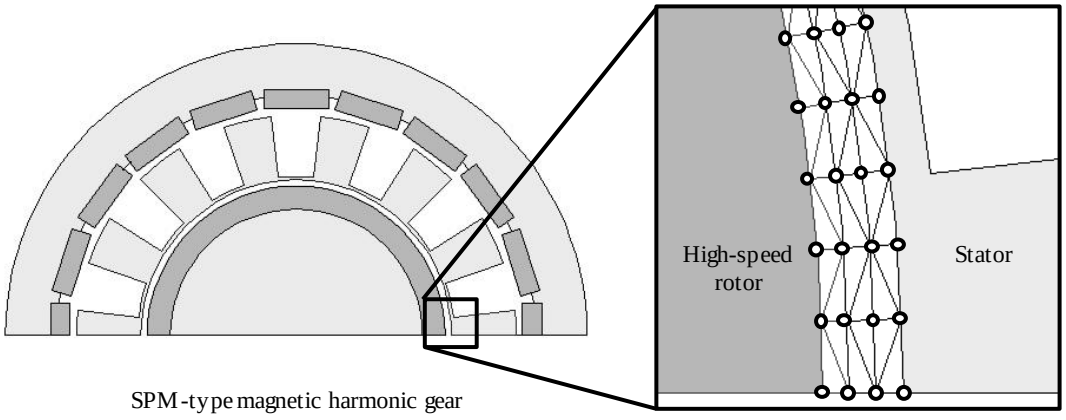

Fig. 2.2 Slide mesh.

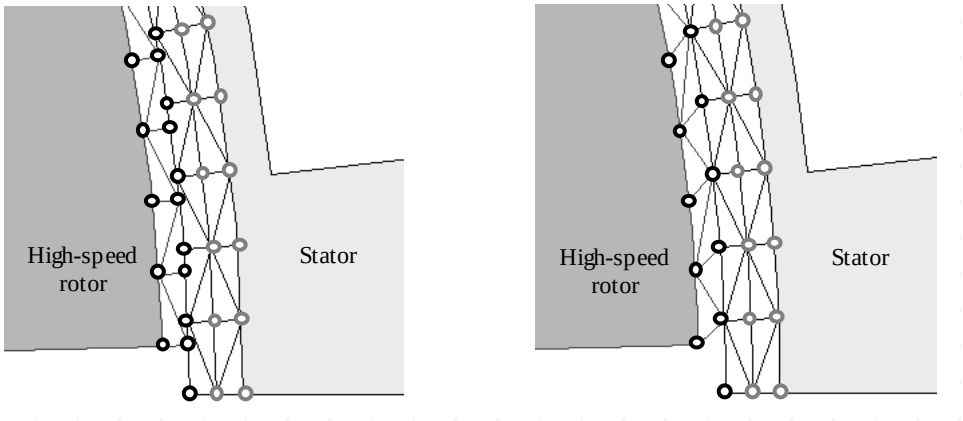

(a) (b)

Fig. 2.3 (a) unmatched mesh, (b) modified mesh.

References

1. 昇新口, “磁気波動減速機に関する基礎研究”, 大阪大学工学研究科知能・機能創成工学専攻博士後期課程論文, 2010.

Chapter 3 Magnetic Gears with Continuously Variable Gear Ratios

3.1 Introduction

Chapter 1 has already discussed the existing magnetic gears that can achieve a variable gear ratio and their respective drawbacks. The gear ratio of the magnetic gear by Daif [1] was discrete, Shah's model[2] used chain reduction gears, and the size of Wang's model[3] was too large. In this chapter, two compact models that can achieve a continuously variable gear ratio without needing any mechanical gears are proposed, their principle of operations explained and their various characteristics discussed. The first model is called the Continuously Variable Gear Ratio Magnetic Gear (CVGR-MG) and the second model is called the Continuously Variable Gear Ratio Vernier Magnetic Gear (CVGR-VMG).

3.2 Continuously Variable Gear Ratio Magnetic Gear

3.2.1 Introduction

The Continuously Variable Gear Ratio Magnetic Gear (CVGR-MG) is shown in Fig. 3.1(a). It consists of 3 parts: a high speed rotor (HSR) on the inside, a low speed rotor (LSR) in the middle, and a stator on the outside where concentrated windings have been wound and are connected to a 3 phase AC power supply. The coils are labeled in blue from 1 to 39 and Fig. 3.1(b) shows the circuit diagram.

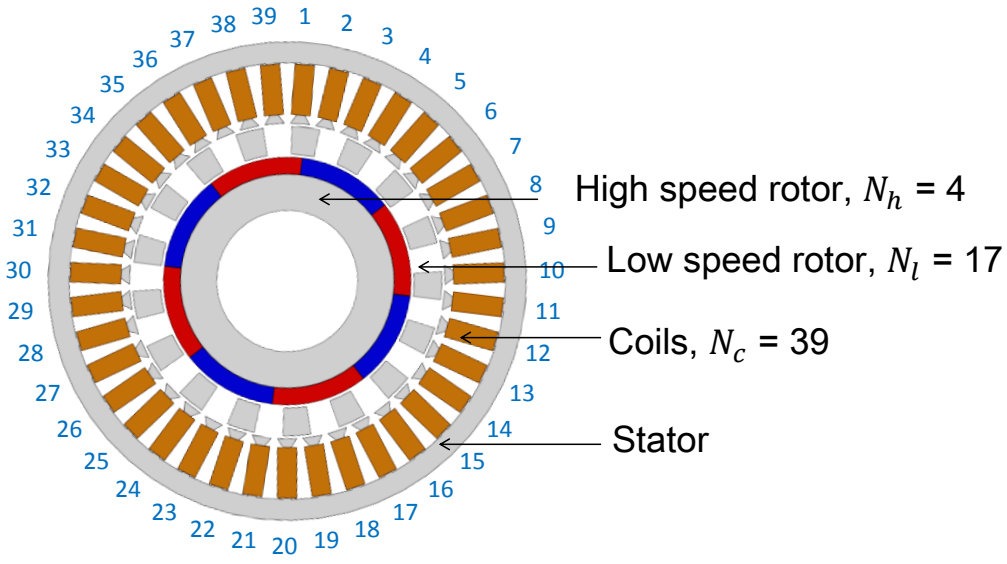

(a) 3 separate parts: HSR, LSR and Stator

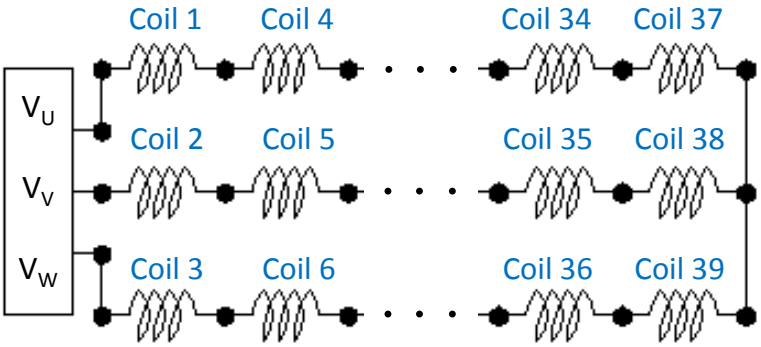

(b) Circuit diagram

Fig. 3.1 Continuously Variable Gear Ratio Magnetic Gear (CVGR-MG).

3.2.2 Principle of Operation

The principle of operation of the CVGR-MG is quite similar to that of Shah's and Wang's model. However the CVGR-MG does not require a Control Rotor, making it more compact.

First, consider the case whereby only the HSR and LSR exist as shown in Fig. 3.2, and that they are static. Like in section 1.2, the MMF of the HSR is given as

$$F(\theta) = \sum_{h=1}^{\infty} \frac{A}{(2h-1)} \sin\{(2h-1)N_h\theta\} \tag{3.1}$$

where N_h is the number of magnetic pole-pairs. Next, the permeance of the LSR is given as

$$P(\theta) = P_0 + \sum_{l=1}^{\infty} \frac{B}{(2l-1)} \sin\{(2l-1)N_l\theta\} \tag{3.2}$$

where N_l is the number of steel pieces. Multiplying them together gives us the flux distribution outside of the LSR which is

$$\phi(\theta) = \sum_{h=1}^{\infty} \frac{AP_0}{(2h-1)} \sin(D_1\theta) + \sum_{h=1}^{\infty}\sum_{l=1}^{\infty} D_0 \left[\cos(D_2 - D_1)\,\theta - \cos(D_2 + D_1)\,\theta\right]. \tag{3.3}$$

The variables D_0, D_1, and D_2 were used to simplify calculations. Their definitions are shown in equations (3.4), (3.5) and (3.6) respectively.

$$D_0 = \frac{AB}{2(2h-1)(2l-1)} \tag{3.4}$$

$$D_1 = (2h-1)N_h \tag{3.5}$$

$$D_2 = (2l-1)N_l \tag{3.6}$$

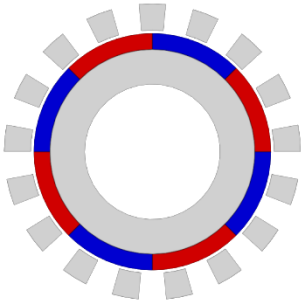

Fig. 3.2 HSR and LSR only of the CVGR-MG.

Again, we can observe the fundamental component, and 2 harmonic components in the flux distribution. In Shah's and Wang's model, either of these 2 harmonic components was coupled with a Control Rotor, which was then rotated to achieve a variable gear ratio.

However, in the CVGR-MG, either of these harmonic components is coupled directly to a rotating magnetic field produced by the coils that are connected to a 3 phase AC supply. This rotating magnetic field basically performs the same role as that of the Control Rotor. Its duty is to adjust the gear ratio of the magnetic gear. For this to happen, the magnetic field produced by the coils must have the same harmonic order

as that of the harmonic component being coupled to. Mathematically, the following condition must be satisfied

$$D_2 \mp D_1 = (2c-1)\frac{N_c}{3} \tag{3.7}$$

where N_c is the number of coils, and c is a positive integer.

Next, the full model including the coils is considered. Assume at time t, the HSR rotates $\omega_h t$ radians, the LSR rotates $\omega_l t$ radians, and the frequency of the coils is f Hz. The MMF distribution of the HSR, the permeance distribution of the LSR, the resulting flux distribution, and the flux distribution from the coils are shown respectively in the next four equations. The flux equation of the stator shown in equation (3.11) has been simplified to a sine wave equation. Strictly speaking, this is not correct since it also contains harmonics. However due to the high order of the harmonics, they do not influence the CVGR-MG in a significant way and thus can be ignored.

$$F(\theta) = \sum_{h=1}^{\infty} \frac{A}{(2h-1)} \sin\{(2h-1)N_h(\theta - \omega_h t)\}. \tag{3.8}$$

$$P(\theta) = P_0 + \sum_{l=1}^{\infty} \frac{B}{(2l-1)} \sin\{(2l-1)N_l(\theta - \omega_l t)\} \tag{3.9}$$

$$\begin{aligned}&\phi(\theta)\\ &= \sum_{h=1}^{\infty} \frac{AP_0}{(2h-1)} \sin D_1(\theta - \omega_h t) + \sum_{h=1}^{\infty}\sum_{l=1}^{\infty} D_0 \begin{bmatrix} \cos(D_2 - D_1)\left(\theta - \dfrac{D_2\omega_l t - D_1\omega_h t}{D_2 - D_1}\right) \\ -\cos(D_2 + D_1)\left(\theta - \dfrac{D_2\omega_l t + D_1\omega_h t}{D_2 + D_1}\right) \end{bmatrix}\end{aligned} \tag{3.10}$$

$$\phi_s(\theta) = \sin(2c-1)\frac{N_c}{3}\left(\theta - \frac{3ft}{(2c-1)N_c}\right) \tag{3.11}$$

Since the harmonic component from the combination of the HSR and LSR, and the flux from the stator are coupled together, their rotation angles at time t are also the same, and thus the following equation holds true

$$\frac{3ft}{(2c-1)N_c} = \frac{D_2\omega_l t \pm D_1\omega_h t}{D_2 \pm D_1}. \tag{3.12}$$

Differentiating both sides with respect to time yields equation (3.13).

$$\frac{3f}{(2c-1)N_c} = \frac{D_2\omega_l \pm D_1\omega_h}{D_2 \pm D_1} \tag{3.13}$$

Equation (3.13) links the HSR rotation speed, frequency of the 3 phase AC supply and the LSR rotation speed. Furthermore this equation is linear and clearly proves that the output speed is continuously variable.

3.2.3 Static Torque Analysis

An FEM analysis was conducted to determine the maximum transmission torque of this magnetic gear. This step is required so that in the dynamic analysis in the next section, a suitable load value can be determined. The LSR was locked, and the HSR was rotated. The U phase coils were supplied with a 1 A direct current and the V and W phase coils were supplied with a -0.5 A direct current. The model parameters are shown in Table 3.1 and the analysis results are shown in Fig. 3.3. From Fig. 3.3, the maximum transmission torque of the LSR is 35.4 Nm.

Table 3.1 Model parameters

Model Diameter	170 mm
Model Thickness	100 mm
Magnetization	1.2 T
Air Gap	1 mm
Current Amplitude	1 A
Coil Turns	600 turns/coil

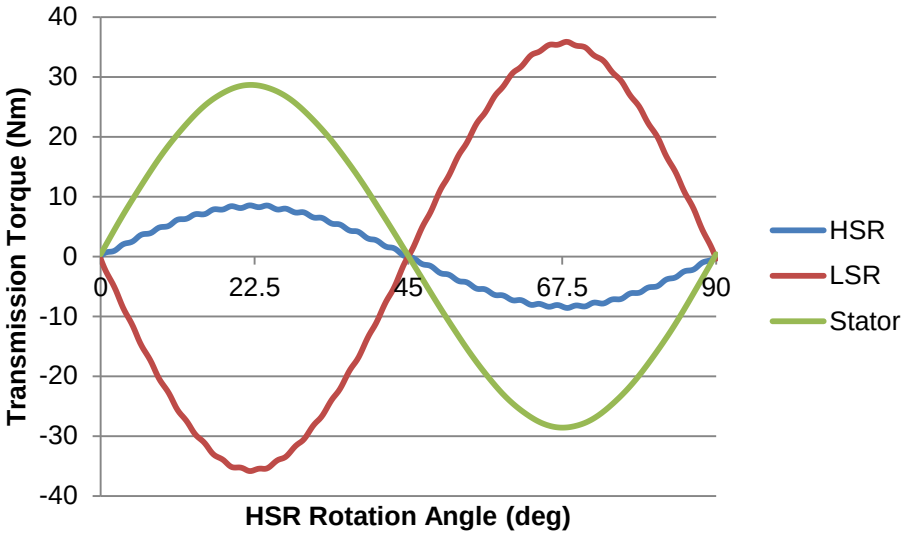

Fig. 3.3 Static torque characteristic of the CVGR-MG.

3.2.4 Continuously Variable Gear Ratio

Next, FEM analyses to confirm that the gear ratio is continuously variable were conducted. The HSR was rotated at a fixed speed (60 rpm), a load slightly lower than then maximum transmission torque was applied to the LSR (30 Nm), and the frequency of the 1A 3 phase AC current supply was varied between -30 and 30 Hz. The positive frequency value indicates that the magnetic field from the coils is rotating counter-clockwise, and a negative frequency value indicates that it is rotating clockwise.

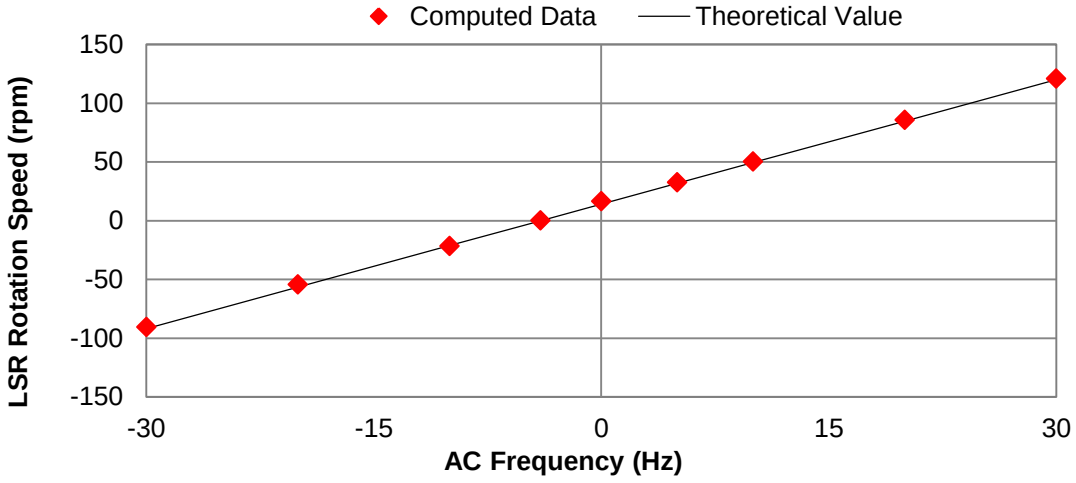

Fig. 3.4 Computed results and theory show a good agreement with each other.

Fig. 3.4 shows the LSR rotation speeds that were derived from the FEM analysis results and also compares it to the theoretical rotation speed which was derived by substituting the relevant model parameters and analysis conditions into equation (3.13). We can clearly see that the FEM analysis results agree with equation (3.13), and that a continuously variable output speed can be obtained by varying the frequency of the 3 phase AC supply.

Fig 3.5 shows some of the transmission torques of the FEM analyses. From Fig. 3.5, large torque ripples at -30 Hz can be seen, which was also seen with the other frequencies. However at f = -4 Hz the torque ripple is very small. This is due to the rotors not rotating.

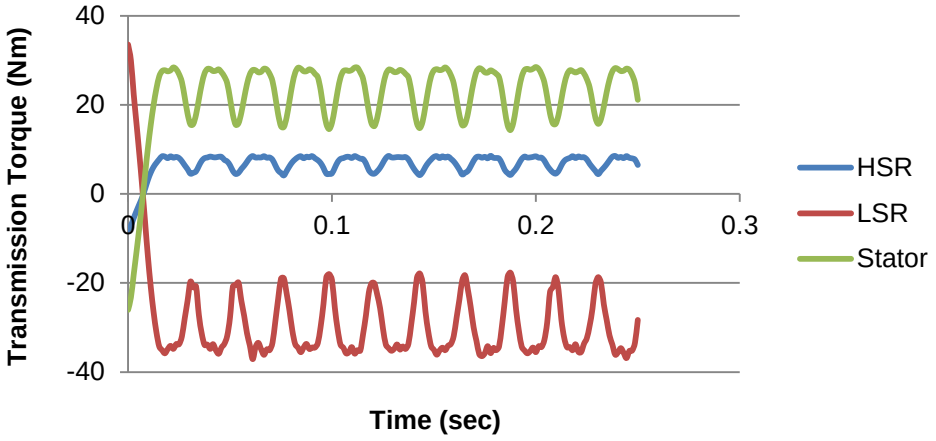

(a) f = −30 Hz

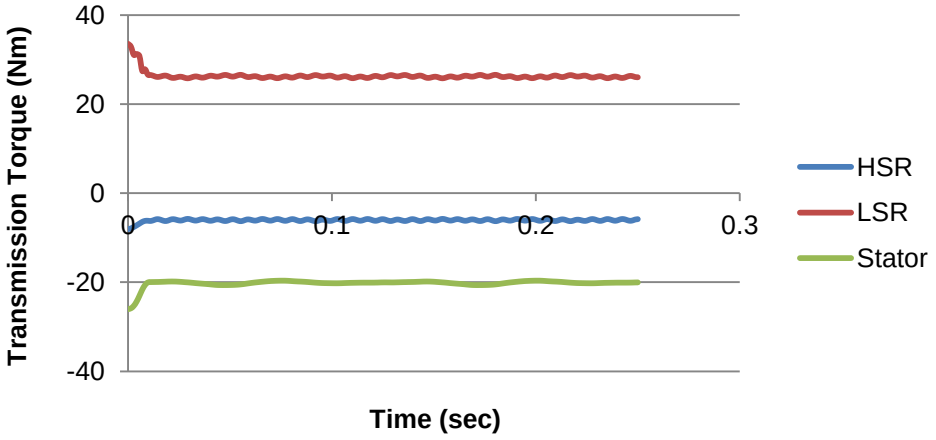

(b) f = −4 Hz

Fig. 3.5 Transmission torque waveforms

Fig. 3.6 summarizes the mean transmission torques. From Fig. 3.14, we can clearly see that the transmission torque is not affected by the frequency of the coils and the torque ratio of the LSR to the HSR is constant at 4.25. The torque ratio will always remain the same, as it is determined by the number of magnet pole pairs and steel pole pieces.

The transmission torque at −4 Hz is smaller than that at other frequency values. This is due to the fact that the LSR does not rotate at −4 Hz, and therefore the torque ripple is smaller. Even still, the torque ratio remains constant at 4.25.

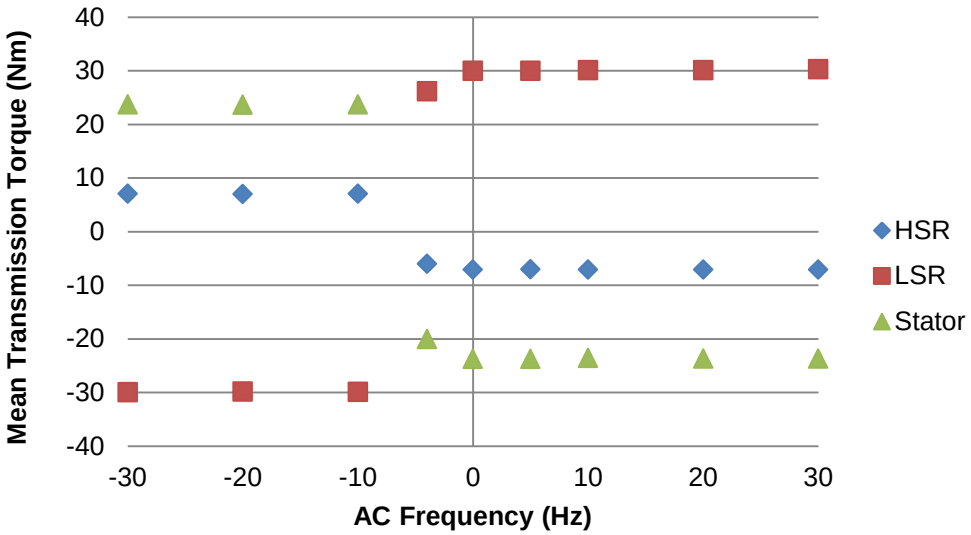

Fig. 3.6 Mean transmission torque

3.3 Continuously Variable Gear Ratio Vernier Magnetic Gear

3.3.1 Introduction

Chapter 3.3 discusses the other model that can achieve a continuously variable gear ratio: The Continuously Variable Gear Ratio Vernier Magnetic Gear (CVGR-VMG). The motivation behind this model is to reduce the number of coils that are required. The proposed model is illustrated in Fig. 3.7. It is basically a combination of the CVGR-MG and the Vernier motor, with the stator of the CVGR-MG having been replaced by that of

the Vernier motor. The Vernier motor is covered extensively in the appendix and the reading of that chapter is strongly recommended before continuing. The CVGR-VMG consists of 3 parts: a HSR, a LSR and a stator. The stator is fitted with concentrated windings. The blue numbers in Fig. 3.7(a) indicates the number of the coil that it corresponds to in the circuit diagram in Fig. 3.7(b). The coils are connected to a 3-phase AC source. Also, like the Vernier motor, there are auxiliary teeth in the stator. The parameters of the model are detailed in Table 3.2.

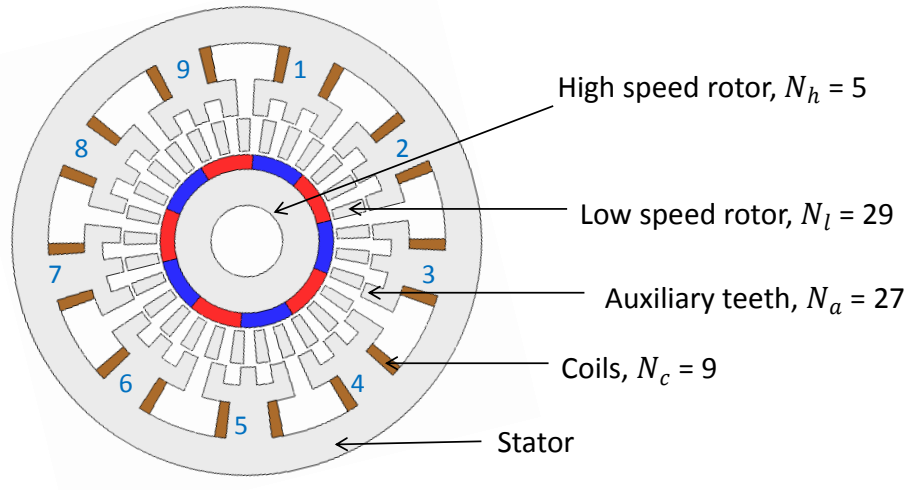

(a) CVGR-VMG

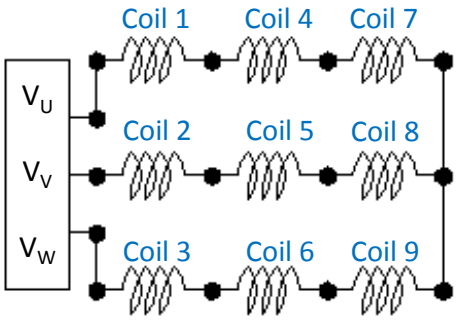

(b) Circuit diagram

Fig. 3.7 Continuously variable gear ratio Vernier magnetic gear.

Table 3.2 Model parameters.

Model Diameter	208 mm
Model Thickness	100 mm
Magnetization	1.2 T
Air Gap	1 mm
Coil Turns	600

3.3.2 Operating Principle

The CVGR-VGM works by combining the operating principles of the CVGR-MG and the Vernier motor. To explain the operating principle, the flux density distributions of the following 2 cases are considered (see Fig. 3.8):

1. The CVGR-VGM with only the rotors
2. The CVGR-VGM with only the stator (coils supplied with 1A current)

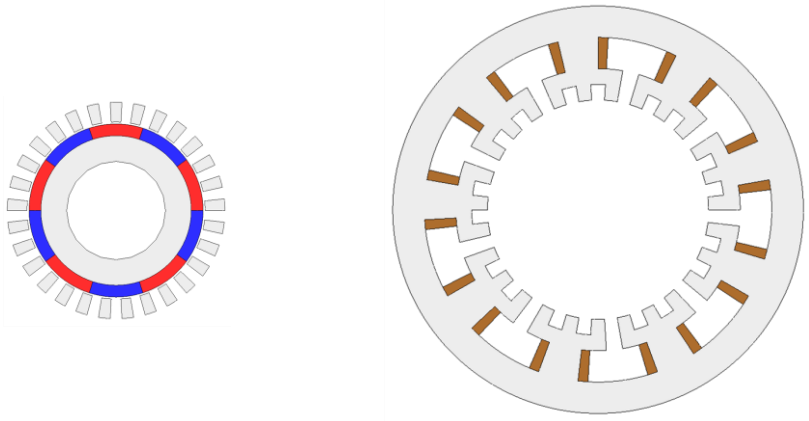

(a) Only the rotors (b) Only the stator

Fig. 3.8 Two cases considered.

First, when only the rotors exist, the flux density distribution in the air gap can be expressed mathematically using equation (3.10), which was detailed in the chapter explaining the operating principle of the CVGR-MG. For the CVGR-VGM rotors shown in Fig. 3.8(a), which has 5 PM pole-pairs and 29 steel pieces, the flux distribution and its FFT analysis results are shown in Fig. 3.9. The 4^{th} component, which is the fundamental component, and the 24^{th} and 34^{th} components, which are the harmonic components can be seen.

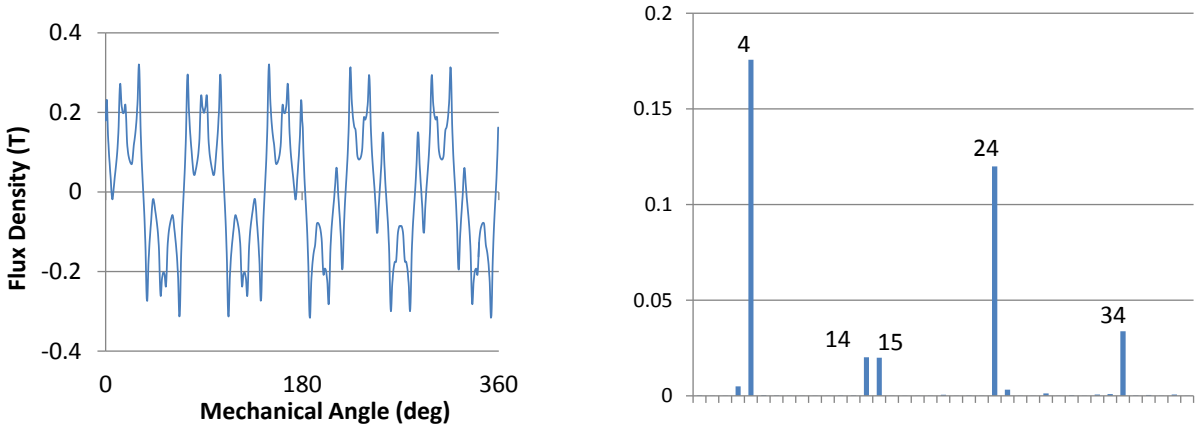

(a) Flux density distribution (b) FFT analysis

Fig. 3.9 Flux distribution of the rotors only.

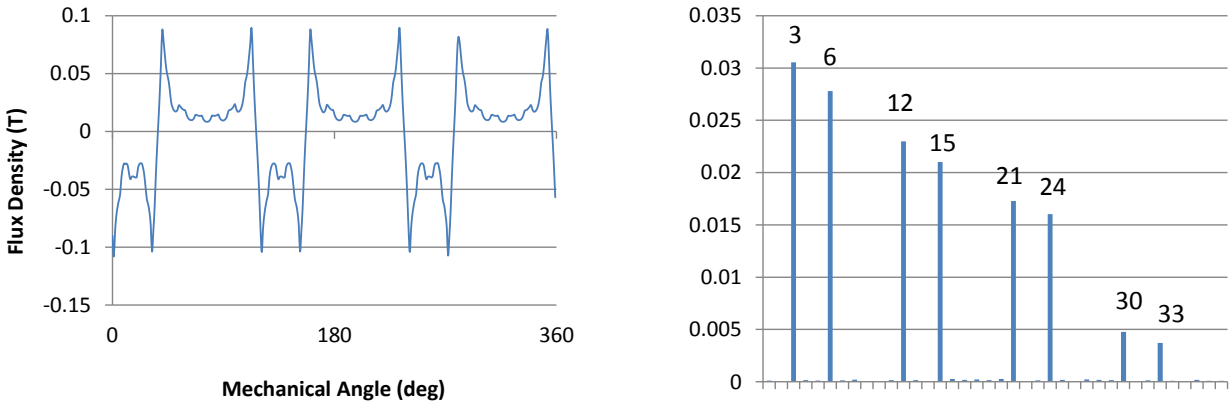

(a) Flux density distribution (b) FFT analysis

Fig. 3.10 Flux distribution of the stator only (1A current input).

Next, the flux distribution of the stator only (with 1A current input) is considered. The flux distribution of the stator can be mathematically expressed using equation (A1.6), from the chapter detailing the operating principle of the Vernier motor in the appendix. The stator of the Vernier motor detailed in equation (A1.6) did not have any auxiliary teeth, and thus in that equation, N_a corresponded to the number of stator teeth. However since the stator of CVGR-VGM does have auxiliary teeth, N_a from now on shall correspond to the number of auxiliary teeth. For the CVGR-VGM stator shown in Fig. 3.8(a), which has 9 coils and 27 auxiliary teeth, the flux distribution and its FFT analysis results are shown in Fig. 3.10. Here we can see the same flux distribution and FFT analysis results as that of the Vernier motor, with the

fundamental and harmonic flux components overlapping each other (please refer to Fig. A1.6 and Table A1.1 in the appendix).

For the CVGR-VGM operate, a flux component from the rotors and the stator, must have the same harmonic order. Mathematically speaking, the following equations must be satisfied.

$$E_i = (2h-1)N_h \pm (2l-1)N_l \quad (i = 1,2) \tag{3.14}$$

$$E_3 \pm E_i = (2h-1)N_h \pm (2l-1)N_l \quad (i = 1,2) \tag{3.15}$$

There are two constraints written above, but they are actually the same thing. Equation (3.14) says that the fundamental component of the stator must be coupled to the harmonic component of the rotors, whilst equation (3.15) says that the harmonic component of the stator must be coupled to the harmonic component of the rotors. However, as is clearly illustrated in Table A1.1 in the appendix, in the stator, the harmonic components overlap with the fundamental components. Therefore coupling the rotors' harmonic flux component with the stator's fundamental component is the same thing as coupling the rotor's harmonic flux harmonic component with the stator's harmonic component, and thus equations (3.14) and (3.15) are the same thing.

When a flux component from the rotors and the stator are coupled together, those flux components will rotate together, and the following equations will be satisfied.

$$\frac{E_2\omega_l t \pm E_1\omega_h t}{E_2 \pm E_1} = \pm\frac{2\pi f t}{E_i} \quad (i = 1,2) \tag{3.16}$$

$$\frac{E_2\omega_l t \pm E_1\omega_h t}{E_2 \pm E_1} = \pm\frac{2\pi f t}{(E_3 \pm E_i)} \quad (i = 1,2) \tag{3.17}$$

Differentiating both sides with respect to t gives the following equations

$$\frac{E_2\omega_l \pm E_1\omega_h}{E_2 \pm E_1} = \pm\frac{2\pi f}{E_i} \quad (i = 1,2) \tag{3.18}$$

$$\frac{E_2\omega_l \pm E_1\omega_h}{E_2 \pm E_1} = \pm\frac{2\pi f}{(E_3 \pm E_i)} \quad (i = 1,2) \tag{3.19}$$

Equations (3.18) and (3.19) link the rotation speeds of the HSR, LSR and the frequency of the input current.

In this thesis, the proposed model shown in Fig. 3.7 has 5 pole-pair PMs in the HSR, 29 steel pieces in the LSR, 9 coils and 27 auxiliary teeth in the stator. The model was designed so that the 24^{th} flux components from the rotors and stator would couple together. Therefore, $h = l = a = 1,\ p = 3$. Substituting these parameters into equation (3.18) gives

$$\frac{(2\cdot 1-1)\times 29\times \omega_l-(2\cdot 1-1)\times 5\times \omega_h}{(2\cdot 1-1)29-(2\cdot 1-1)5}=-\frac{2\pi f}{\frac{(3\cdot 3-2)9}{3}} \tag{3.20}$$

On the other hand, substituting the same parameters into equation (3.19) gives

$$\frac{(2\cdot 1-1)\times 29\times \omega_l-(2\cdot 1-1)\times 5\times \omega_h}{(2\cdot 1-1)29-(2\cdot 1-1)5}=-\frac{2\pi f}{(2\cdot 1-1)27-\frac{(3\cdot 3-2)9}{3}} \tag{3.21}$$

Rearranging equations (3.20) or (3.21) both gives the final equation shown here in equation (3.22). This again proves that equations (3.14) and (3.15) are the same thing. Also, it can clearly be seen that equation (3.22) is a linear equation and therefore a continuously variable gear ratio can be obtained.

$$29\omega_l-5\omega_h=-2\pi f \tag{3.22}$$

3.3.3 Static Torque Analysis

An FEM analysis was conducted to determine the maximum transmission torque of this magnetic gear. Again, this step is required so that in the dynamic analysis in the next section, a suitable load value can be determined. The LSR was locked, and the HSR was rotated. The U phase coils were supplied with a 1 A direct current and the V and W phase coils were supplied with a -0.5 A direct current. The model parameters are shown in Table 3.3 and the analysis results are shown in Fig. 3.11. From Fig. 3.11, the maximum transmission torque of the LSR is 10.6 Nm.

Table 3.3 Model parameters.

Model Diameter	208 mm
Model Thickness	100 mm
Magnetization	1.2 T
Air Gap	1 mm
Current Amplitude	1 A
Coil Turns	600 turns/coil

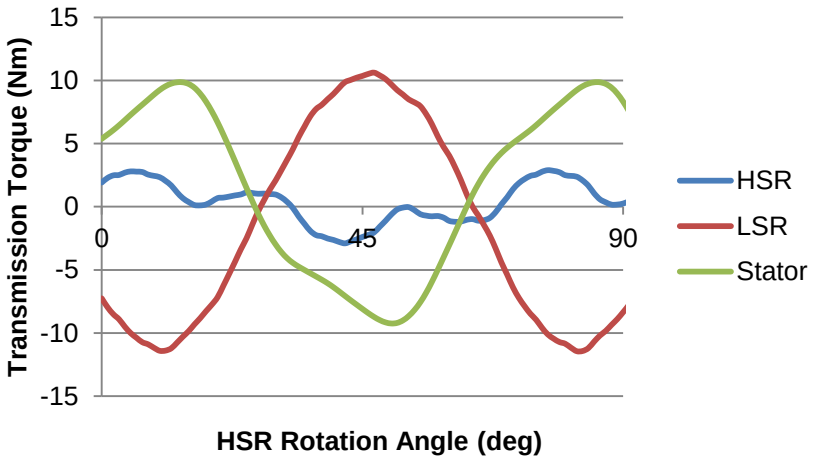

Fig. 3.11 Static torque characteristics of the CVGR-VGM.

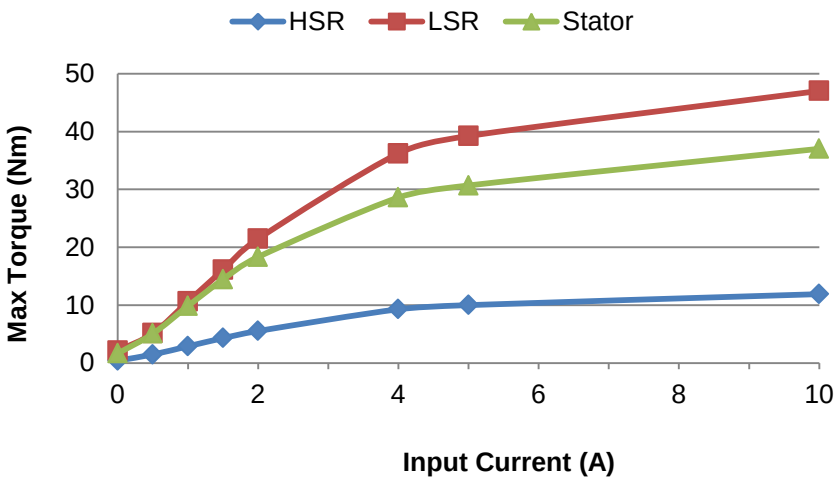

Fig. 3.12 Maximum torque of the CVGR-VGM with respect to input current.

Next, the analysis was repeated but with different input currents. The analysis results are summarized in Fig. 3.12. From Fig. 3.12, we can see that the maximum torque is proportional to the input current and the relationship is linear up until 4 Nm. After that, the increase of the maximum torque slows down and the graph seems to flatten out. This is due to magnetic saturation in the stator occurring at the higher input currents, such as can be seen in the contour graph in Fig. 3.13.

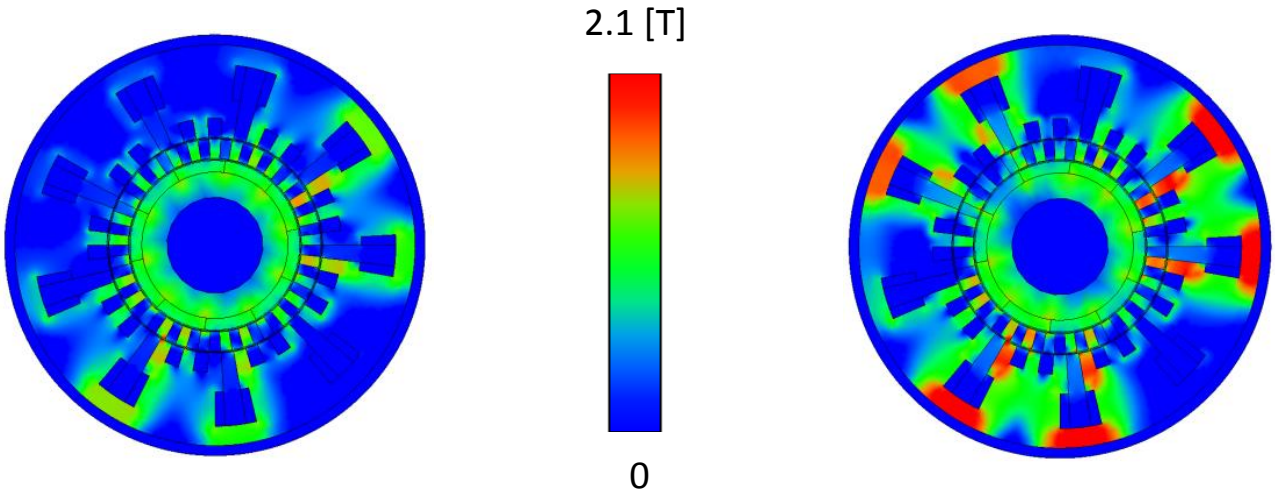

(a) 1.5 A (b) 5 A

Fig. 3.13 Flux density contour view of the CVGR-VGM.

3.3.4 Continuously Variable Gear Ratio

Next, the HSR was rotated at a fixed speed (60 rpm), a slightly lower than the maximum transmission torque was applied to the LSR (8 Nm), and the frequency of the 1 A, 3 phase AC supply was varied from -30 to 30 Hz. Fig. 3.14 shows the FEM analysis results and also compares it to the theoretical rotation speed shown in equation (3.22), and Fig. 3.15 shows some of the transmission torque waveforms from the conducted analyses. The ripples at f = 5 Hz is lower than at f = -30 Hz because at 5 Hz, the LSR is not rotating. Even though torque ripples can be clearly seen in the transmission torque graphs, this does not affect the overall operation of the CVGR-VMG. This is because from Fig. 3.14, the analysis results exactly match that of the theoretical value.

Therefore it can be concluded that even when using a real model where torque ripples and cogging torques have to also be considered, the CVMG-VGR has a continuously variable gear ratio.

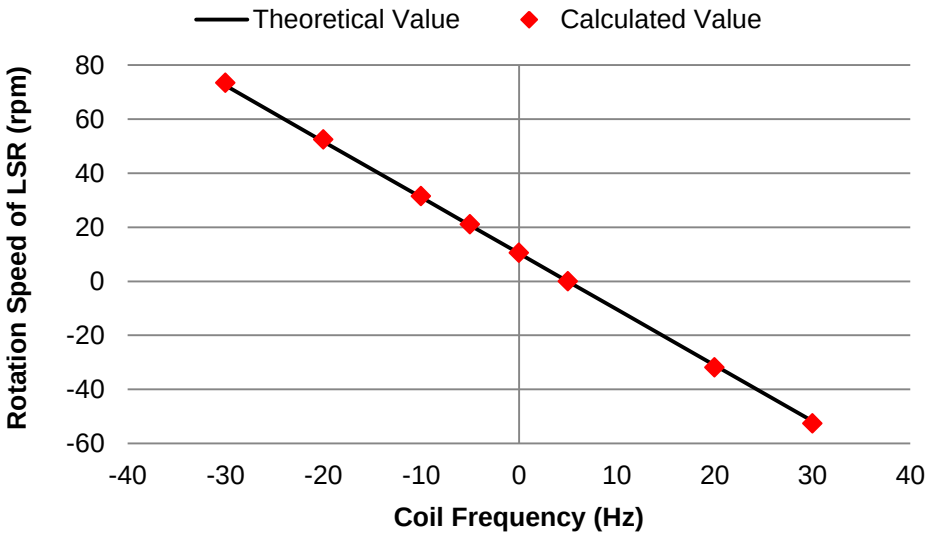

Fig. 3.14 Calculated results and theory show a good agreement with each other.

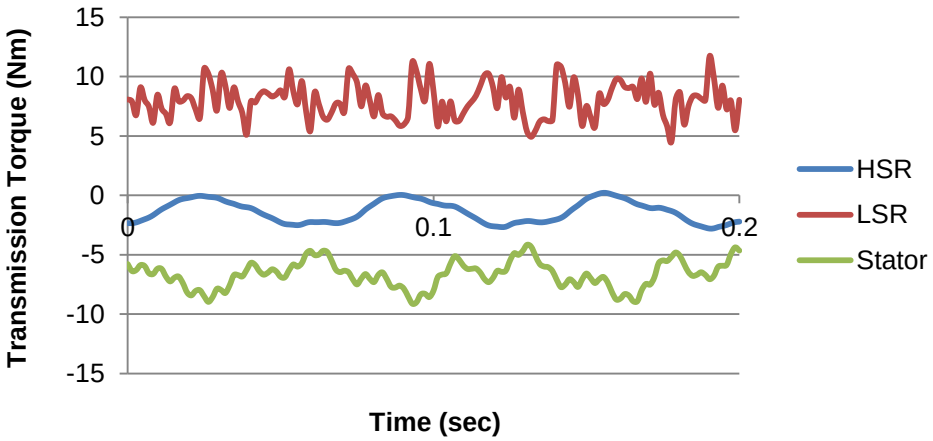

(a) $f = -30$ Hz

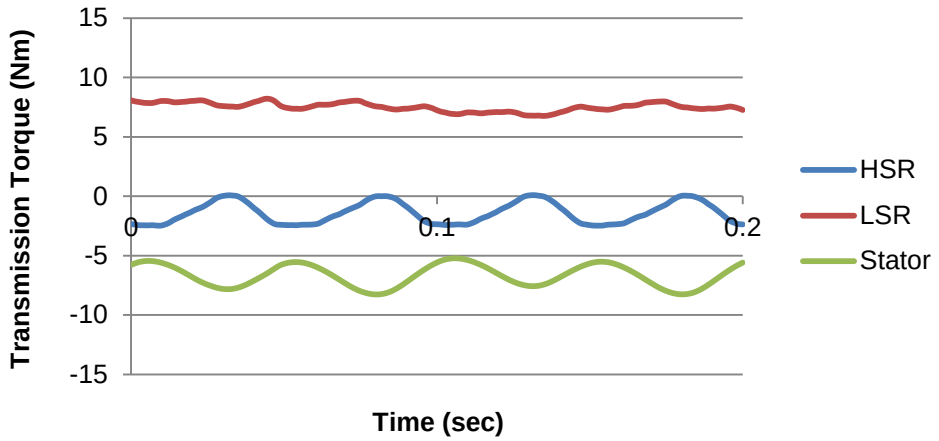

(b) f = 5 Hz

Fig. 3.15 Transmission torque waveforms

Fig 3.16 summarizes the mean transmission torques. From Fig. 3.16, we can again see that the transmission torque is not affected by the frequency of the coils and that the torque ratio of the LSR to the HSR is constant at 5.8. As was already stated before, the torque ratio will always remain the same, as it is determined by the number of magnet pole pairs and steel pole pieces.

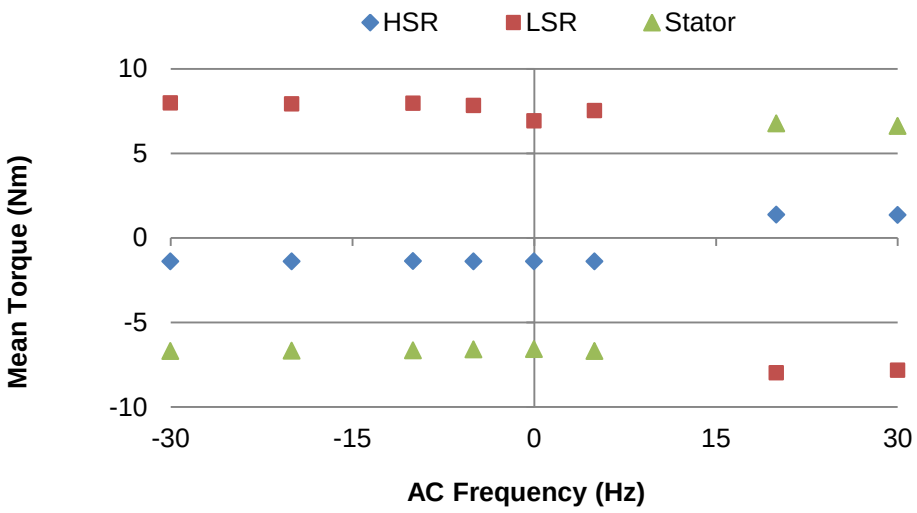

Fig. 3.16 Mean transmission torques

3.3.5 Effects of the Auxiliary Teeth

This section discusses the effects of the auxiliary teeth on the CVGR-VMG. As is stated in section 1.3 in the appendix, the auxiliary teeth is thought to increase the transmission torque and also decrease the cogging torque. To confirm this, the torque characteristics of the 3 models shown in Fig. 3.17 were analyzed. Their primary model parameters are shown in Table 3.4. A 1A DC current was input into the coils, the LSR was fixed and the HSR was rotated. The analysis results are shown in Fig. 3.18. For easy comparison, the transmission torques are grouped according to the model parts: HSR, LSR and Stator. Also, due to the large cogging torque in the transmission torque waveforms, FFT analyses were performed. The 1st component of the FFT analysis is the transmission torque component, whilst the 2nd component onwards are the cogging torque components.

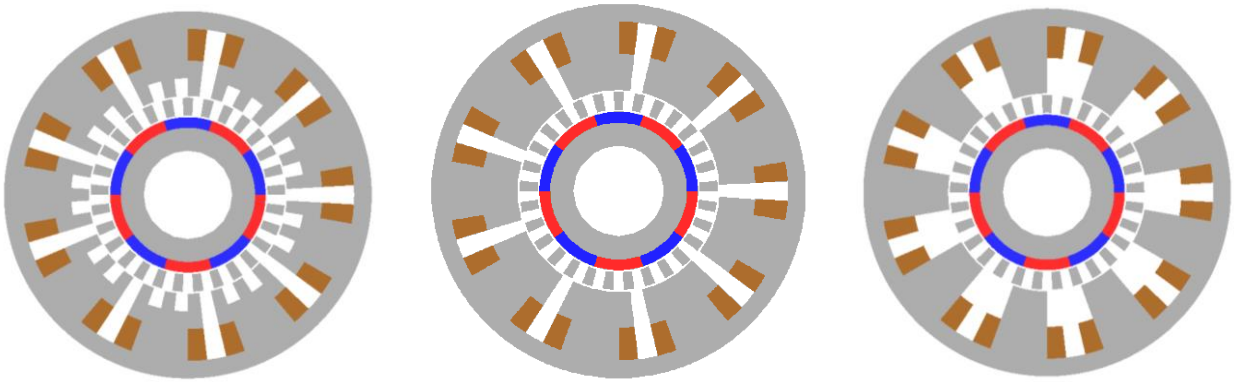

(a) Auxiliary teeth model (b) Wide teeth model (c) Even teeth model

Fig. 3.17 Analysis models.

Table 3.4 Important parameters of the magnetic gears.

Outer Diameter	204 mm
Stack Length	100 mm
HSR Magnet Pole Pairs	5
LSR Steel Pieces	29
No. of Coils	9
Coil Turns per Pole	600

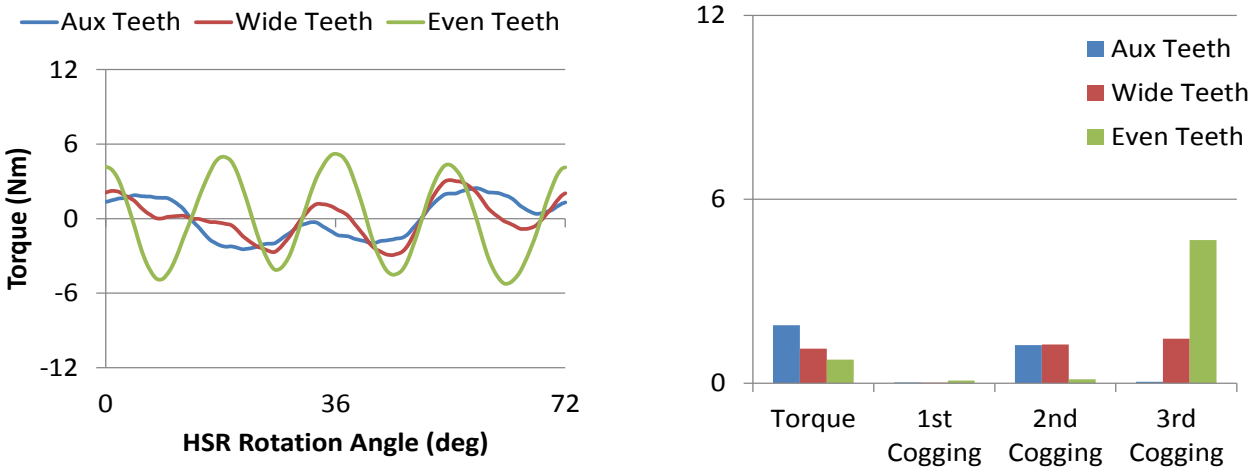

(a) HSR

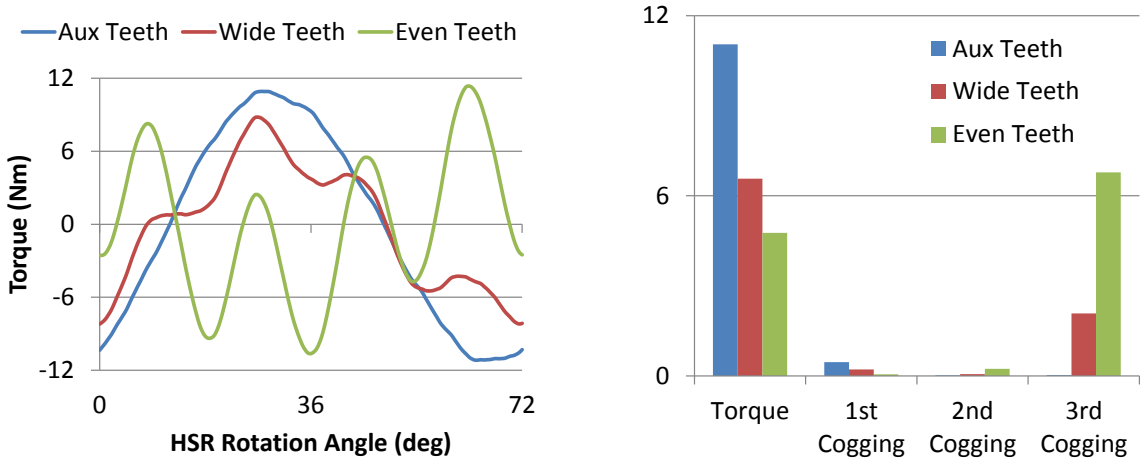

(b) LSR

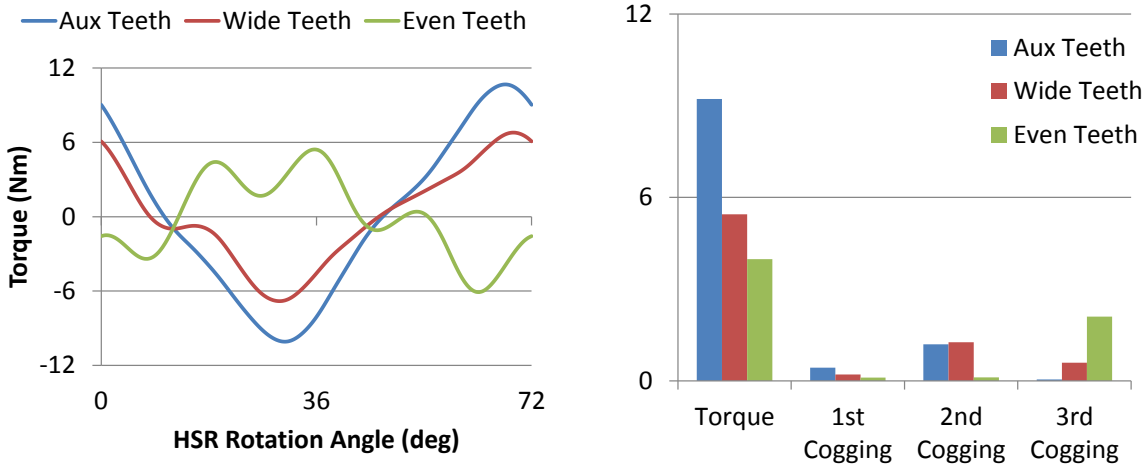

(c) Stator

Fig. 3.18 Transmission torques.

From Fig. 3.18, it can be seen that the Auxiliary Teeth model gives the largest transmission torque and also the smallest cogging torque, whilst the Even Teeth model has the smallest transmission torque and largest cogging torque. As is explained in section 1.3 of the appendix, this is due to the auxiliary teeth strengthening the transmission torque and reducing the cogging torque coefficient.

3.4 Comparison between CVGR-MG and CVGR-VMG

This chapter discusses the advantages and disadvantages of the CVGR-MG and CVGR-VMG. The author wanted to know the answer to a simple question: if all parameters are equal, which would be better? What are the advantages or disadvantages of the CVGR-MG and CVGR-VMG?

The keyword of course is “if all parameters are equal”. Currently, the model and analysis parameters of the CVGR-MG and CVGR-VMG are slightly different. For example, the diameter of the CVGR-MG is 170mm as compared to 204mm of the CVGR-VMG. Also, there are 39 coils in the CVGR-MG whilst the CVGR-VMG has only 9.

Since the most important characteristic of any magnetic gear is its torque characteristic, a static torque analysis was performed on both the CVGR-MG and CVGR-VMG. The CVGR-MG was remodeled so that the model parameters became the same as the CVGR-VMG. Also the input current of the CVGR-MG was adjusted so that its coil’s MMF would also be the same as the CVGR-VMG. The magnetic gears used in the analysis are shown in Fig. 3.19 and the model and analysis parameters are summarized in Table 3.5. The analysis results are shown in Fig. 3.20.

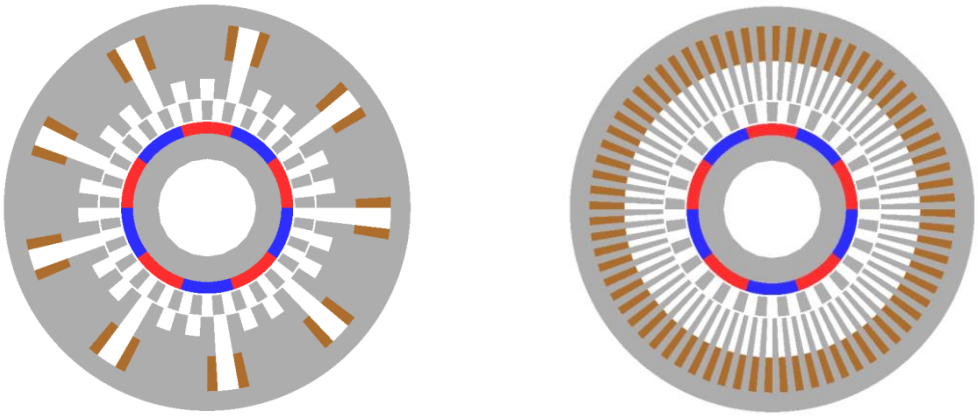

(a) CVGR-VMG (b) CVGR-MG

Fig. 3.19 Remodeled magnetic gears.

Table 3.5 Main model and analysis parameters

	CVGR-VMG	CVGR-MG
Outer Diameter	204 mm	204 mm
Stack Length	100 mm	100 mm
HSR Magnet Pole Pairs	5	5
LSR Steel Pieces	29	29
No. of Coils	9	72
Auxiliary Teeth	3 per coil	—
Current Amplitude	1 A	0.125 A
Coil Turns per Pole	600	600

From Fig. 3.20 it is very clear that the CVGR-VMG has a higher (roughly 50% more) maximum transmission torque than the CVGR-MG. This is due to the effect of the auxiliary teeth that is detailed in section 1.3 of the appendix.

However, it is also clear that the waveforms of the CVGR-VMG are quite distorted, especially the HSR. It is thought that the main reason for the distortion is due to the interaction between the 5 PMs in the HSR and the fundamental component of the coils (3 pole-pair).

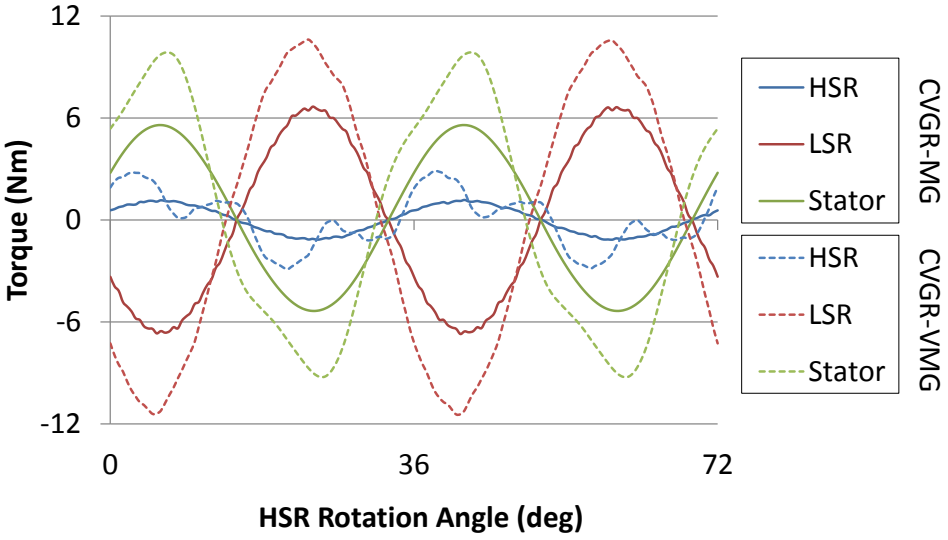

Fig. 3.20 Static torque comparison of the CVGR-MG and the CVGR-VMG.

To confirm the source of the distortion, a torque ripple and cogging torque analysis was conducted. The HSR and LSR were rotated 435 and 75 degrees respectively, and the coils were applied with a 1A DC current. The analysis results are shown in Fig. 3.21. On the right of Fig. 3.21 are the amplitudes of HSR torque ripples, which were obtained through FFT analysis of the HSR waveform.

The 18th, 36th and 72nd components respectively exist due to the interaction between the 3rd, 6th and 12th flux components of the coils and the 5 PM pole-pairs in the HSR (please refer to Figs. 3.9 and 3.10). The 18th torque ripple component is especially large since the 3rd coil flux component is very large.

The 54th torque ripple component is due to the interaction between the 14th harmonic of the rotors and the 5 pole-pair PMs of the HSR. The 290th cogging torque component is due to the interaction between the 5 pole-pair PMs in the HSR and 29 steel pieces in the LSR.

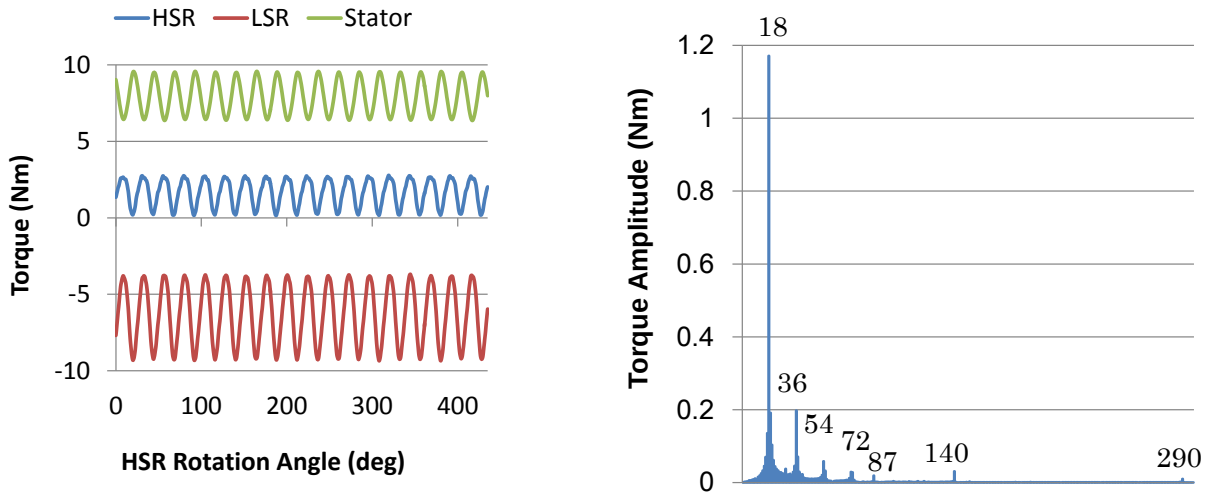

(a) Torque waveforms (b) FFT results of the HSR

Fig. 3.21 Torque ripple and cogging torque analysis results.

In conclusion, although the CVGR-VMG has a higher maximum transmission torque, its waveforms are slightly distorted meaning its operation would not be smooth. However, trying to reduce torque ripple and cogging torque is not a new research topic. This topic in conventional motors has widely been researched[5]-[12]. Common methods include:

1. Skewing the PMs or the LSR
2. Controlling the input current
3. Using uneven stator teeth width
4. Adding tiny protrusions to the face of the stator teeth facing the air gap

3.5 Summary

This chapter proposed two magnetic gears: the CVGR-MG and the CVGR-VMG. The CVGR-VMG is a combination of the CVGR-MG and the Vernier motor. Both their rotation and torque characteristics were determined and from FEM analysis, it was shown that the gear ratios of both models were continuously variable and the ratio between the LSR torque and HSR torque was constant, irrespective of the frequency of the coil currents.

Also, it was determined that when the input MMF was the same for both models, the CMVGR-VMG had a higher output torque, and when both models had the same gear ratio, the CVGR-VMG has smaller torque ripples and cogging torque.

References

1. Mustafa Husain, Katsuhiro Hirata, Noboru Niguchi, “Novel Proposals for the Realization of Variable-Transmission Magnetic Gear”, IEEJ Transactions on Industry Applications, Vol. 131, No. 11, pp. 1263-1268, 2011.
2. L. Shah, A. Cruden, B.W. Williams, “A Variable Speed Magnetic Gear Box Using Contra-Rotating Input Shafts”, IEEE Trans. Magn., Vol. 47, No. 2, pp. 431-438, 2011.
3. Jiabin Wang, K. Atallah, S.D. Carvley, “A Magnetic Continuously Variable Transmission Device”, IEEE Trans. Magn., Vol. 47, No. 10, pp. 2815-2818, 2011.
4. C.H. Lee, “Vernier motor and its design”, IEEE Trans. Power App. Syst., Vol. 82, No. 66, pp. 343-349, 1963.
5. Sang-Moon Hwang, Jae-Boo Eom, Yoong-Ho Jung, Deug-Woo Lee, “Various design techniques to reduce cogging torque by controlling energy variation in permanent magnet motors”, IEEE Trans. Magn., Vol. 37, No. 4, pp. 2806 – 2809, 2001.
6. G.H. Jang, C.J. Lee, “Design and control of the phase current of a brushless DC motor to eliminate cogging torque”, Journal of Applied Physics, Vol. 99, No. 8, pp. 08R305 - 08R305-3, 2006.
7. Z.Q. Zhu, Y. Liu, D. Howe, “Minimizing the Influence of Cogging Torque on Vibration of PM Brushless Machines by Direct Torque Control”, IEEE Trans. Magn., Vol. 42, No. 10, pp. 3512 – 3514, 2006.
8. R. Islam, I. Husain, A. Fardoun, K. McLaughlin, “Permanent-Magnet Synchronous Motor Magnet Designs With Skewing for Torque Ripple and Cogging Torque Reduction”, IEEE Trans. Ind. App., Vol. 45, No. 1, pp. 152 – 160, 2009.
9. Yongchang Zhang, Jianguo Zhu, “A Novel Duty Cycle Control Strategy to Reduce Both Torque and Flux Ripples for DTC of Permanent Magnet Synchronous Motor

Drives With Switching Frequency Reduction", IEEE Trans. Power Elect., Vol. 26, No. 10, pp. 3055 – 3067, 2011.

10. E.R. Braga Filho, T.S. Araujo, "Reducing cogging torque in interior permanent magnet machines without skewing", IEEE Trans. Magn., Vol. 34 , No. 5, pp. 3652 – 3655, 1998.
11. Ki-Chan Kim, "A Novel Method for Minimization of Cogging Torque and Torque Ripple for Interior Permanent Magnet Synchronous Motor", IEEE. Trans. Magn., Vol. 50, No. 2, 2014.
12. Weizhong Fei, P.C.K. Luk, Jianxin Shen, "Torque Analysis of Permanent-Magnet Flux Switching Machines With Rotor Step Skewing", IEEE Trans. Magn., Vol. 48, No. 10, pp. 2664 – 2673, 2012.

Chapter 4 Power and Efficiency

In this section, the power equation and efficiency of the CVGR-MG and CVGR-VMG will be discussed. Although all analyses will use the CVGR-VMG model, it should be made clear that everything applies to the CVGR-MG as well.

4.1 Power Equation

The CVGR-VMG is a type of gear, and thus like all gears, mechanical power is input into it and at the same time mechanical power is also obtained from it. Mechanical power is a product of the rotor torque and angular velocity as shown by the next equation

$$P_{mech} = \tau \times \omega. \tag{4.1}$$

For conventional mechanical gears, if mechanical losses are ignored, the input and mechanical power will equal the output mechanical power.

$$\tau_{in}\omega_{in} = \tau_{out}\omega_{out} \tag{4.2}$$

For step-up gears, which are often used with generators, a low-speed high-torque input is converted into a high-speed low-torque output. On the other hand, for step-down gears, which are often used with vehicles, a high-speed low-torque input is converted into a low-speed high-torque output. However, as was already stated, if mechanical losses are ignored the input and output mechanical power will be the same.

However in the power equation of the CVGR-VGM (and also CVGR-MG), the input electrical power, which creates a controllable rotating magnetic field, must also be considered, as well as the copper loss, which can be considered to be a type of output that cannot be ignored. Therefore equation (4.2) cannot be used to describe the CVGR-VMG.

Fig. 4.1 illustrates the input and output power relationship of the CVGR-VGM and equation (4.3) expresses it mathematically. It should be noted that since only FEM analyses are conducted, as opposed to conducting experiments on a prototype, it is not necessary to consider mechanical, hysteresis and eddy current losses.

$$\tau_{in}\omega_{in} + 3VI\cos\theta = \tau_{out}\omega_{out} + 3I^2R \tag{4.3}$$

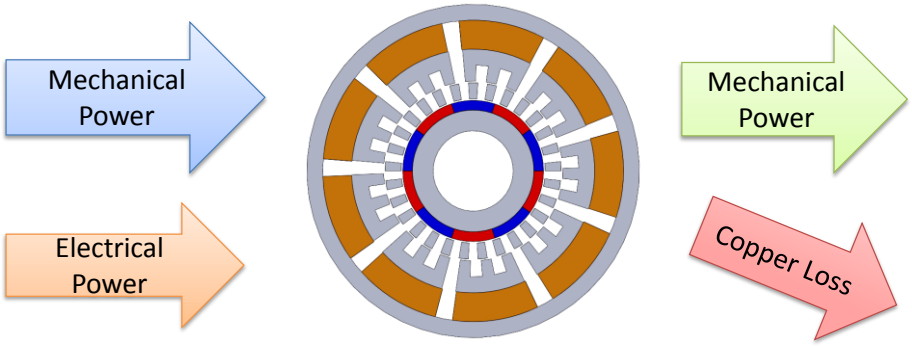

Fig. 4.1 Input / Output power diagram.

Equation (4.3) has two "3"s in front of the electrical input and copper loss terms. This is because the CVGR-VGM uses 3-phase power. V and I are the RMS values of the input voltage and current of a single phase, and R is the total resistance of that phase. θ is the phase angle of the power triangle of a single phase, as shown in Fig. 4.2.

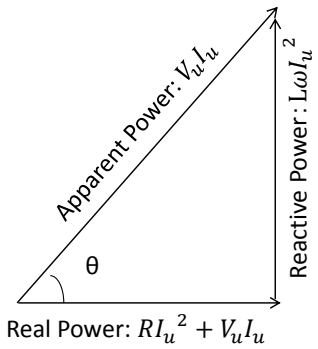

Fig. 4.2 Power triangle (U-phase).

To confirm that the proposed power equation in (4.3) is correct, FEM analysis where the input and output powers are recorded and compared at different input voltage frequencies should be conducted. The conventional way to do this would be to do a dynamic analysis where a voltage is applied to the coils, a load is applied to the output rotor and the input rotor is rotated. However doing this takes a long time due to the need for the FEM analysis software to solve the motion of equation at every time step.

Therefore a pseudo-dynamic analysis was conducted instead.

In a pseudo-dynamic analysis, no motion of equations are used, therefore shortening the analysis time. A voltage is input into the coils and the input and output rotors are rotated at precalculated rotation speeds. For a given input voltage frequency, the output rotation speed can be easily obtained from equation (3.22) if the input voltage frequency is fixed. To simulate the load on the output rotor, an initial rotational displacement angle, called the "load angle", was applied. Normally, when a load is applied to a rotor, the rotor will experience a rotational displacement that corresponds to the value of the load. The load angle, in electrical degrees, indicates how much of the maximum transmission torque is being simulated, with 90 degrees being the maximum transmission torque and 0 degrees being no transmission. The load angle in this analysis was approximately 70 electrical degrees.

It was quite difficult to obtain accurate results due to noise and analytical errors. Therefore, instead of just one, two sets of analyses were conducted and their results are compared. The model and analysis parameters are shown in Table 4.1. The analysis results are shown in Fig. 4.3.

Table 4.1 Model and analysis parameters

	Analysis A	Analysis B
Model Diameter	208 mm	
Model Thickness	100 mm	
Magnetization	1.2 T	
Air Gap	1 mm	
Coil Turns	100	80
Coil Resistance (1 coil)	2.5Ω	6.8Ω
Input Rotor (LSR) speed	20 rpm	
Output Rotor (HSR) speed	-244 ~ 296 rpm	-124 ~ 296 rpm
Voltage Amplitude	20 V	
Input Voltage Frequency	-30 ~ 15 Hz	-20 ~ 15 Hz

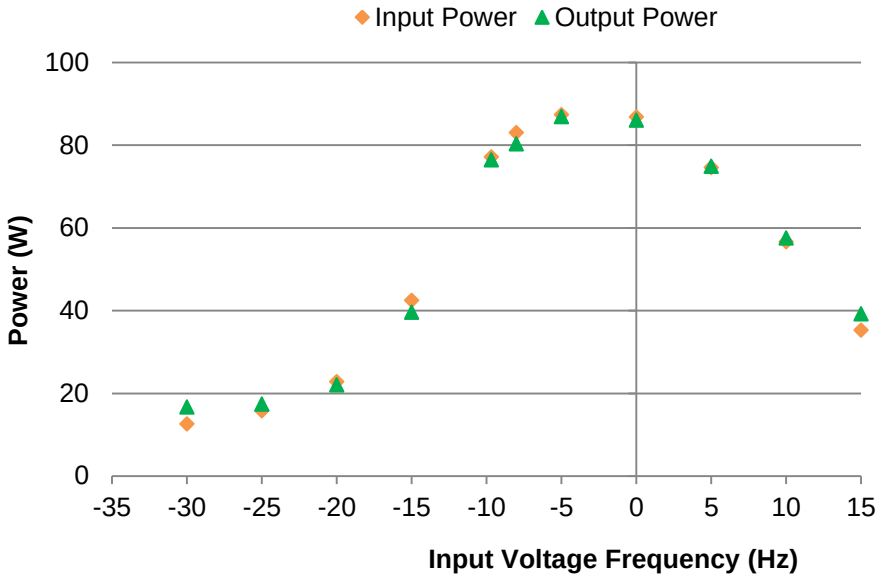

(a) Analysis A

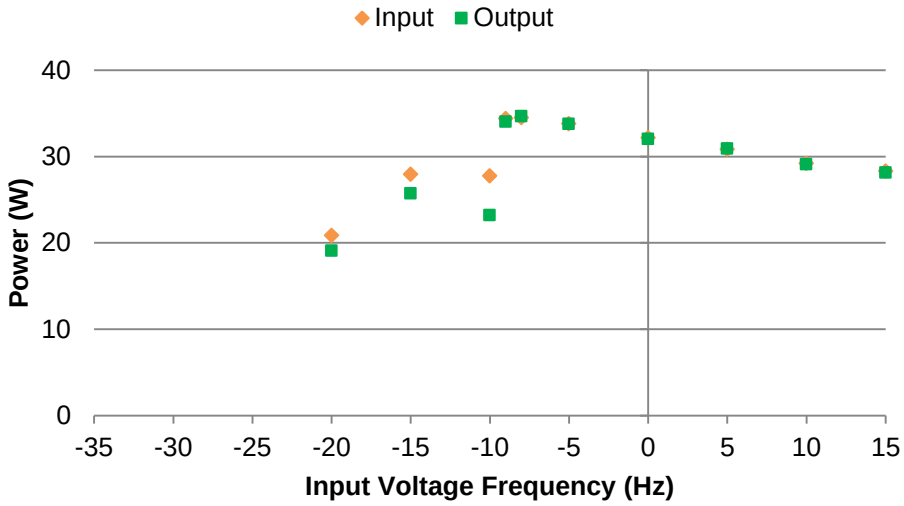

(b) Analysis B

Fig. 4.3 Input and output power comparison.

From Fig. 4.3, for Analysis A, we can see that the input and output powers more or less match each other. Some errors can be seen but this is thought to be due to analytical errors. For Analysis B, errors are much more pronounced, especially at -10 Hz. At -10 Hz, a sudden drop in both the input and output powers can be seen. This is due to the currents suddenly dropping at that frequency. This phenomenon can be seen in the total copper loss graph, in Fig. 4.4.

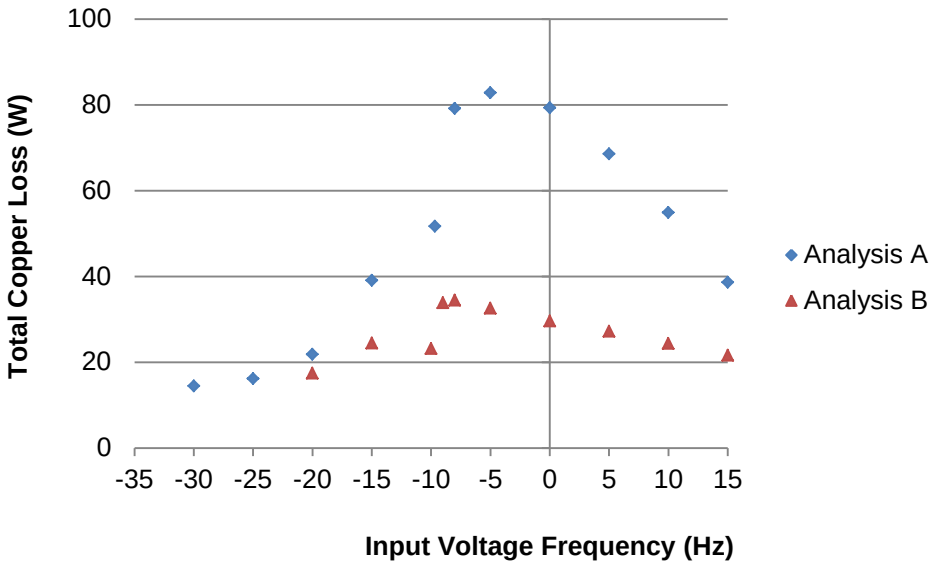

Fig. 4.4 Total copper losses of Analyses A and B.

4.2 Efficiency

Next, the efficiency of the CVGR-VMG will be discussed. The efficiency of the CVGR-VMG is defined as follows.

$$\eta = \frac{\tau_{out}\omega_{out}}{\tau_{in}\omega_{in} + 3VI\cos\theta} \times 100\% \tag{4.4}$$

From equation (4.4), it is clear that if all the other parameters do not change, and only the output speed (which is dependent on the input voltage frequency) increases, the efficiency will increase. Of course, this will not happen since as the speed of the rotors increase, the back EMF in the coils (which will be detailed later on) will also increase, decreasing the current and also the transmission torques. Therefore this problem is complex since there are more than one variable influencing the efficiency.

However, the author hypothesizes that the rotation speed will play the dominant role in determining the efficiency of the device. This is because as the output speed increases, the current and torque will decrease due to the back EMF, making the denominator of equation (4.4) small. Therefore the output speed should be the most important factor in determining the efficiency.

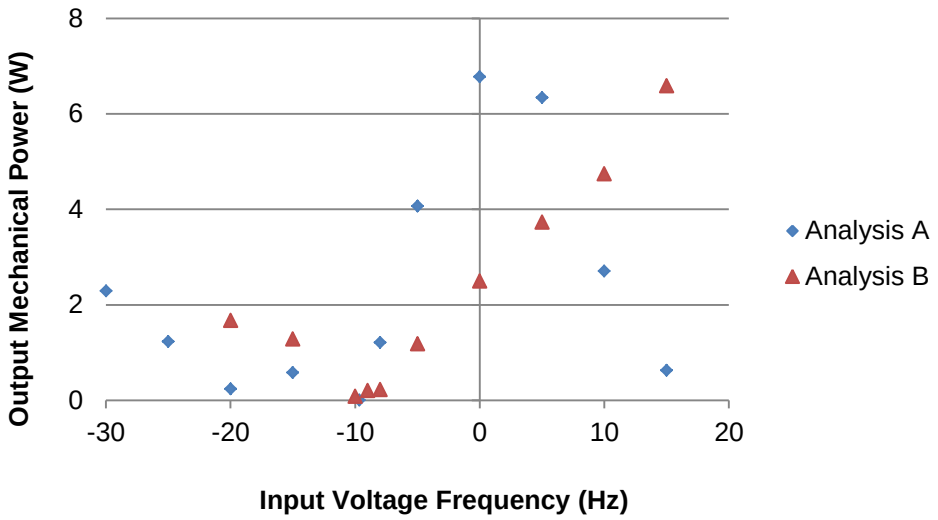

(a) Effect of voltage frequency on output mechanical power.

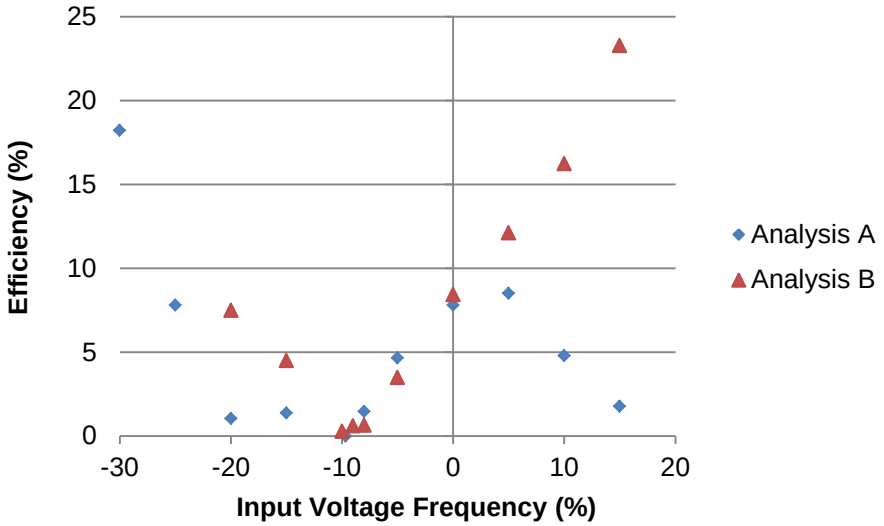

(b) Effect of voltage frequency on efficiency.

Fig. 4.5 Effect of voltage frequency on output mechanical power and efficiency.

Using the analysis data from the previous section, Fig. 4.5 shows how the output mechanical powers and efficiencies of the device changes with the input voltage frequency. At first glance, both graphs look very similar. Therefore only by this information alone, we can already gather that the output mechanical power, and more specifically, the output speed is the dominant factor in determining the efficiency of the device.

The analysis results of Analysis B clearly agrees with the author's hypothesis that increasing the input voltage frequency (towards the negative or positive side), will

increase the output speed and also the efficiency.

On the other hand, many errors, especially at -20, 10, and 15 Hz, where the values suddenly drop, can be seen in the results of Analysis A. The reason for this is thought to be due to a combination of analytical errors and the high torque ripple, which made it difficult to accurately determine the torque at low levels since at this time the torque ripples become dominant. This problem can be seen in the torque transmission graphs that are shown in Fig. 4.6.

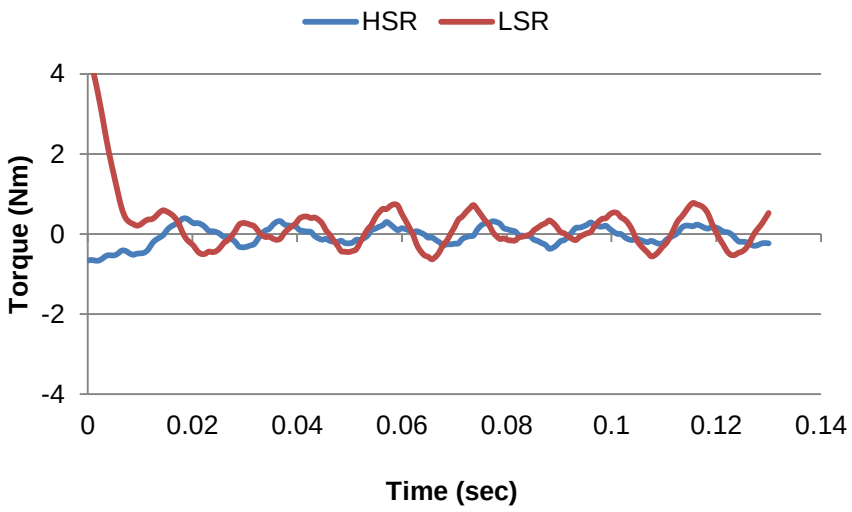

(a) f = -20 Hz

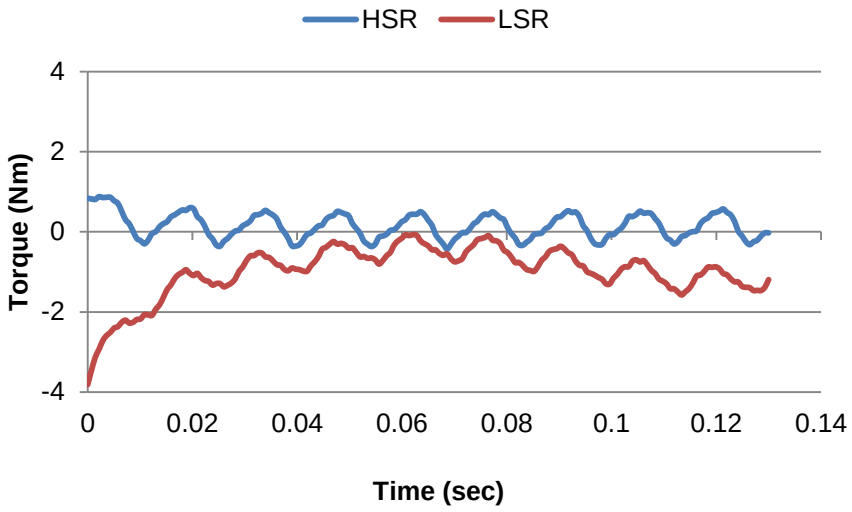

(b) f = 10 Hz

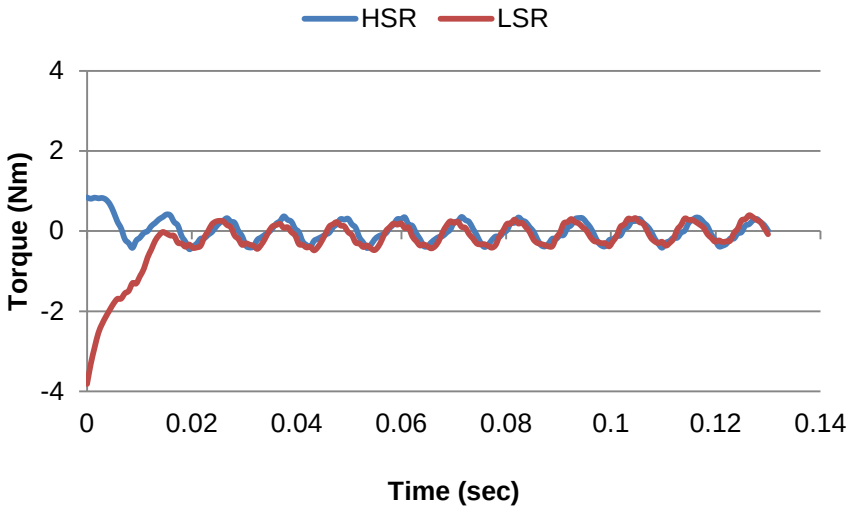

(a) f = 15 Hz

Fig. 4.6 High torque ripples are dominant at these input voltage frequencies.

Furthermore, at high frequencies, the phase angle (angle between the voltage and the current in the power triangle), becomes large, as shown in Fig. 4.7. This makes it hard to accurately determine the efficiency since at these input voltage frequencies, a small change in the phase angle causes a large change in the cosine value of the phase angle, which is what is used to determine the efficiency.

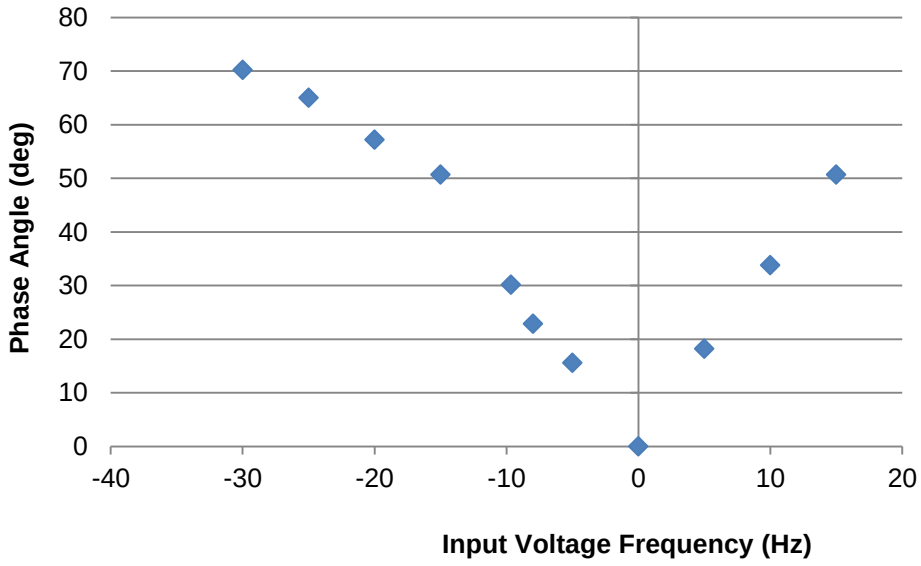

Fig. 4.7 Phase angle of the CVGR-VMG.

However, one cannot just simply keep increasing the input voltage frequency to improve the efficiency. The reason is that at high HSR rotation speeds, the back EMF can become larger than the input voltage, meaning that the CVGR-VGM is no longer operating as a magnetic gear, but as a generator. This phenomenon can be seen in Fig. 4.8, which shows the maximum electrical potential in the electrical circuit. (The input voltage amplitude was 20 V for both sets of analyses).

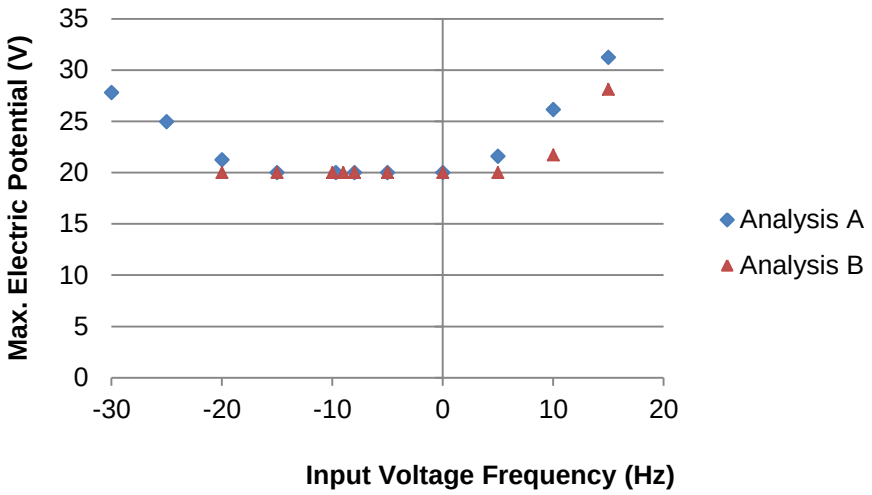

Fig. 4.8 Maximum electrical potential in the circuit (U-phase).

From 4.8, the magnetic gear operating domain for the Analysis A model (100 turns / coil) is between -15 Hz and 0 Hz. On the other hand, the magnetic gear operating domain for the Analysis B model (80 turns / coil) is between -20 Hz and 0 Hz. Analysis B was only conducted until -20 Hz, so there is a possibility that the magnetic gear operation domain is actually even larger. The reason the Analysis B model has a larger operating domain is because it has fewer coil turns; hence a smaller back EMF is generated when the HSR rotates.

4.3 Summary

In this chapter the power equation for the CVGR-MG and CVGR-VMG were derived. It was hypothesized that the efficiency of the machine is proportional to the rotation speed of the HSR and this was proven true. Therefore from this, we can gather that

these two magnetic gears would be especially suitable for high speed rotation applications.

Chapter 5 Thesis Summary

This thesis extensively studied magnetic gears with continuously variable gear ratios.

Chapter 1 started off with the history magnetic gears before moving on to describing the fundamentals of flux harmonics, how it is created and its essential role in the creation of magnetic gears. Other magnetic gears with variable gear ratios in scientific literature were briefly described, along with their disadvantages. Then, the research aim which was to develop a magnetic gear with a continuously variable gear ratio, which is a 100% non-contact device and has a relatively high torque ratio, was stated and the thesis outline was described.

Chapter 2 moved on to the topic of FEM analysis. This is because all analyses done in this thesis was conducted with FEM analysis. This chapter covered the governing equations of a magnetic field, Galerkin's method for discretization, the non-linearity of the material, how electromagnetic force is calculated and how everything comes together in the equation of motion.

In Chapter 3, two magnetic gears with continuously variable gear ratios: the CVGR-MG and CVGR-VMG were proposed. Compared to the other models in literature, the CVGR-MG is a 100% non-contact system and it only has 2 rotating parts, making it compact and easier to manufacture. Furthermore its torque ripple and cogging torque characteristics are relatively good. Therefore relatively quiet operation without requiring any complicated control is possible.

In the next section, the CVGR-VMG, which is a combination of the CVGR-MG and the Vernier motor, was proposed. The advantage of the CVGR-VMG is that it does not require many coils and is therefore easy to manufacture. Also, it is much easier to obtain a higher torque ratio when compared to the CVGR-MG. However, due to the

increased number of harmonics in the air gap, the torque ripple of the CVGR-VMG is larger than that of the CVGR-MG.

Then, In Chapter 4, the power equation of both the CVGR-MG and CVGR-VMG was proposed and verified through FEM analysis. Then the efficiency of the machines was investigated. It was discovered that the faster the HSR rotates, the higher the efficiency becomes. Therefore the CVGR-MG and CVGR-VMG would be ideal for use in high speed applications. However there was a limit to the rotation speed of the HSR. If it goes too fast, the back EMF will exceed the input voltage. This means that the machine now is no longer a magnetic gear but a generator. Therefore it is necessary that one checks the rotation speed limit of the designed machine first. The easiest way to widen the operation range would be to lower the number of coil turns so that the back-EMF would not be so high.

In the appendices, two other topics that were connected with the main research target were also investigated. The first topic, the Vernier motor, which is a type of low-speed high-torque synchronous motor, was introduced. It was shown that the Vernier motor can sometimes output a higher torque than normal synchronous motors.

Then, the possibility of the CVGR-MG and CVGR-VMG operating using induced currents were discussed. In such a configuration where the stator coil terminals are joined together, the output torque is proportional to the rotation speed of the HSR. This means that for high speed applications where a variable gear ratio is not required, the CVGR-MG and CVGR-VMG would be good candidates.

Appendix 1 Vernier Motor

1.1 Introduction

C.H. Lee[1] was the first person to propose the Vernier motor in scientific literature. His proposed model is shown in Fig. A1.1. From his paper:

"It runs at a slow speed as if it were geared down from the speed of the rotating field set up by the stator."

"As the rotor speed steps down from the speed of the rotating field, the motor torque steps up. A Vernier motor, therefore, works as an electric gearing. This kind of motor is attractive in applications which require low speed and high torque, and where mechanical gearing is undesirable. Since the Vernier motor is a synchronous machine, useful torque is developed only when it operates at synchronous speed."

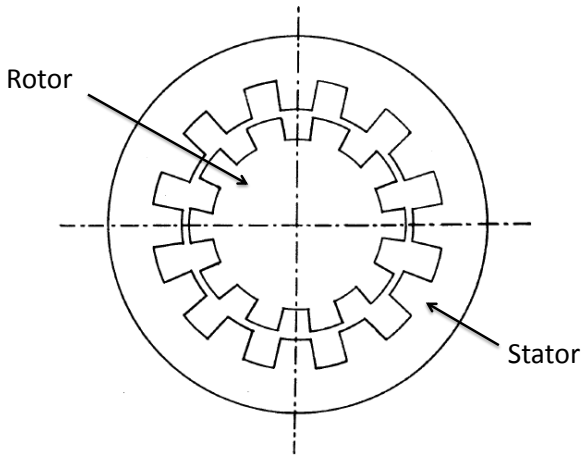

Fig. A1.1 Vernier motor by Lee (stator windings not shown in illustration).

The Vernier motor looks like a normal synchronous motor, except that the number of salient poles in the rotor is large. It operates using flux harmonics and its operating principle is very similar to the magnetic gear.

1.2 Operating Principle

The Vernier motor shown in Fig. A1.2(a) will be used for explaining the operating principle. The rotor is fitted with 6 permanent magnet pole pairs and the stator has 9 slots. The slots are fitted with concentrated windings that are connected to a 3-phase AC supply. The numbers in blue in Fig. A1.2(a) indicate the number of the coil that it corresponds to in the circuit diagram shown in Fig. A1.2(b).

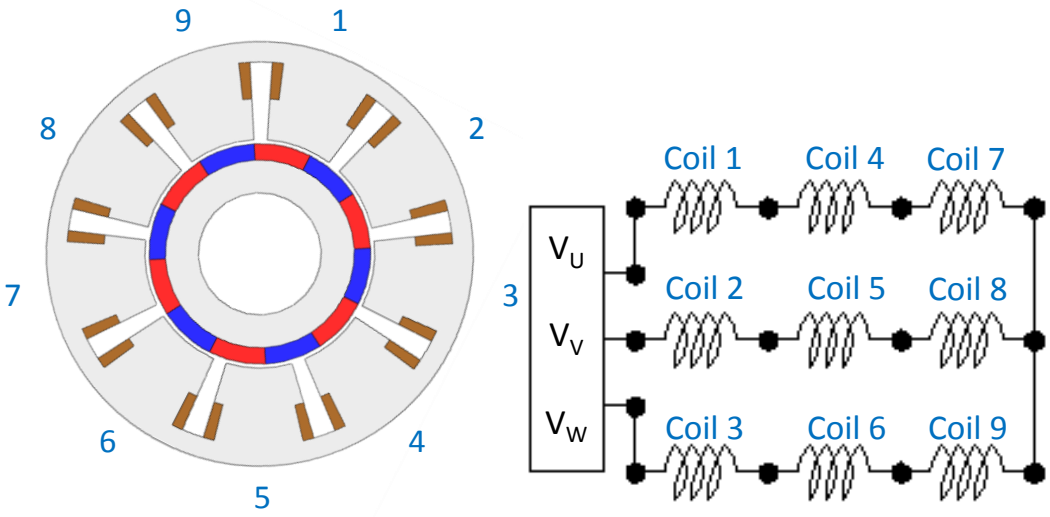

(a) Vernier motor (b) Circuit diagram

Fig. A1.2 Vernier motor.

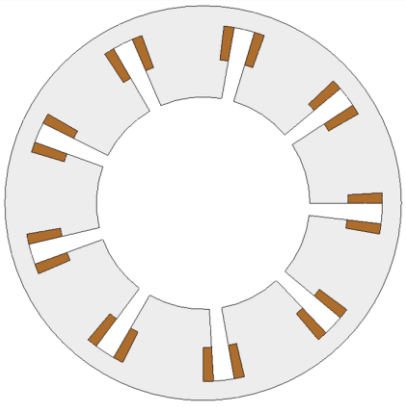

Fig. A1.3 Vernier motor with only stator present

First, the case where only the stator is present, as shown in Fig. A1.3, is considered. At time t, the MMF distribution in the air gap is

$$F(\theta)_s = \sum_{p=1}^{\infty} \frac{A}{3p-2} \sin E_1 \left(\theta + \frac{1}{N_c(3p-2)} \left(\frac{\pi}{2} - 6\pi f t \right) \right) + \sum_{q=1}^{\infty} \frac{A}{3q-1} \sin E_2 \left(\theta - \frac{1}{N_c(3q-1)} \left(\frac{\pi}{2} - 6\pi f t \right) \right). \quad \text{(A1.1)}$$

There are two fundamental components in the MMF distribution due to concentrated windings being connected to a 3 phase AC supply. E_1 and E_2 were used to simplify equation (A1.1) and their definitions are shown in equations (A1.2) and (A1.3) respectively. The MMF distribution shown in equation (A1.1) is graphed in Fig. A1.4(a) and its FFT analysis results are shown in Fig. A1.4(b). From the FFT analysis results, we can indeed see that the MMF is composed of two fundamental components that are repeated over and over again.

$$E_1 = \frac{(3p-2)N_c}{3} \quad \text{(A1.2)}$$

$$E_2 = \frac{(3q-1)N_c}{3}. \quad \text{(A1.3)}$$

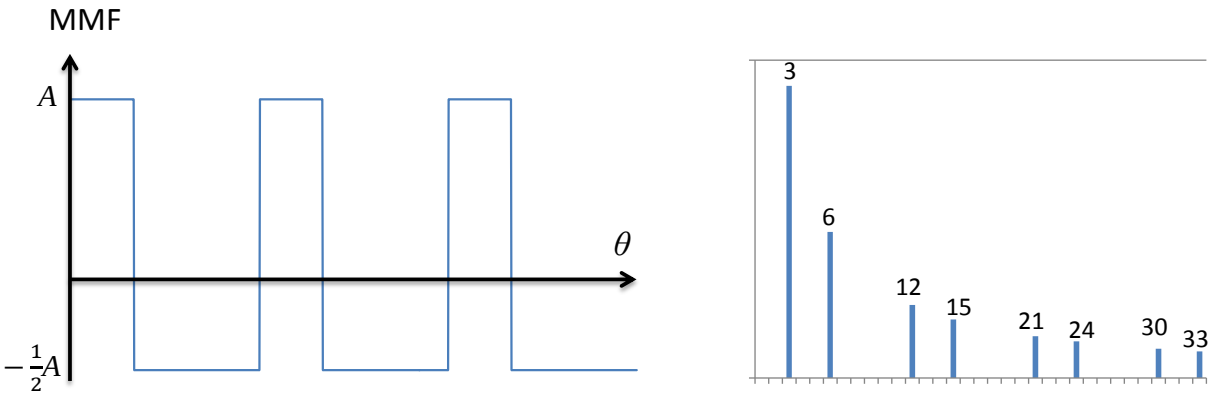

(a) MMF distribution (b) FFT analysis results

Fig. A1.4 MMF in the air gap.

Next, the permeance distribution of the teeth is

$$P(\theta)_s = P_0 + \sum_{a=1}^{\infty} \frac{B}{(2a-1)} \sin E_3 \theta \quad \text{(A1.4)}$$

where E_3 is

$$E_3 = (2a-1)N_a \tag{A1.5}$$

and N_a is the number of stator teeth. The permeance distribution shown in equation (A1.4) for the 9 slot Vernier motor shown in Fig. A1.3, is graphed in Fig. A1.5.

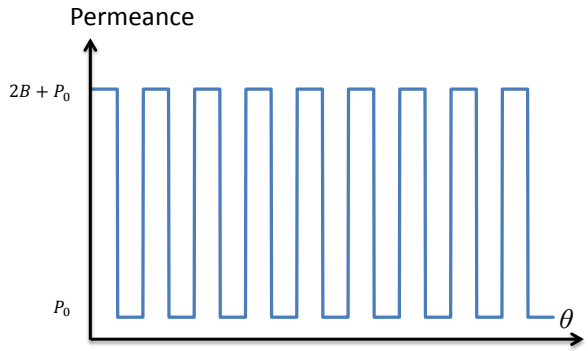

Fig. A1.5 Permeance in the air gap.

Multiplying equations (A1.1) with (A1.4) yields equation (A1.6), which is the flux distribution.

$$\phi(\theta)_s = \sum_{p=1}^{\infty} \frac{AP_0}{3p-2} \sin E_1 \left(\theta + \frac{\pi - 12\pi ft}{6E_1}\right) + \sum_{q=1}^{\infty} \frac{AP_0}{3q-1} \sin E_2 \left(\theta - \frac{\pi - 12\pi ft}{6E_2}\right)$$

$$+\frac{1}{2}\sum_{a=1}^{\infty}\sum_{p=1}^{\infty} \frac{B}{2a-1}\frac{A}{3p-2} \begin{Bmatrix} \cos(E_3 - E_1)\left(\theta - \frac{\pi - 12\pi ft}{6(E_3 - E_1)}\right) \\ -\cos(E_3 + E_1)\left(\theta + \frac{\pi - 12\pi ft}{6(E_3 + E_1)}\right) \end{Bmatrix} \tag{A1.6}$$

$$+\frac{1}{2}\sum_{a=1}^{\infty}\sum_{q=1}^{\infty} \frac{B}{2a-1}\frac{A}{3q-1} \begin{Bmatrix} \cos(E_3 - E_2)\left(\theta + \frac{\pi - 12\pi ft}{6(E_3 - E_2)}\right) \\ -\cos(E_3 + E_2)\left(\theta - \frac{\pi - 12\pi ft}{6(E_3 + E_2)}\right) \end{Bmatrix}$$

From equation (A1.6), we can see that in addition to the two fundamental components from the MMF distribution in equation (A1.1), just like with magnetic gears, new harmonic components can be seen. Equation (A1.6) is graphed in Fig. A1.6(a) and its FFT analysis results are shown in Fig. A1.6(b).

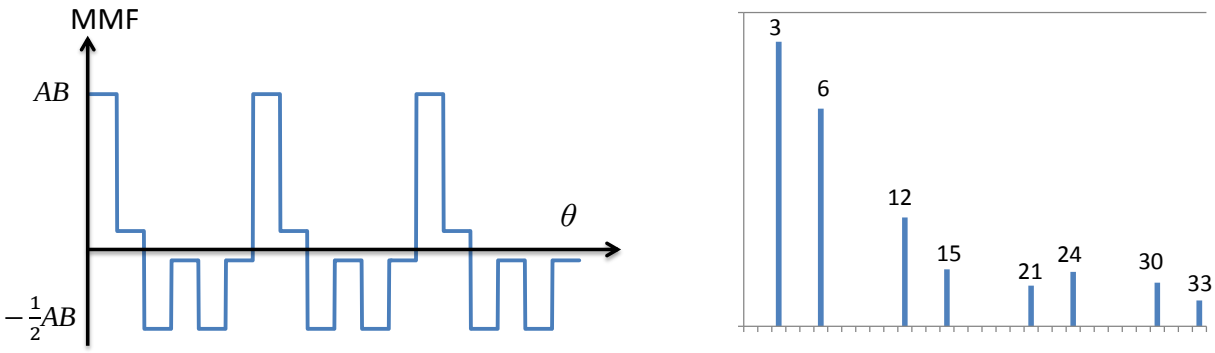

(a) Flux distribution (b) FFT analysis results

Fig. A1.6 Flux in the air gap.

However, from Fig. A1.6(b), we can only see the same components as the MMF in Fig. A1.4(b) and no new components have appeared. Apart from the slightly different sizes of each component, Figs. A1.6(b) and A1.4(b) are the same. This is due to the new harmonic components overlapping with the original fundamental components since they have the exact same order. Table A1.1 illustrates this point by showing the possible order of the fundamental and harmonic components. Table A1.1 clearly shows the harmonic components overlapping with the fundamental components.

Table A1.1 Possible spatial harmonic number of the various stator flux components

Fundamental Component 1	3, 12, 21, 30, 39, 48, ...
Fundamental Component 2	6, 1A1, 24, 33, 42, 51, ...
Harmonic Component 1	6, 15, 24, ...
Harmonic Component 2	30, 39, 48, ...
Harmonic Component 3	3, 12, 21, ...
Harmonic Component 4	33, 42, 51, ...

Then, just like magnetic gears, a flux component is chosen and a rotor with permanent magnets that have the same number of pole pairs as the harmonic order of the chosen harmonic is installed, and the rotor will rotate together with the chosen component at a much lower speed than the frequency of the 3 phase AC. As can be seen in Fig. A1.2, the 6^{th} component was chosen and thus, 6 PM pole-pairs were installed in

the rotor. However, unlike the magnetic gear, the rotor is coupled to not just the harmonic component, but also the fundamental component as well due to overlapping components. Therefore the rotor of the Vernier motor is being rotated by the 6th fundamental component and the 6th harmonic component as well.

All in all, the Vernier motor is very similar to the magnetic gear. Table A1.2 and Fig. A1.7 illustrates how parts of the Vernier motor corresponds to that of the magnetic gear.

Table. A1.2 Comparison between the Vernier motor and the magnetic gear.

Vernier Motor	Magnetic Gear
Coils connected to a 3 phase AC supply	Rotating HSR
Stator teeth	Steel pieces
Rotor	LSR

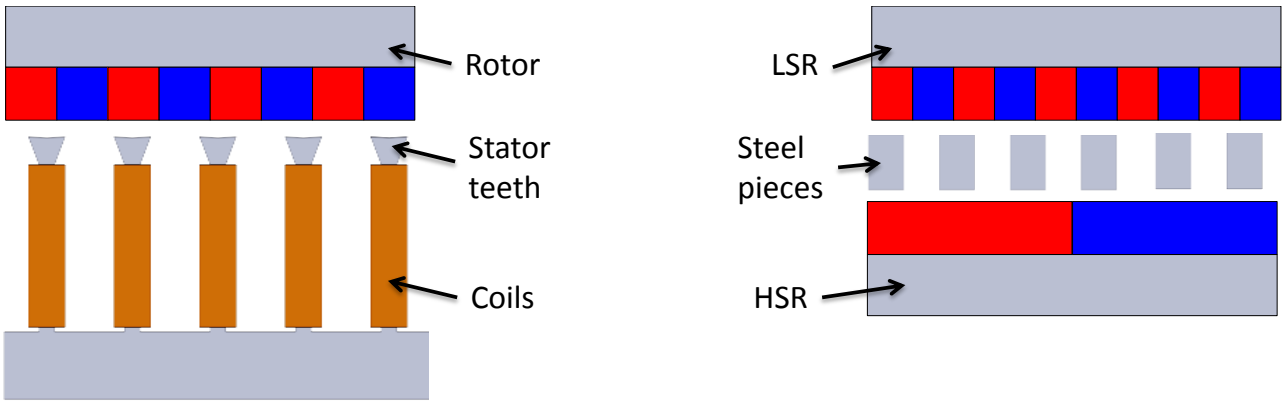

(a) Vernier motor (b) Magnetic gear

Fig. A1.7 Comparison between the Vernier motor and the magnetic gear.

1.3 Auxiliary Teeth

Apart from the large number of salient rotor poles, the first Vernier motor in scientific literature by Lee looked exactly like any other synchronous motor. It was only in later models[(2)-(8)] that the emergence of “flux modulating poles” or “auxiliary teeth” could be seen. Fig. A1.8 illustrates these auxiliary teeth using the Vernier motor by J. Li[(8)].

The auxiliary teeth have two purposes:

1. Reduce cogging torque
2. Increase output torque

Cogging torque is reduced due to the auxiliary teeth increasing the number of poles facing the air gap. As a result, the cogging torque coefficient, which is determined by inverse of the least common multiple (LCM) of the number of permanent magnet pairs and stator teeth, will decrease, also decreasing the size of the cogging torque. Expression (A1.7) expresses this mathematically

$$K_{cog} = \frac{1}{LCM(PM, Teeth)}. \tag{A1.7}$$

If the Vernier motor in Fig. A1.8 did not have any auxiliary teeth, there would be 9 stator teeth facing the air gap. The cogging torque coefficient would be

$$K_{cog} = \frac{1}{LCM(PM, Teeth)} = \frac{1}{LCM(24\,, 9)} = 0.0138.$$

On the other hand, with the auxiliary teeth, there are now 27 teeth facing the air gap. Thus the cogging torque coefficient then becomes

$$K_{cog} = \frac{1}{LCM(PM, Teeth)} = \frac{1}{LCM(24{,}27)} = 0.0046$$

which is 3 times smaller.

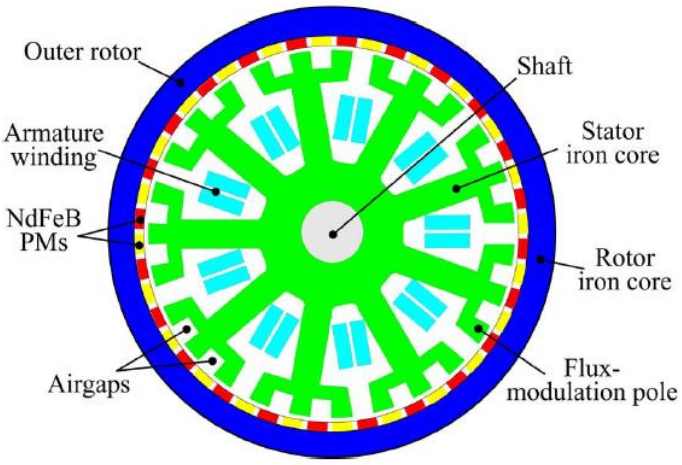

Fig. A1.8 Vernier motor with auxiliary teeth by J. Li[8].

The second purpose of these auxiliary teeth is to increase the torque by strengthening the chosen harmonic component.

A simple FEM analysis was conducted to confirm these cogging torque reduction and output torque increase properties. The two models shown in Fig. A1.9 were used. The rotor was fixed and a 1A 3 phase current was input and the torque was recorded. The analysis condition and model parameters are shown in Table A1.3, and the results are shown in Fig. A1.10.

Table A1.3 Model parameters and analysis conditions.

Diameter	90 mm
No. of PM	24 pairs
No. of coils	9
Input current	3-phase 1 A
No. of winding turns	600 / coil

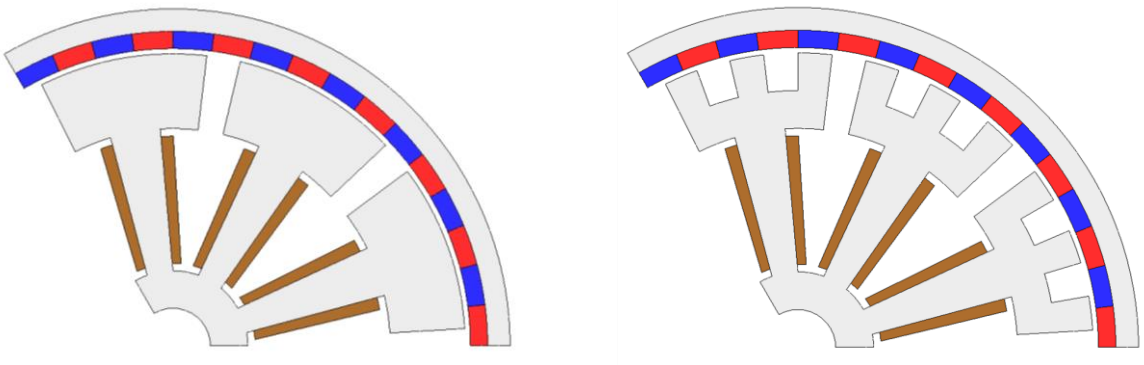

(a) Without auxiliary teeth (b) With auxiliary teeth

Fig. A1.9 Analysis of auxiliary teeth (1/3 model).

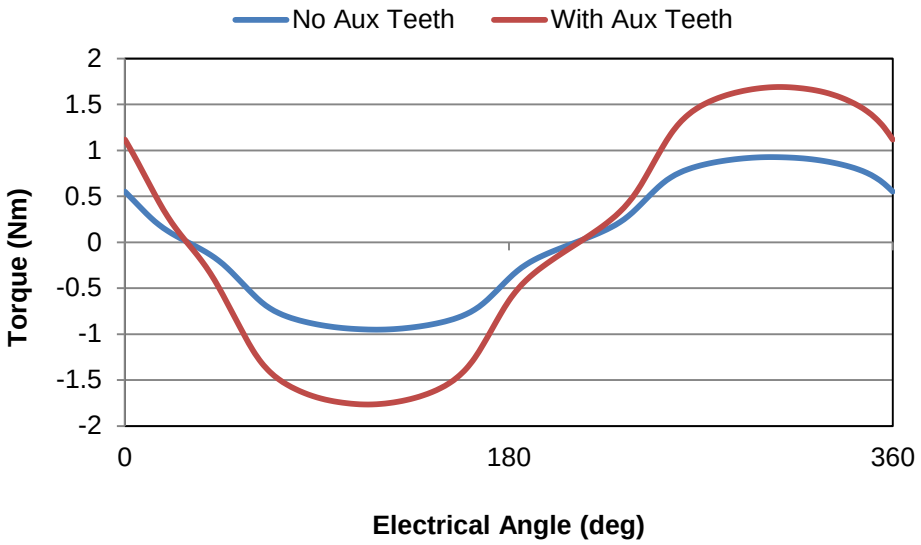

Fig. A1.10 FEM analysis results investigating effects of auxiliary teeth

From Fig. A1.10, it is clear that the torque has increased. However, cogging torque reduction could not be observed in this analysis. This is due to the cogging torque coefficient being already quite low to begin with.

1.4 Choosing the Strongest Flux Component

As mentioned in the previous section, in the Vernier motor, a flux component is chosen, and it is coupled to a rotor with the same number of PM pole-pairs. However, the author was curious as to whether one could predict, just by looking at the strength of each flux component, which component should be utilized to obtain the model with the strongest output torque.

This was done by first only looking at the stator of the Vernier motor and applying a 1A current to the coils, and then analyzing the flux distribution at 0.5mm outside the auxiliary teeth, at the place indicated by the dotted blue line in Fig. A1.11. The analysis results and the FFT analysis of the graph are both shown in Fig. A1.12.

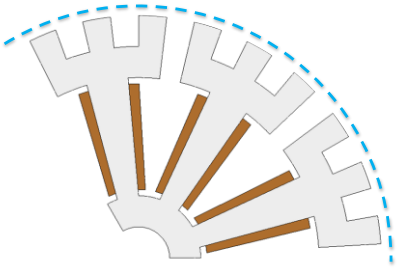

Fig. A1.11 Flux distribution analysis at 0.5mm outside the auxiliary teeth (1/3 model).

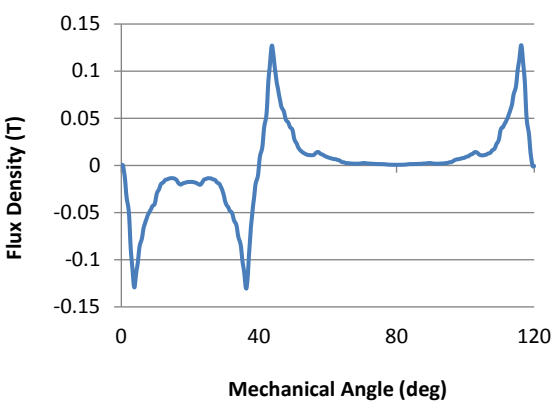

(a) Flux density distribution

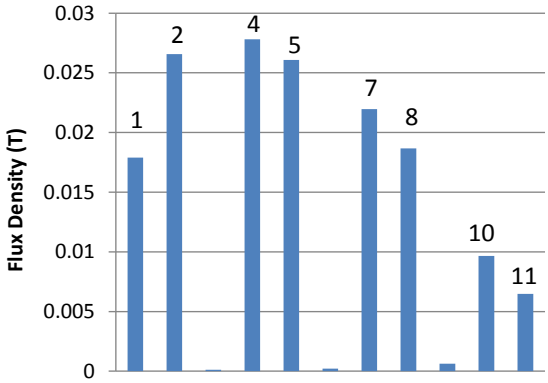

(b) FFT analysis

Fig. A1.12 Flux density distribution and FFT analysis results (1/3 model).

From Fig. A1.12(b), we can see that the 4th component is the strongest. Therefore it would make sense if a model with 4 PM pole pairs gave the strongest torque. To confirm this hypothesis, the transmission torque of models that utilize the 1st, 2nd, 4th, 5th, 7th, 8th and 10th components were created and analyzed by FEM analaysis. Fig. A1.13 shows some of the models that were analyzed. Only 1/3 of each model was analyzed due to the symmetry.

The analysis results are shown in Fig. A1.14. From Fig. A1.14, we can see that the strongest flux component did not necessarily produce the strongest output torque. Up until the 5th component model, the strength of the output torques seemed to correspond to the srength of the chosen flux component. However, for the 7th and 8th component models, the output torque increased in spite of a decrease in the strength of the flux component. Therefore from this, we can conclude that the amplitude of the chosen flux component is not the only thing that decides the output torque.

Also, it is interesting that when the 1st component is chosen, that is, when this

Vernier motor was set up as a synchronous motor, the output torque was low. Therefore we can gather that the Vernier motor can output a larger torque than synchronous motors.

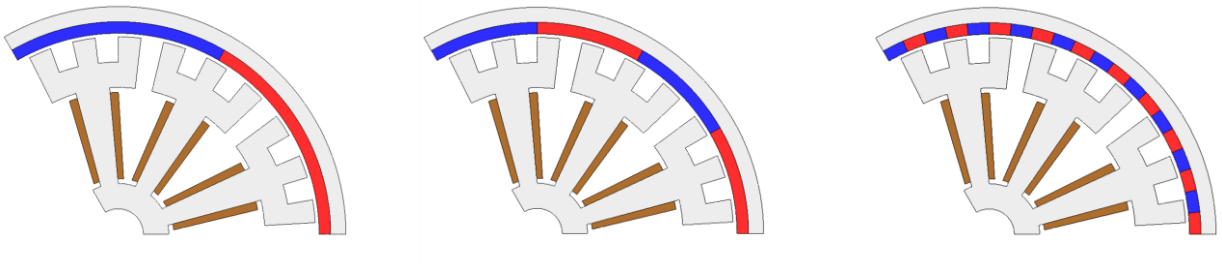

(a) 1st component (b) 2nd component (c) 10th component

Fig. A1.13 Some of the analysis models (1/3 model).

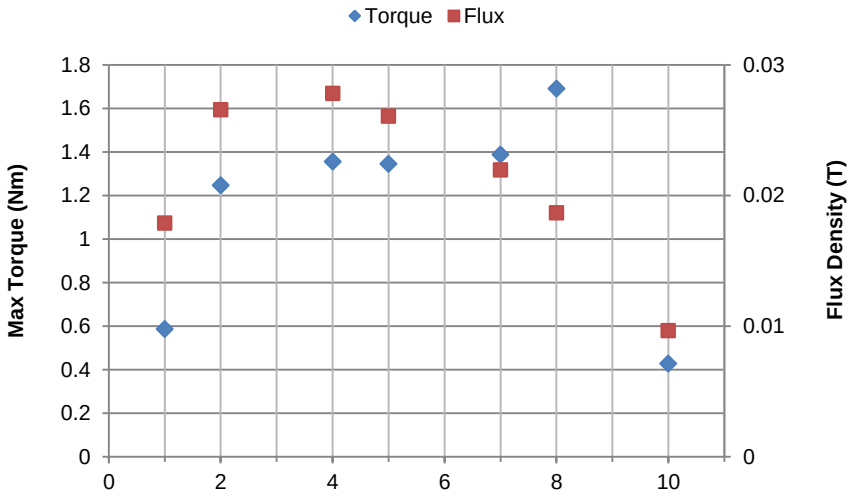

Fig. A1.14 Comparison of output torque and flux density.

References

1. C. H. Lee, "Vernier motor and its design", IEEE Trans. Power App. Syst., Vol. 82, No. 66, pp. 343-349, 1963.
2. Dae Kyu Jang and Jung Hwan Chang, "Design of a Vernier Machine With PM on Both Sides of Rotor and Stator", IEEE Trans. Magn., Vol. 50, No. 2, 2014.
3. Shuangxia Niu, S. L. Ho, and W. N. Fu, "A Novel Stator and Rotor Dual PM Vernier Motor With Space Vector Pulse Width Modulation", IEEE Trans. Magn., Vol. 50, No. 2, 2014.

4. S. L. Ho, Shuangxia Niu, and W. N. Fu , “Design and Comparison of Vernier Permanent Magnet Machines”, IEEE Trans. Magn., Vol. 47, No. 10, pp. 3280-3283, 2011.
5. Guohai Liu, Junqin Yang, Wenxiang Zhao, Jinghua Ji, Qian Chen, and Wensheng Gong, “Design and Analysis of a New Fault-Tolerant Permanent-Magnet Vernier Machine for Electric Vehicles”, IEEE Trans. Magn., Vol. 48, No. 11, pp. 4176-4179, 2012.
6. Shi-Uk Chung, Ji-Won Kim, Byung-Chul Woo, Do-Kwan Hong, Ji-Young Lee, and Dae-Hyun Koo, “A Novel Design of Modular Three-Phase Permanent Magnet Vernier Machine With Consequent Pole Rotor”, IEEE Trans. Magn., Vol. 47, No. 10, pp. 4215-4218, 2011.
7. Kenji Okada, Noboru Niguchi, and Katsuhiro Hirata, “Analysis of a Vernier Motor with Concentrated Windings”, IEEE Trans. Magn., Vol. 49, No. 5, pp. 2241-2244, 2013.
8. Jiangui Li and K.T. Chau, “A Novel HTS PM Vernier Motor for Direct-Drive Propulsion”, IEEE Trans. App. Superconduct., Vol. 21, No. 3, pp. 1175-1179, 2011.

Appendix 2 Induction Magnetic Gear

2.1 Introduction

In section 4.2, it was shown that when the HSR of the CVGR-MG or CVGR-VMG was rotated too fast, the back-EMF became larger than the input torque, meaning that the coils were generating their own current. It was from this that the author came up with the idea of using induced currents as an alternative to a 3-phase power supply to power the CVGR-MG or CVGR-VMG. The disadvantage would be that since there is no active electrical power source to control the coil currents, the gear ratio of the magnetic gear can no longer be actively controlled. On the other hand, the output torque of this magnetic gear is directly related to the rotation speed of the HSR. This means that at high speed rotations, this magnetic gear would also have a high transmission torque density. Furthermore, if compared to the magnetic gear proposed by Atallah, it only requires magnets on the HSR, meaning that only half the number of PMs is required, saving PM material.

Although both the CVGR-MG and CVGR-VMG works using the induced current configuration, in this chapter only the CVGR-MG will be used.

2.2 Operating Principle

The same CVGR-MG shown in Fig. 3.1(a) will be used in this chapter. However, the coils are no longer connected to a 3-phase AC supply. Instead, the coil terminals are connected to each other. Fig. A2.1 shows the new circuit diagram.

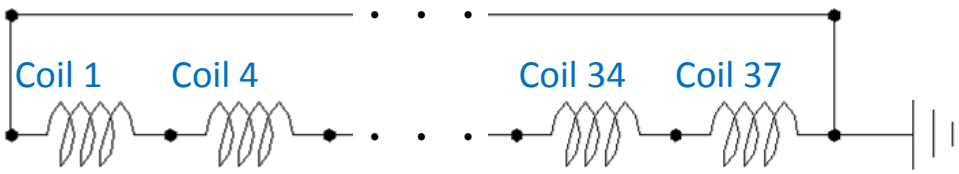

Fig. A2.1 Circuit diagram (U-phase).

When the HSR rotates, current is induced in the coils. These coils then create their own rotating magnetic field. The number of magnetic pole-pairs in this field is exactly the same as it was when a 3-phase power supply was applied. Therefore the operating condition as a magnetic gear is satisfied.

2.3 Operating Characteristics

In this chapter, the operating characteristics such as the transmission torque and efficiency will be discussed.

To determine the transmission torque characteristics, dynamic analysis using FEM was conducted. The HSR is the input rotor and rotated at 60 rpm, and a load is applied and increased steadily from 0 Nm to 15 Nm to the LSR, which is the output rotor. The analysis conditions are summarized in Table A2.1.

Table A2.1 Analysis conditions.

Input rotor (HSR) speed	60 rpm
Output rotor (LSR) load	0, 1, 2, 3, 4, 5, 8, 10, 12, 15 Nm

Fig. A2.2 shows the rotation angle of the output rotor. The operation is not smooth due to heavy fluctuations in the transmission torque. Also, it can be seen that when a load of 10 Nm onwards was applied to the output rotor, it stopped rotating. Fig. A2.3 summarizes Fig. A2.1 as a curve showing the N-T characteristics of the magnetic gear. We can see that the analysis results roughly fit a parabolic curve, which is quite common in some conventional induction motors.

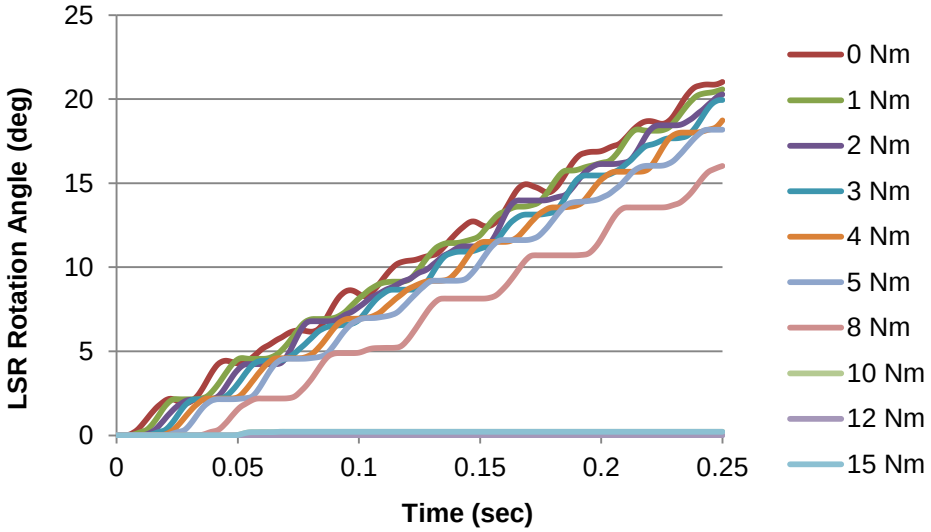

Fig. A2.2 Output rotation speed at different loads.

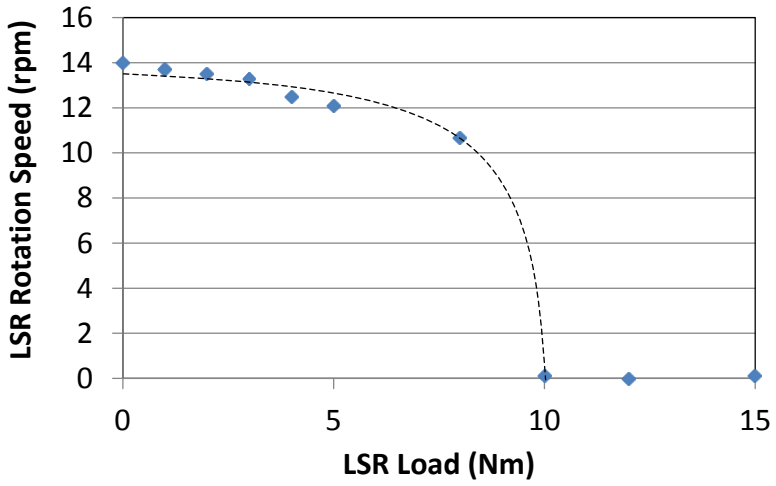

Fig. A2.3 N-T curve.

Some of the transmission torque graphs are shown in Fig. A1.18. The torque fluctuations are very evident here. Also, when the load was 10 Nm, the LSR could not rotate any more, as is evident by how the torque waveform shown in Fig. A1.18(c) is qualitatively different from (a) and (b): the waveforms in the graph are not straight lines, and instead resemble sine waves.

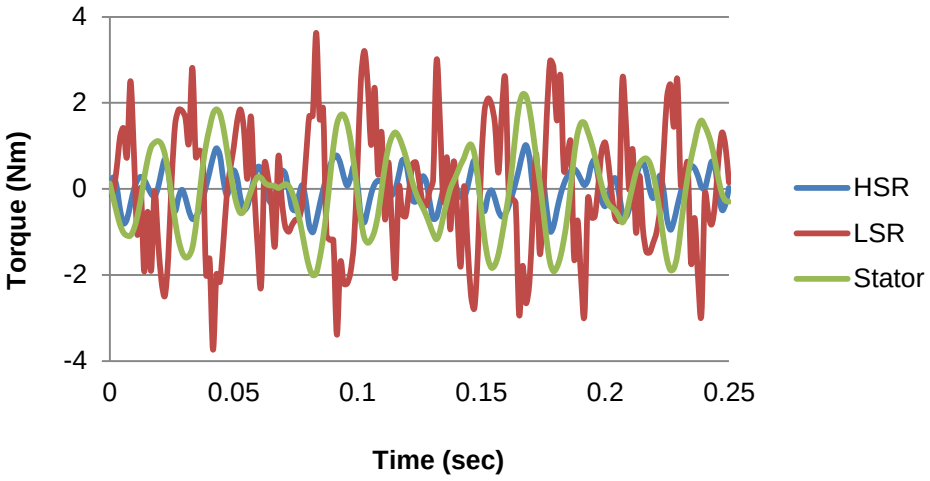

(a) Load 0 Nm

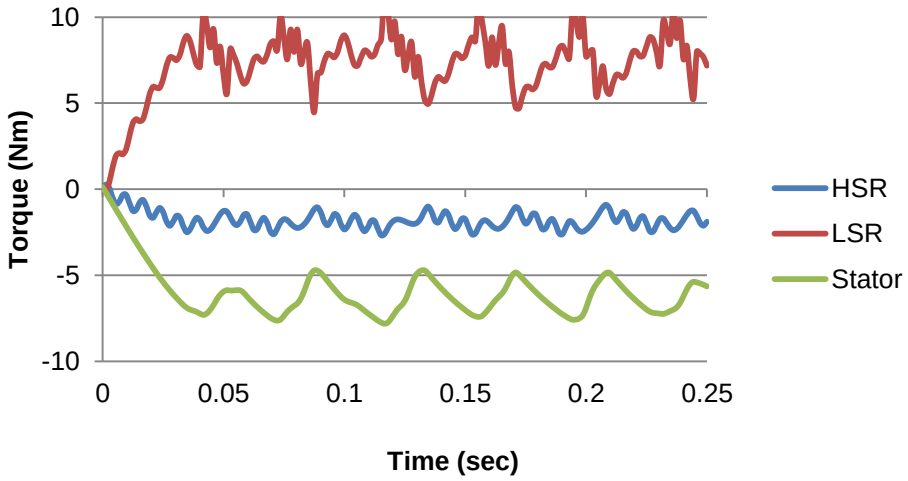

(b) Load 8 Nm

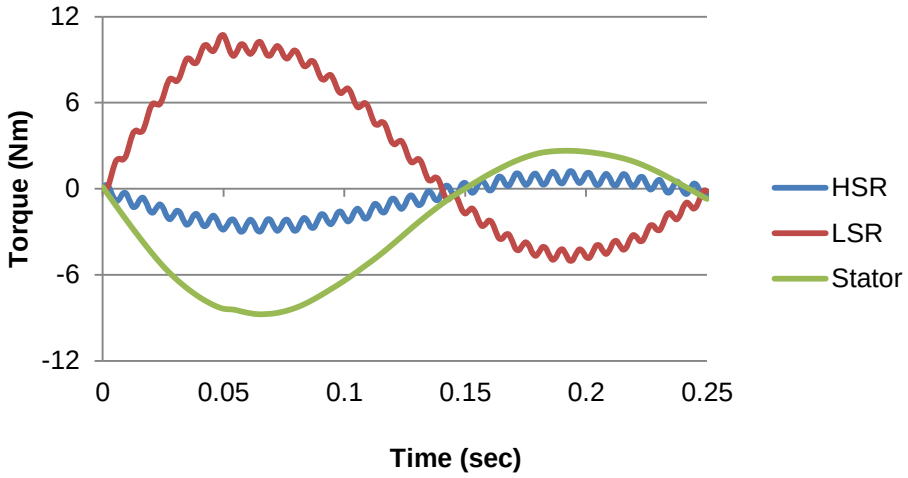

(c) Load 10 Nm

Fig. A2.4 Transmission torque at different loads

Fig. A2.5 summarizes the transmission torque graphs, and shows how the mean torques changes linearly according to the load torque. The results for 10, 12, and 15 Nm are omitted from this graph. From Fig. A2.5, we can see that at 60 rpm rotation speed input, the output rotor can carry a load of 8 Nm. For this model, this calculates to a transmission torque density of 4.4 kNm/m^3.

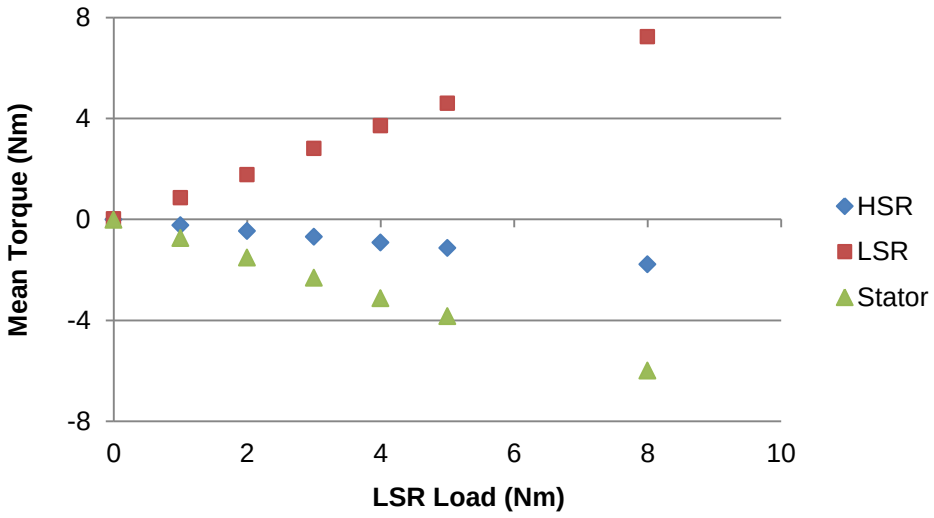

Fig. A2.5 Mean transmission torque.

The torque ratio, which is the ratio between the LSR and HSR, is shown in Fig. A2.6. The torque ratio is always 4.25, which is the value it would be if a 3-phase AC supply was actively applied to the coils.

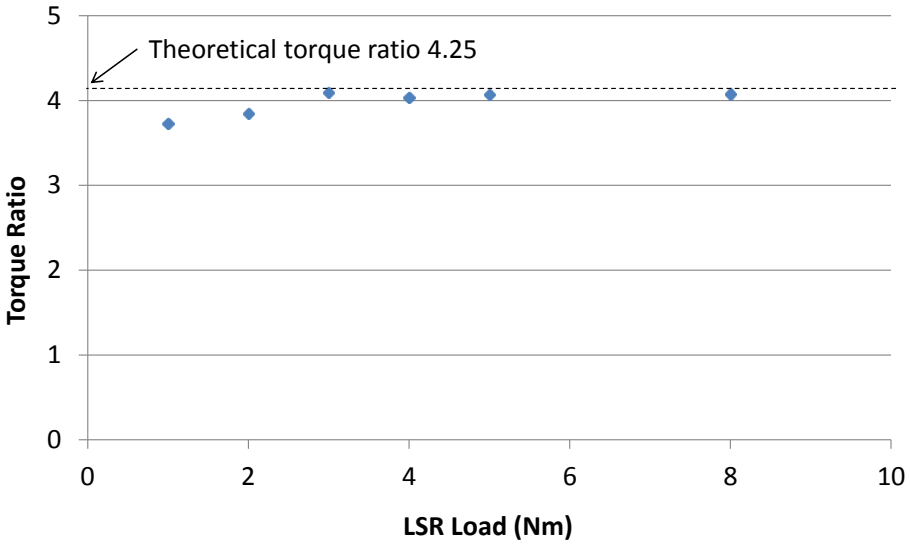

Fig. A2.6 Torque ratio (LSR / HSR).

Next, the efficiency is discussed. Iron and mechanical losses are ignored. Only copper loss is considered. The efficiency is calculated by the following formula.

$$\eta = \frac{\tau_{out}\omega_{out}}{\tau_{in}\omega_{in}} \times 100\% \qquad \text{(A2.1)}$$

The efficiency curve with respect to load is shown in Fig. A2.7. It is quite high, at about 90% at low loads. The analysis results also more or less fit a parabolic curve, which is again similar to some types of conventional induction motors.

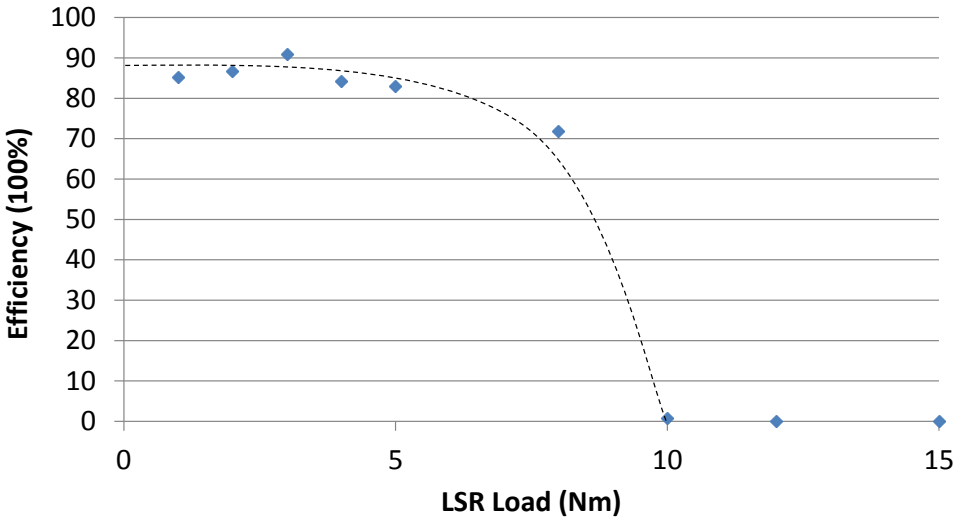

Fig. A2.7 Efficiency.

2.4 Summary

In this chapter, the possibility of the CVGR-MG using induced currents was explored. The rotating PMs on the HSR excited the coils in the stator, inducing currents in them. It was discovered that the CVGR-MG could function like a normal magnetic gear and the efficiency is high. The down side is that since no electric power is being actively applied to the coils, the gear ratio can no longer be controlled. If the load and input rotor speed is fixed, then the gear ratio will also be fixed.

However, for this type magnetic gear, the faster the HSR rotates, the larger the currents will be induced in the coils, which of results in larger transmission torques. In the analyses shown, when the HSR was only rotated at 60 rpm, it had a

transmission torque density of 4.4 kNm/m^3. Therefore, for applications where the HSR is rotated at high speeds, this induction magnetic gear would be a good choice since it can have a high transmission torque density, but at the same time, only require half the number of permanent magnets of the magnetic gear proposed in scientific literature by Atallah.

Acknowledgements

The author would like to thank Professors Katsuhiro Hirata and Eiji Arai, Associate Professor Fumikazu Miyasaka, and also Assistant Professor Noboru Niguchi for their advice and feedback throughout this research. The author would also like to thank his lab colleagues who have made his time in Hirata Laboratory a wonderful experience. Finally, the author would also like to thank his family for their constant support.

Research Achievements

Published Papers

(1) Ariff ZAINI, Noboru NIGUCHI and Katsuhiro HIRATA, "Continuously Variable Speed Magnetic Gear", 日本 AEM 学会誌 Vol.20, No.2, pp.337-341, 2012.06

(2) Ariff Zaini, Noboru Niguchi, and Katsuhiro Hirata,"Continuously Variable Speed Vernier Magnetic Gear", IEEE Transactions on Magnetics, VOL. 48, No. 11, pp.3104-3107, 2012.11

(3) Noboru Niguchi, Katsuhiro Hirata, Ariff Zaini, "Electromagnetic Vibration Analysis and Measurement of a Magnetic Gear", IEEJ Journal of Industry Applications Vol.2, No.6, pp.261-268, 2013.11

International Conferences

(1) Ariff Zaini, Noboru Niguchi and Katsuhiro Hirata, “Continuously Variable Speed Magnetic Gear”, Proceedings of the 20th MAGDA Conference in Pacific Asia,Kaohsiung, Taiwan, 1A35, pp74-78, 2011.11

(2) Ariff Zaini, Noboru Niguchi and Katsuhiro Hirata, “Continuously Variable Speed Vernier Magnetic Gear”, Proceedings of INTERMAG 2012 (International Magnetics Conference), Canada, BG-04, 2012.05.

(3) Noboru Niguchi, Katsuhiro Hirata, Ariff Zaini, Shingo Nagai, "Proposal of an Axial-Type Magnetic-Geared Motor", Proceedings of the International Conference on Electorical Machines (ICEM2012), France, pp.736-741. 2012.09

(4) Ariff Zaini, Noboru Niguchi, Katsuhiro Hirata, "Dynamic Analysis of a Vernier Magnetic Gear with a Continuously Variable Gear Ratio", Proceedings of 15th Biennial IEEE CEFC (Conference on Electromagnetic Field Computation), Oita, Japan, TP5-24, p.295, 2012.11

(5) Noboru Niguchi, Katsuhiro Hirata, Ariff Zaini, Eiki Morimoto, and Yuki Ohno, “N-T Characteristics Analysis of a Magnetic-Geared Induction Motor”, Proceedings of CEFC2014(16th Biennial IEEE Conference on Electromagnetic Field Computation), Annecy, France, OF2:3, 2014.05

Domestic Conferences

(1) アリフザイニ，新口昇，平田勝弘，"減速比を連続的に変化可能なバーニア型磁気歯車の提案"，静止器・回転機合同研究会，SA-12-46，pp.133-138，2012.01

(2) アリフザイニ，新口昇，平田勝弘，"バーニア型磁気歯車の補助ティースの

トルクへの影響", 回転機・リニアドライブ・家電・民生合同研究会, LD-12-56, pp.23-28, 2012.08

(3) アリフザイニ, 新口昇, 平田勝弘, "誘導電流を用いた磁気ギアードモータの提案", 電気学会静止器・回転機合同研究会, SA-13-25, pp.53-56, 2013.01